UNIVERSITÀ DEGLI STUDI DI MILANO

Scuola di Dottorato in Fisica, Astrofisica e Fisica Applicata

Dipartimento di Fisica

Corso di Dottorato in Fisica, Astrofisica e Fisica Applicata

Ciclo XXVII

Challenges for Present and Future Cosmic Microwave Background Observations: Systematic Effects and Foreground Emission in Polarization

Supervisore: Professor Aniello MENNELLA

Coordinatore: Professor Marco BERSANELLI

Tesi di Dottorato di:

Nicoletta KRACHMALNICOFF

Anno Accademico 2014/2015

Commission of the final examination:

External Referee:
Dott. Jean-Christophe Hamilton

External Member:
Prof. Carlo Baccigalupi

External Member:
Prof. Massimo Gervasi

Internal Member:
Prof. Aniello Mennella

Final examination:

June 29th, 2015

Università degli Studi di Milano, Dipartimento di Fisica, Milano, Italy

MIUR subjects:

FIS/05 - Astronomy and Astrophysics

PACS:

98.80.Es - Observational cosmology

Contents

Part II Systematic effects control for LSPE/STRIP experiment

Introduction

We are lucky enough to live in an epoch where we can observe and measure the Cosmic Microwave Background (CMB) radiation and study its characteristics to get information about the origin and evolution of our universe, sometimes with an impressive accuracy.

We are also lucky enough to live in an epoch where technology moves quickly, giving the possibility to observational cosmologists to go deeper and deeper with their measurements but also forcing them to face new experimental challenges.

In this framework I developed the work carried out during my PhD in which I mainly analyzed data and performed computational simulations for experiments aimed at observing the CMB polarization, focusing my efforts on two specific topics: the study of foreground emissions, including the astrophysical component separation, and the characterization of instrumental systematic effects.

The characterization of the polarized CMB signal is, nowadays, one of the most important branches of observational cosmology. Indeed, in the curl component of the CMB polarization field (also known as "B-modes") it is thought to be hiding the imprint of primordial gravitational waves. The presence of gravitational waves, perturbing the metric of the primordial universe and leaving a signature in the CMB polarized signal, is one of the prediction of the inflationary paradigm. This theory accounts for the accelerated expansion of the universe that is thought to have happened in the very first stages of its evolution. Detecting the B-modes CMB signal would, therefore, give a strong and well-founded evidence for the inflation theory, opening the doors for the study of the physics of the very early universe, which today is far from being completely understood.

Nevertheless, given the extreme faintness of such a signal, which is at the level of fraction of μK, its detection is anything but easy. To achieve the measurement of such tiny differences in the sky temperature, it is, indeed, necessary to build complex experiments with extremely high sensitivity. Moreover, the sky signal in the CMB microwave frequency range is dominated by other brighter astrophysical emissions, mainly coming from our Galaxy. Removing the contamination from these other kind of emissions is mandatory to recover the cosmological imprints encoded in the CMB signal.

An emblematic example of how the foreground contamination is a key issue in CMB experiments is certainly represented by the observations performed by the BICEP2 tele-

scope and the subsequent efforts aimed at characterizing and understanding the physical origin of the detected signal.

With its high sensitivity, BICEP2 has been the first experiment able to measure a polarization B-modes signal compatible with what expected from primordial gravitational waves. The observations were performed on a small sky patch (about 1% of the sky), at one-degree angular scale, in a single frequency band centered at 150 GHz (BICEP2 collaboration I 2014).

The BICEP2 collaboration announced this thrilling detection in March 2014, leading to a lively discussion within the scientific community concerning the actual cosmological nature of the observed signal.

Catalyzed by such remarkable measurements, the Planck collaboration started a deep analysis of the multi-frequency Planck data, with the precise goal of characterizing the Galactic foreground emission and understanding its impact on BICEP2 results. I was actively involved in this analysis, since the beginning, and in this thesis I describe my contribution to it. My work, in particular, was focused on the study of the polarized thermal dust emission in the BICEP2 region of the sky, using mainly Planck data at the highest available frequency of 353 GHz, where the Galactic dust radiation dominates the sky emission. The criticalities faced during the analysis are also described in the thesis, concerning in particular the difficulty of retrieving information from Planck data on such a small region of the sky, where the sensitivity of the instrument is not optimal.

The final results of this analysis show that the level of contamination from thermal dust emission in the BICEP2 field is high enough to account for the entire B-modes signal observed by BICEP2, as we reported in Planck Collaboration Int. XXX (2014). This result has been confirmed by the subsequent joint analysis of the BICEP2 and Planck data, which is also summarized in this thesis. The cross-correlation between the data coming from the two instruments allowed, nevertheless, to put a stringent upper limit on the expected level of CMB B-modes signal (BICEP2/Keck Array and Planck Collaborations 2015).

Galactic foreground emission is not the only source of contamination for CMB experiments. Spurious signals can also arise from instrumental systematic effects. This is especially critical for observations in polarization, given the faintness of the CMB signal and the consequent high sensitivity requested by the experiments, which often have a complex architecture.

We do know, for example, that the characterization of systematic effects still represents a challenge in the Planck data analysis, delaying the final release of Planck scientific products (Planck Collaboration I 2015).

In the work done for this thesis I also dealt with this issue, studying the case of a future balloon-borne experiment for CMB polarization observations, the *Large Scale Polarization Explorer* (LSPE).

This experiment is currently in the development phase, with the first flight planned for December 2016 (LSPE Collaboration 2012). LSPE observations will last for about 15 days, with the balloon flying around the North Pole, during the polar night. They will cover a large fraction of the sky of about 30%, in four different frequency channels (43, 140, 220, 240 GHz) and will be carried out with two different instruments. The main goal of the experiment is to observe the CMB polarization with high sensitivity, on the very

large angular scales, and to put further constraints on the level of the B-modes signal. The multi-frequency observations will also allow to characterize foreground emissions.

The second part of this thesis is focused on the implementation of a simulation pipeline for the *STRatospheric Italian Polarimeter* (STRIP) instrument onboard LSPE. STRIP is composed by an array of polarimeters (49 detectors) based on radiometric technology and will observe the sky at a frequency of 43 GHz, where the Galactic synchrotron radiation dominates the sky emission (LSPE-STRIP Collaboration 2012).

The pipeline simulates the flight mission, considering the sky scanning strategy and the instrument architecture, with the goal of computing end-to-end simulations of the sky observation to assess the scientific performance of the experiment. Moreover, it includes also the presence of possible non-idealities in the polarimeter behavior which can lead to several systematic effects. Thanks to this simulations, I have estimated the final impact of these effects on the sky observations.

I would like to mention that, as it often happens in modern experimental physics, the work presented in this thesis has been carried out in the context of large scientific collaborations and therefore includes also the efforts of several colleagues who I gratefully acknowledge here.

Organizational note

This thesis is organized as follows.

Chapter 1: in this chapter I review the modern theories describing the evolution of our universe focusing the discussion on observational evidences and, in particular, on the proprieties of CMB. I start with a brief description of the Standard Big Bang theory mentioning the experimental evidences strongly supporting it and simultaneously the problems of this model. I then review the Inflation paradigm which is able to address these issues. I also describe the CMB features, illustrating in particular the CMB temperature anisotropies characteristics and the properties of their power spectrum. Moreover, I review the physics underlying the CMB polarization signal together with the modern status of observations.

Chapter 2: this chapter is focused on the two key topics of this thesis: the Galactic foreground emissions and the instrumental systematic effects which may affect CMB experiments. In particular, I describe the characteristics of polarized thermal dust and synchrotron emissions, relying on the multi-frequency observations performed by WMAP and Planck satellites. I then illustrate the general impact that foreground emissions can have on the observation of the CMB polarization signal and the available computational algorithms able to compute the separation of the various astrophysical components. In the second part of the chapter I report a general review on the possible instrumental systematic effects, focusing, in particular, on polarization measurements, taking the Planck instrumentation as a reference case.

Chapter 3: here I describe the first part of the work done for this thesis, concerning the characterization of thermal dust polarized radiation at high Galactic latitude and,

in particular, its contamination to the BICEP2 CMB observations. As introduction, I present the BICEP2 measurements together with their original physical interpretation in terms of primordial gravitational waves. Next, I summarize the main results obtained from Planck high frequency data on the properties of thermal dust radiation and its polarization power spectra. I then move to the description of the methods used to assess the level of contamination by dust emission in BICEP2 measurements and I present the important obtained results. Finally, I review the main aspects of joint analysis performed by the Planck and BICEP2/Keck collaborations.

Chapter 4: in this chapter I describe the computational simulation pipeline developed for the STRIP instrument onboard the LSPE experiment. In the first sections I review the experiment characteristics describing both the instruments that will observe the microwave sky in the four frequency channels and summarizing the expected scientific performance. I present, with more details, the characteristics of the STRIP instrument, with an analytical description of the polarimeters architecture. I then move to the functioning of the developed pipeline, with the analysis of the results obtained from these simulations in both ideal and non-ideal case. In this latter case I summarize the impact of systematic effects on final scientific results.

Conclusions: here, finally, I review the main results of the work done for this thesis and provide an outlook on possible future developments. I also focus on a general description about the future of CMB polarized observations.

Appendix A: since, during the work done for this thesis, I have intensively analyzed data coming from the Planck satellite, in this appendix I report a very brief description of the Planck space mission and its onboard instrumentation.

Evolution of the universe and the Cosmic Microwave Background

In this introductory chapter we briefly review the modern theory which describes the evolution of the universe focusing our discussion on observational evidences and, in particular, on the proprieties of the Cosmic Microwave Background (CMB) which represents the key topic of this thesis.

The chapter is organized as follows: in sections (1.1) a brief description of the thermal history of the universe is reported; section (1.2) and (1.3) introduce the Standard Big Bang theory and the Inflation paradigm respectively; the CMB radiation features are described in the last two sections. In particular, the CMB temperature anisotropies characteristics are illustrated in section (1.4) together with a description of the CMB temperature power spectrum and the cosmological parameters whose values can be obtained from the its analysis; section (1.5) is focused on the polarization of the CMB, giving particular attention to the encoded information on the early universe and to the current status of observations.

1.1 A brief thermal history of the universe

In the past decades astrophysical observations gave us undeniable evidence for the expansion of the universe: the light from distant galaxies is systematically shifted toward the red end of the spectrum (Hubble 1929), the observed abundances of the light elements (H, He and Li) matches the prediction of the Big Bang Nucleosynthesis (BBN, Alpher et al. 1948), and the only convincing explanation for the existence of the Cosmic Microwave Background (CMB) is a relic radiation from the hot primordial universe (Dicke et al. 1965).

From 10^{-10} seconds after the Big Bang to today the history of the universe is based on well understood and experimentally tested laws of particle, nuclear and atomic physics and gravity. We can infer that at energy scale below ~ 100 GeV (10^{-10} to 10^{-6} seconds after the Big Bang) the symmetry between the electromagnetic and the weak force was broken and the cross section of weak interaction decreased as the temperature of the universe dropped. As a result, at ~ 1 MeV (~ 1 s), neutrinos decoupled from the rest of matter. Around 0.1 MeV (~ 3 min) the strong interaction became important and protons and neutrons combined to form light elements. The successful prediction of the H, He and Li abundances in our universe is one of the most convincing evidence supporting the Big Bang theory. The matter and radiation densities were equal at around 1 eV (10^{11}

s). In this primordial state, charged matter particles and photons were strongly coupled in the plasma and fluctuations in the density propagated as cosmic "sound waves". Around 0.1 eV ($\sim$ 380.000 yrs) protons and electrons combined to form neutral hydrogen atoms. Photons thus decoupled from matter and the CMB was free to propagate in the universe. Today, about 13.8 billion years later, these photons give us the earliest snapshot of the universe and anisotropies in the CMB temperature an polarization provide us the evidence for fluctuations in the primordial plasma.

As the universe evolved, the small primordial density perturbations grew via gravitational instability to form the Large-Scale Structure (LSS) observed in the late universe. During radiation domination the growth of the structures was slow. Clustering became more efficient after matter started to dominate the background density. On small scales gravitationally bound objects started to form and decoupled from the overall expansion. This led to a picture of hierarchical structure formation with small-scale structures (like stars and galaxies) forming first and then merging into larger structures (clusters and superclusters of galaxies).

Around redshift $z \sim 20$, high energy photons from the first stars began to ionize the hydrogen in the Inter-Galactic Medium (IGM). This process of "reionization" was completed at $z \sim 6$. Meanwhile, the most massive stars run out of nuclear fuel and exploded as supernovae creating the heavy elements (C, O, ...). At $z \sim 1$, a "dark energy" with negative pressure started to dominate the universe leading to the accelerating expansion that we observe today.

1.2   The Standard Big Bang model

Although it is an evidence that matter in the universe we observe today is clustered in gravitationally bound structures, observations at scales larger than these structures show that the distribution of matter is homogeneous and isotropic at high level. The observation of homogeneity and isotropy on large scales necessarily concerns the universe observed from our position. Nevertheless, we can assume this is the case for any other position in the universe as well. Such an assumption leads to the *Cosmological Principle* according to which

> *viewed on sufficiently large distance scales, there are no preferred directions or preferred places in the universe.*

Relying on General Relativity (GR) for the dynamical evolution of the space-time, the Cosmological Principle represents the starting point for characterizing the metric of the universe.

To describe the evolution of the expanding universe it is convenient to introduce a scale factor $a(t)$, whose present value is set to one. The distance of a given point can be written as $r(t) = xa(t)$, where x is the so called *comoving distance* and is equal to the physical distance at the present epoch. To understand the evolution of the universe we must investigate how the scale factor varies with time. This evolution is determined by the energy density of the universe. GR is the theory that provides the connection between the evolution of the scale factor and the energy in the universe.

At any epoch the expansion rate of the universe is given by the *Hubble parameter*:

$$H \equiv \dot{a}/a, \tag{1.1}$$

where dots denote derivative with respect to cosmic time t. It is also useful to introduce the so called *conformal time*:

$$d\eta = \frac{dt}{a(t)} \tag{1.2}$$

and the integral of this quantity:

$$\eta = \int_0^t \frac{dt'}{a(t')} \tag{1.3}$$

which represents the comoving distance that light could have traveled in a time t^{1}. This length, called *comoving horizon*, implies that regions separated by distance larger then the comoving horizon are not causally connected.

Homogeneity and isotropy lead to a specific form for the metric of the universe which assumes the simple form of Friedman-Robertson-Walker (FRW) metric:

$$ds^2 = dt^2 - a^2(t) \left[\frac{dr^2}{1 - Kr^2} + r^2(d\theta^2 + \sin^2\theta d\phi^2) \right] \tag{1.4}$$

where spherical polar coordinates have been adopted. The quantity K parametrizes the spatial curvature of the universe defining its geometry, in particular:

- $K < 0$: hyperbolic geometry;

- $K = 0$: euclidean geometry (flat universe);

- $K > 0$: spherical geometry.

The evolution of the scale factor $a(t)$ is governed by Einstein field equations:

$$G_{\mu\nu} \equiv R_{\mu\nu} - \frac{1}{2}Rg_{\mu\nu} = 8\pi G T_{\mu\nu}; \tag{1.5}$$

the left-hand side of these equations (the Einstein tensor $G_{\mu\nu}$) describes the geometry of the space-time through the metric tensor ($g_{\mu\nu}$), its first and second derivatives contained the Ricci tensor ($R_{\mu\nu}$) and the Ricci scalar (R). On the right-hand side, instead, the energy-momentum tensor ($T_{\mu\nu}$) is responsible for the energy and momentum carried by matter. G is the Newton constant. Under the assumption of homogeneous and isotropic universe we can assume $T_{\mu\nu}$ as that of a perfect fluid:

$$T_{\mu\nu} = (\rho + P)u_\mu u_\nu + P g_{\mu\nu}, \tag{1.6}$$

where ρ is the density, P the pressure, u_μ the 4-velocity vector. Using this expression for the energy-momentum tensor and the FRW metric, Einstein equations reduce to just two equations for the scale factor time evolution:

$$H^2 = \frac{8\pi G}{3}\rho - \frac{K}{a^2}, \tag{1.7}$$

$$\frac{\ddot{a}}{a} = -\frac{4\pi G}{3}(\rho + 3P). \tag{1.8}$$

---

[1]Hereafter we consider natural units with $c \equiv 1$

We can now consider the densities for the different components of our universe: matter (baryonic matter and Cold Dark Matter, CDM[2]) ρ_m, radiation (photons and neutrinos) ρ_r, and the cosmological constant ρ_Λ. The latter is included to take into account the accelerated expansion of the universe we measure today thanks to observations of distant supernovae (Riess et al. 1998; Perlmutter et al. 1999). Moreover we can also define a critical density:

$$\rho_c = \frac{3H^2}{8\pi G},$$
(1.9)

and write equation (1.7) as:

$$H^2 = H_0^2 \left(\frac{\rho_m}{\rho_{c,0}} + \frac{\rho_r}{\rho_{c,0}} + \frac{\rho_\Lambda}{\rho_{c,0}} \right) - \frac{K}{a^2},$$
(1.10)

where H_0 and $\rho_{c,0}$ represent the value of the parameters evaluated today. By introducing the following adimensional quantities:

$$\Omega_m = \Omega_b + \Omega_c = \frac{\rho_m}{\rho_c}, \qquad \Omega_r = \Omega_\lambda + \Omega_\nu = \frac{\rho_r}{\rho_c}, \qquad \Omega_\Lambda = \frac{\rho_\Lambda}{\rho_c},$$
(1.11)

and considering the relation between densities and the scale factor given by

$$\rho_m \propto \frac{1}{a^3}, \qquad \rho_r \propto \frac{1}{a^4}, \qquad \rho_\Lambda \propto \text{constant},$$
(1.12)

we can finally write equation (1.10) as:

$$H^2 = H_0^2 \left(\frac{\Omega_{m,0}}{a^3} + \frac{\Omega_{r,0}}{a^4} + \Omega_{\Lambda,0} \right) - \frac{K}{a^2}.$$
(1.13)

The value of the density parameters, which are now explicitly included in the Friedamm equation and represent the fundamental parameter of the so called ΛCDM model (Λ Cold Dark Matter), can be extract from observations of the CMB, as will be described in section (1.4).

This model describes very well some of the cosmological observations made in the past decades. Nevertheless several fundamental questions are still unsolved:

- *Flatness problem:* current observations show a very nearly spatially flat universe. If we examine the evolution of the space-time curvature, in the framework of the Standard Big Bang model, we discover that during the radiation dominated epoch the curvature grows quickly with time, i.e. the spatially flat solution is unstable. To explain today spatially flat geometry we need to introduce fine-tuned initial conditions.

- *Horizon problem:* we know that the universe is homogeneous and isotropic on very large scales. In particular if we look at the CMB sky we find that the temperature of the radiation is the same in every direction, even for regions at distance larger than the horizon scale at the time when the CMB was released. In fact, region that, in the Standard Big Bang model, would be causally connected ~ 380.000 years after

---

[2]"Cold" means non-relativistic at the time of decoupling. The Standard Big Bang model has CDM as the dominant non-relativistic component of the universe.

the Big Bang, subtend now an angle of about $1°$ in the sky. In the Standard Big Bang model there is not any mechanism which can explain a causally connection between regions larger than this angular dimension.

- *Relic problem:* the breaking of symmetries at the extremely high energy associated with the early universe leads to the production of many unobserved particles such as the magnetic monopole (Guth & Tye 1980).

Each of this problems can be solved by assuming that the early universe experienced a brief but very intense period of accelerated expansion, inflating by a factor of at least 10^{26} within less than 10^{-34} seconds. This implies that the physical wavelengths in the early universe grow faster then the physical horizon, reminding that physical wavelengths expansion is determined by the scale factor evolution while the physical horizon evolves always at the speed of light.

In this scenario, physical distances that are now inside the horizon but were outside at the time when the CMB was released, could have been causally connected in the very early stage of the universe, explaining the observed homogeneity an isotropy of the universe.

The same mechanism solves also the flatness problem: during the inflationary period physical scales grow so rapidly that today we observe only a very small region of the entire universe that has been stretched by this rapid expansion; the universe may appear flat because its curvature has been stretched as the others physical lengths.

Similarly, if magnetic monopole existed in the early universe such an evolution dilutes it, until it is not anymore observable in today universe.

1.3 Inflationary paradigm

We have seen that the inflationary paradigm requires an accelerated expansion. From equation (1.8), requiring $\ddot{a} > 0$ in a flat universe ($K = 0$) implies:

$$P < -\frac{\rho}{3}. \tag{1.14}$$

Since the energy density is always positive, pressure must be negative, meaning that whatever it is that drives inflation is not ordinary matter or radiation. To solve Friedmann equations and determine the evolution of the scale factor we assume the extreme condition $P = -\rho$ which considerably simplify the analysis. With such an assumption, combining the continuity equation for the perfect fluid stress-energy tensor:

$$\dot{\rho} + 3H(\rho + P) = 0, \tag{1.15}$$

with Friedmann equations, one finds the following relations:

$$\rho = \text{constant} \tag{1.16}$$

and

$$H = H_I = \text{constant}. \tag{1.17}$$

Therefore, we have that the scale factor during inflation grows as:

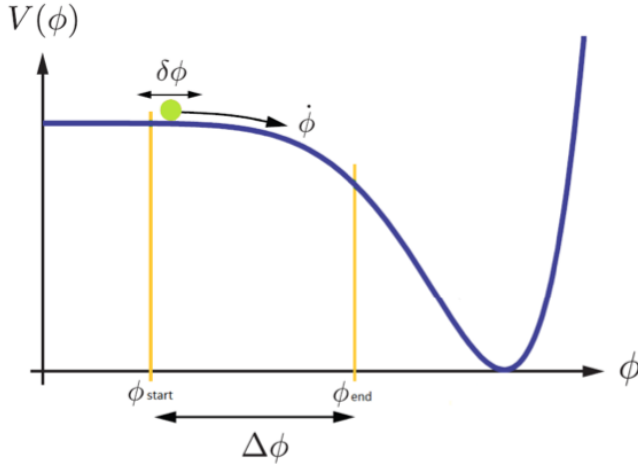$$a(t) = a_I e^{H_I(t-t_i)} \tag{1.18}$$

Figure 1.1: Example of slow-roll potential for the scalar field ϕ.

where t_i is the time inflation starts.

Inflation is a very unfamiliar physical phenomenon: within a fraction of second the universe grows exponentially at an accelerating rate. The simplest models of inflation takes into account a single scalar field ϕ, with a potential $V(\phi)$. The scalar field, called the *inflaton*, is a parameter used to parameterize the time-evolution of the inflationary energy density. Is it possible to obtain the expression for the energy-momentum tensor for this scalar field:

$$T_{\mu\nu} = \partial_\mu \phi \partial_\nu \phi + g_{\mu\nu} \left[-\frac{1}{2} g^{\alpha\beta} \partial_\alpha \phi \partial_\beta \phi - V(\phi) \right]. \tag{1.19}$$

Comparing this with equation (1.6), one finds that the scalar field $\phi(t)$ behaves like a perfect fluid with:

$$\rho_\phi = \frac{\dot{\phi}^2}{2} + V(\phi) \tag{1.20}$$

$$P_\phi = \frac{\dot{\phi}^2}{2} - V(\phi). \tag{1.21}$$

Friedmann equations then take the expression:

$$H^2 = \frac{8\pi G}{3} \left(\frac{\dot{\phi}^2}{2} + V(\phi) \right) \tag{1.22}$$

$$\frac{\ddot{a}}{a} = -\frac{4\pi G}{3} \left(\frac{\dot{\phi}^2}{2} - V(\phi) \right). \tag{1.23}$$

We can therefore conclude that if

$$V(\phi) \gg \dot{\phi}^2 \tag{1.24}$$

we obtain the desired condition:

$$P_\phi \simeq -\rho_\phi. \tag{1.25}$$

From this simple calculation, we realize that a scalar field whose energy density is dominant in the universe and whose potential energy dominates over the kinetic term gives rise to inflation. An example of such a situation is given by a field trapped in a false vacuum, i.e., a local, but not the global, minimum of the potential: since it is trapped, it has little kinetic energy, however the potential is nonzero, so the pressure is negative. But, in this scenario, the field could never reach the true vacuum of the potential and so inflation would never end. A possible way to avoid this problem is to introduce a scalar field slowly rolling toward its true ground state. The energy density of such a field is very close to constant so it quickly comes to dominate. This is the so called *slow-roll* condition for inflation; an example for a slow-roll potential is sketched in figure (1.1) (Linde 1982; Albrecht & Steinhardt 1982).

1.3.1 Inflation and cosmological perturbations

As we have briefly seen in the previous sections, the inflationary paradigm solves the horizon, flatness and relic problem. Moreover, combining the inflation paradigm with quantum mechanics provides an elegant mechanism for generating the initial seeds of the structures in the universe we observed today. Indeed, small spatial perturbations in the inflaton ϕ and the metric $g_{\mu\nu}$ are inevitable due to quantum mechanics. They are the seeds of the energy density fluctuations that eventually evolve in baryonic and dark matter density fluctuation, seeding the formation of stars, galaxies and galaxy clusters and leaving their imprint in the CMB temperature and polarization anisotropies that we observe today.
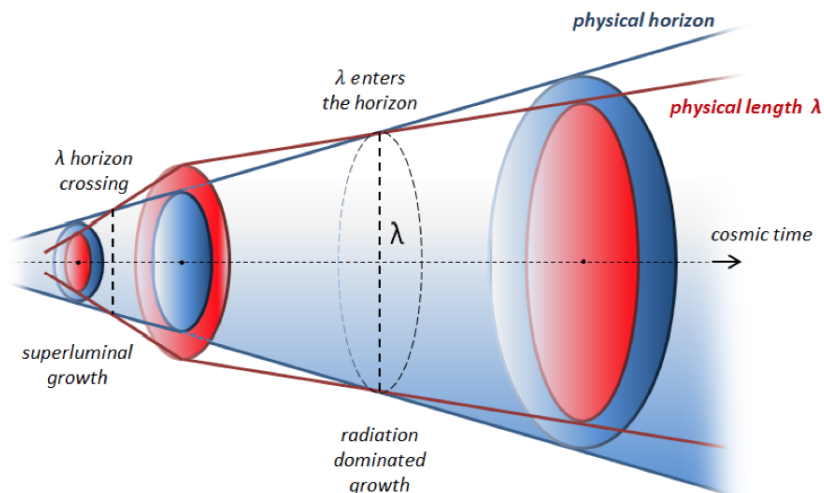

Figure 1.2: Physical horizon and physical length evolution during and after inflation.

During inflation the scalar field fluctuates with a magnitude proportional to the stored energy density ρ which, by Einstein equations, is related to the Hubble parameter H at that time. Fluctuations are created on all length scales with a spectrum of wavenumbers k. Cosmologically relevant fluctuations start inside the horizon then, while the horizon grows at the speed of light, physical scales expand exponentially in time and the perturbations exit the horizon (see sketch in figure 1.2). Since physics does not affect the evolution of fluctuations when their wavelength is outside the horizon, their amplitude is frozen and fixed at the non zero value acquired at the horizon crossing. After inflation ends, those modes return inside the horizon as a stochastic background of perturbations. Clearly, the larger the energy scale at which inflation occurs, the larger will be the residual imprint on primordial plasma of these perturbations after inflation ends.

Many books and review papers revise the mathematical calculation underlying the quantum fluctuation during inflation (see for example Dodelson 2003; Baumann 2009), and going into details is beyond the scope of this thesis. It is important to notice though, that the inflation and metric perturbations can be decomposed into independent scalar, vector and tensor perturbations. The importance of this decomposition is that, if the perturbations are small, they evolve independently and can therefore be treated separately. Moreover, as will be described in the following sections, they also leave different imprints in the CMB signal.

1.4   CMB temperature anisotropies

The CMB radiation is the key topic of this thesis. As mentioned previously, it is the relic radiation from the Big Bang, emitted when the universe was about 380.000 years old, after the decoupling of matter and photons. The CMB was first observed in 1965 by Arno Penzias and Robert Wilson as a temperature excess of about 3 K in every direction of the sky (Penzias & Wilson 1965). Since then, many accurate measurements of the CMB radiation have been carried by three dedicated space missions and many ground based and balloon-borne experiments[3]. We know today that this radiation has a blackbody spectrum at the temperature $T = 2.7260 \pm 0.0013$ K (Fixsen 2009), measured with high accuracy by the FIRAS (*Far Infrared Absolute Spectrophotometer*) instrument onboard the COBE (*COsmic Background Explorer*) satellite (Fixsen et al. 1994). We also know that the CMB radiation is extremely isotropic: temperature anisotropies, which are thought to represent the trace of the primordial fluctuations generated during inflation, are of the order of $\Delta T/T \simeq 10^{-5}$ (Smoot et al. 1992).

In figure (1.3) the most up-to-date full sky map of the CMB temperature anisotropies is shown with an angular resolution of 5 arcmin, obtained thanks to the measurements of the Planck satellite. Planck (European Space Agency, ESA) has been launched in May 2009 and collected data for about four years with the primary goal of observing the CMB radiation on the entire sky with unprecedented sensitivity, angular resolution and frequency coverage, in both total intensity and polarization (Planck Collaboration I 2014). Data from the Planck satellite have been intensively analyzed in the work done for this thesis and a description of this space mission and its onboard instrumentation is reported in Appendix (A).

---

[3]See `http://lambda.gsfc.nasa.gov/product/expt/` for a complete and updated list of experiments dedicated to CMB observations.
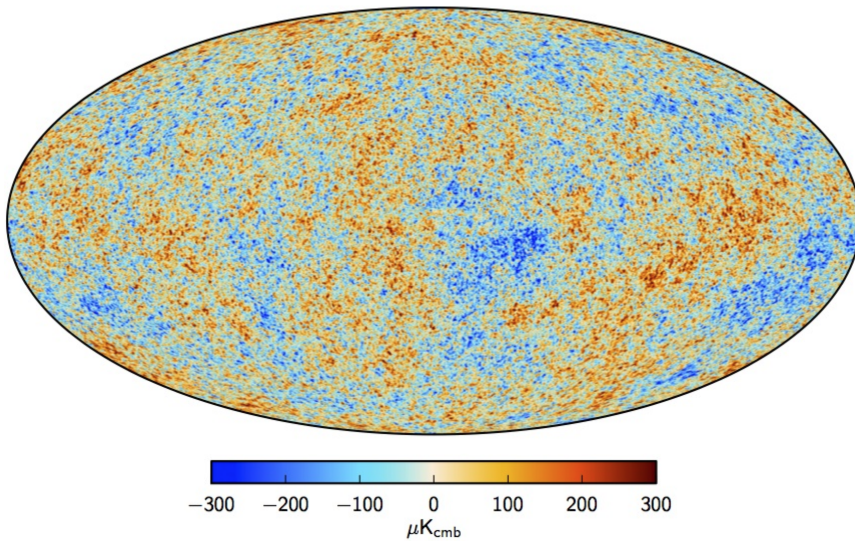
Figure 1.3: Component separated maps of the CMB temperature anisotropies obtained from four years of data of the Planck satellite. The map has an angular resolution of 5 arcmin (Planck Collaboration I 2015).

1.4.1 Power spectrum and cosmological parameters

We detect CMB photons as incoming radiation from any direction of the sky $\hat{n}$. To statistically analyze the CMB anisotropies we need to characterize the radiation field and to study its angular distribution on the sphere. Temperature is a scalar quantity and does not depend on the chosen reference frame; we can therefore expand temperature anisotropies using spherical harmonics as a orthonormal basis:

$$T(\hat{n}) = \sum_{\ell,m} a_{\ell m}^T Y_{\ell m}(\hat{n}). \tag{1.26}$$

The angular power spectrum of the temperature anisotropies is obtained by computing the variance of the zero-mean distribution of the $a_{\ell m}$ coefficients:

$$\langle a_{\ell m} \rangle = 0\,, \qquad \langle a_{\ell m}^* a_{\ell' m'} \rangle = \delta_{\ell \ell'} \delta_{m m'} C_\ell \tag{1.27}$$

where the average is meant to be over an ensemble of realizations. The variance is independent of m, i.e. all the $2\ell + 1$ coefficients for a given ℓ have the same variance:

$$C_\ell = \frac{1}{2\ell + 1} \sum_{m=-\ell}^{m=\ell} \langle a_{\ell m}^* a_{\ell m} \rangle. \tag{1.28}$$

This means that to draw the distribution of each C_ℓ we have no more than $2\ell+1$ samples. Such a limitation is called *cosmic variance* and defines the intrinsic uncertainty in the knowledge of the C_ℓ:

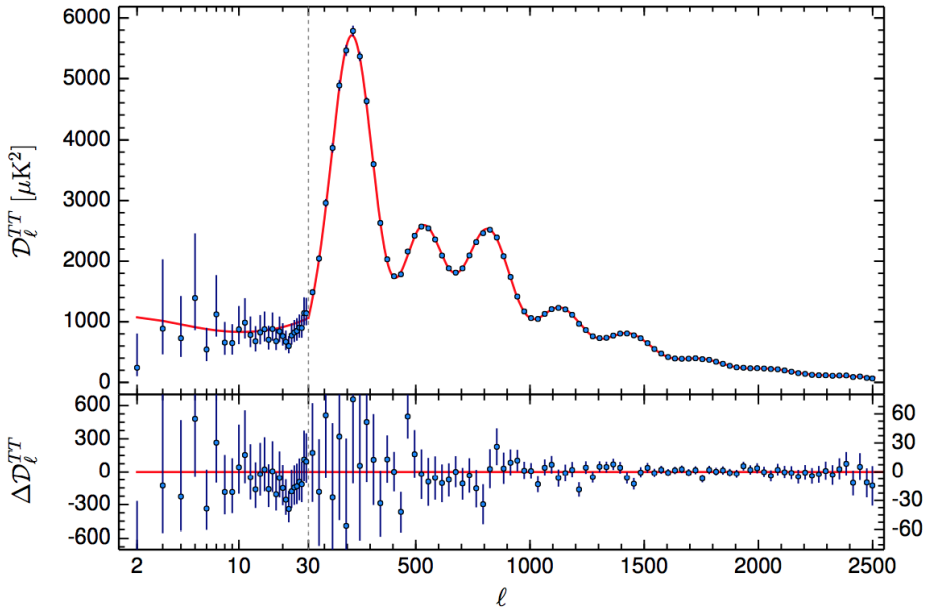$$\Delta C_\ell = C_\ell \sqrt{\frac{2}{2\ell + 1}}, \tag{1.29}$$

Figure 1.4: Angular power spectrum of CMB temperature anisotropies obtained from the Planck map shown in figure (1.3). The spectrum has been computed considering the 94% of the sky. Red solid line represents the best ΛCDM model fit. Lower panel shows the residual with respect to this model (Planck Collaboration XIII 2015).

under the hypothesis of gaussianity of the primordial fluctuations.

Figure (1.4) shows the CMB temperature power spectrum derived from the Planck map in figure (1.3). The $\mathcal{D}_\ell \equiv \ell(\ell+1)C_\ell/2\pi$ are plotted as a function of the multipole moment ℓ, which is proportional to the inverse of the angular scale ($\ell = \pi/\theta$) (Planck Collaboration XIII 2015). The spectrum shows eight acoustic peaks which are the trace of the acoustic oscillations in the primordial plasma. Data are extremely well fitted by a standard ΛCDM model, characterized by a set of cosmological parameters which define the proprieties of our universe. In particular, we can define six main parameters whose values have been derived from the shape of the Planck temperature power spectrum (Planck Collaboration XVI 2014; Planck Collaboration XIII 2015):

- *Hubble constant:* defined as in equation (1.1) it describes the expansion rate of the universe today. From Planck data we can put a $\sim 1\%$ constraint (68% confidence level) on the value of H_0:

$$H_0 = 67.8 \pm 0.9 \quad \mathrm{km\,s^{-1}\,Mpc^{-1}}.$$

- *Acoustic scale:* it is the characteristic angular size of the fluctuations in the CMB. It is determined by the comoving size of the sound horizon at the time of last-scattering, r_s, and the angular diameter distance at which we are observing the fluctuations, D_A. The value of this parameter $\theta_* = r_s/D_A$ is constrained by the

position of the peaks (and not by their amplitude). With accurate measurement of seven acoustic peaks, Planck determined θ_* to better than 0.1% at 1σ:

$$\theta_* = 0.59636° \pm 0.00027°.$$

- *Barionic matter density:* the matter densities in baryons and dark matter can be derived from the relative heights of the acoustic peaks. From Planck data the parameter $\Omega_b h^2$ has been determined with an accuracy of 1% (68% confidence level), with the following value (remember that $H_0 = 100h \, \text{km s}^{-1} \, \text{Mpc}^{-1}$):

$$\Omega_b h^2 = 0.02222 \pm 0.00023.$$

- *Dark matter density:* the value of the dark matter density obtained from Planck data is slightly less accurate, with an uncertainty of about 2% (68% confidence level):

$$\Omega_c h^2 = 0.1197 \pm 0.0022.$$

- *Dark energy density*: the constraint on the dark energy density parameter obtained from Planck data has also an uncertainty of about 2% at 1σ:

$$\Omega_\Lambda = 0.685 \pm 0.013.$$

- *Scalar spectral index:* we have briefly seen in section (1.3.1) that primordial perturbation during inflation are created at all length scales. For the scalar perturbations the power spectrum of the perturbations $\mathcal{P}_s(k)$ is predicted to be proportional to the wavenumber: $\mathcal{P}_s(k) \propto k^{n_s}$. According to this power law a spectral index $n_s = 1$ corresponds to scale invariant fluctuations. Planck data gives constraint on the spectral index parameter with $\lesssim 1\%$ accuracy (68% confidence level):

$$n_s = 0.9655 \pm 0.0062.$$

- *Optical depth:* small-scale fluctuations in the CMB are damped by Thomson scattering from free electrons produced during the epoch of reionization. This scattering suppresses the amplitude of the power spectrum by a factor $e^{-2\tau}$ on scales that correspond to modes with wavelength smaller that the Hubble radius at reionization. The parameter τ is the optical depth of Thomson scattering and can be constraint from Planck temperature (and polarization) power spectrum. The resulting value is:

$$\tau = 0.078 \pm 0.019$$

corresponding to a redshift for reionization (redshift at which the universe is half reionized) of $z_{re} \simeq 10$.

1.5 CMB polarization anisotropies

Thanks to Thomson scattering events during the recombination era the CMB is also partially linearly polarized. In particular the Thomson scattering cross section depends on polarization as:

$$\frac{d\sigma_T}{d\Omega} \propto |\hat{\epsilon}' \cdot \hat{\epsilon}|^2 \tag{1.30}$$

where $\hat{\epsilon}'$ and $\hat{\epsilon}$ are the incident and scattered polarization directions. The outcoming radiation thus is linearly polarized with polarization parallel to the incident one. Nevertheless, if the incoming radiation field is isotropic, the two perpendicular polarization states from orthogonal incident directions would have the same intensity and thus the scattered radiation would remain unpolarized. To generate a net linearly polarized signal we need a quadrupole anisotropy in intensity or temperature in the incident field, as shown in figure (1.5).
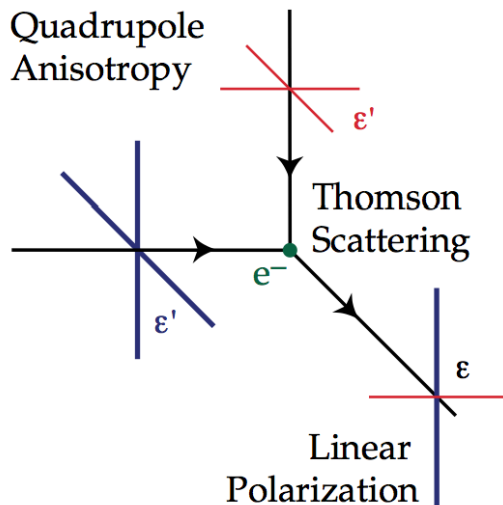

Figure 1.5: Quadrupole anisotropy in the incident radiation generates net linear polarization after Thomson scattering. In this sketch blue (red) lines represent hot (cold) radiation.

As we briefly discuss in the next section, quadrupole anisotropy could have been generated in the primordial plasma by density fluctuations, vorticity in the plasma or gravitational waves which stretch and squeeze the metric. These three different sources of anisotropy correspond scalar, vector and tensor perturbations and leave different kind of imprints in the CMB polarization pattern in the sky.

Polarization state of electromagnetic radiation is usually described by the set of Stokes parameters (I, Q, U, V). In particular the parameter I represents the total intensity of radiation, while Q and U describe the linear polarization. The parameter V is related to the circular polarization of the radiation and, since the CMB is not expected to be circularly polarized, we do not take it into account in our analysis. I is a scalar quantity and does not depend in the reference frame; on the contrary Q and U depend on the chosen coordinate system. A combination of them, though, is invariant under rotation of the polarization plane and define the total polarization intensity of the electromagnetic field, $P = \left(Q^2 + U^2\right)^{1/2}$. In each point in the sky the value of the parameter P together with the polarization angle $\alpha = \arctan(U/Q)/2$ specifies the CMB polarization pattern.

To describe the CMB polarization anisotropies using spherical harmonics, as done for the temperature case, we can introduce the quantities $Q \pm iU$, which are spin-2 objects,

and expand them in terms of tensor spherical harmonics (Zaldarriaga & Seljak 1997):

$$\left(Q \pm iU\right)(\hat{n}) = \sum_{\ell,m} a_{\ell m}^{\pm 2} Y_{\ell m}^{\pm 2}(\hat{n}). \tag{1.31}$$

Instead of $a_{\ell m}^{\pm 2}$ it is convenient to introduce their linear combinations:

$$a_{\ell m}^{E} = -\left(-a_{\ell m}^{2} + a_{\ell m}^{-2}\right)/2\,, \qquad a_{\ell m}^{B} = i\left(-a_{\ell m}^{2} - a_{\ell m}^{-2}\right)/2. \tag{1.32}$$

Starting from these coefficients we can now define the two quantities:

$$E(\hat{n}) = \sum_{\ell,m} a_{\ell m}^{E} Y_{\ell m}(\hat{n})\,, \qquad B(\hat{n}) = \sum_{\ell,m} a_{\ell m}^{B} Y_{\ell m}(\hat{n}) \tag{1.33}$$

which represent the so called *E-modes* and *B-modes* of the CMB and completely specify all the statistical proprieties of the linear polarization field. E and B-modes present a characteristic and different pattern of polarization in the sky: E-polarization vectors are radial around cold spots and tangential around hot spots in the sky, while B-polarization vector has vorticity around any given point in the sky, as shown in figure (1.6).
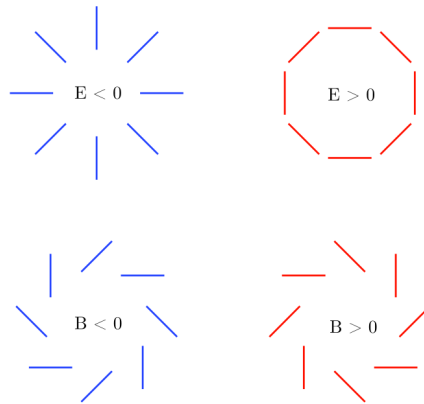
Figure 1.6: E-modes and B-modes polarization pattern in the sky.

From (1.32) we can also construct the C_{ℓ} coefficients to compute the polarization power spectra, in particular we can calculate the auto-correlation of E-modes and B-modes, as well as the cross-correlation between temperature and polarization fluctuations:

$$C_{\ell}^{XY} = \frac{1}{2\ell + 1} \sum_{m=-\ell}^{m=\ell} \langle a_{\ell m}^{*X} a_{\ell m}^{Y} \rangle\,, \qquad X, Y = T, E, B. \tag{1.34}$$

1.5.1 Scalar and tensor power spectra

We have seen that perturbations in the primordial plasma can generate quadrupole anisotropies in the radiation, leading to linear polarization in the CMB we observe today. In particular quadrupole anisotropies can be decomposed into scalar perturbations ($\ell = 2$, $m = 0$), vector perturbations ($\ell = 2$, $m = \pm 1$) and tensor perturbations ($\ell = 2$,

$m = \pm 2$). Starting from geometrical considerations it can be demonstrated that the three different kinds of perturbations are generated by distinct physical processes (for a detailed analysis see for example Hu & White 1997).

The simplest kind of perturbations in the primordial plasma are density fluctuations in the cosmological fluid. In this case the overdense regions are colder (because photons must climb out of the potential well, losing energy) and hence there is a flow of hotter photons into these regions. These generate an $m = 0$ quadrupole anisotropy and therefore, thanks to Thomson scattering, a linear polarization in the CMB released at the epoch of recombination.

Vector perturbations represent vortical motions of the matter. Nevertheless the vorticity is damped by the expansion of the universe, as are all the motions which are not enhanced by gravity. For this reason vector perturbations are not expected to be relevant in the primordial plasma and to leave an imprint in the CMB polarization pattern.

The tensor geometrical pattern can be generated only by perturbations of the metric in the primordial universe, which can be viewed as gravitational waves. In particular we can consider a wave passing through the plasma which would distort a circle of test particles into an ellipse. This kind of distortion generates a quadrupole anisotropy which is not axisymmetric and, therefore, a net polarization in the CMB after Thomson scattering.

We can now consider the CMB anisotropies and distinguish whether they were generated by scalar or tensor perturbations in the primordial plasma. Hence we can compute the T/E/B power spectra (equation 1.34) for the two cases. Figure shows (1.7) the scalar (solid lines) and tensor (dashed lines) power spectra for both temperature and polarization anisotropies obtained from simulations. We notice several things by looking at this plot:

- scalar perturbations at the epoch of recombination generate both temperature and polarization anisotropies. Nevertheless the latter are generated only with the characteristic E-modes pattern in the sky. Tensor perturbations (which we recall are produced by the presence of primordial gravitational waves) on the contrary, contributes to the CMB temperature and polarization signal generating both E and B-modes.

- For temperature and E-modes, tensor perturbations leave an imprint in the power spectra which is smaller than the scalar one. We can parametrize the ratio between tensor and scalar modes at the time of recombination by introducing the r parameter, called the *tensor-to-scalar ratio*. The value of this parameter does not change the shape of the spectra, but only the normalization of the tensor modes. A smaller value of r implies lower tensor power spectra (the normalization of the spectra changes linearly with the value of r). Figure (1.7) is computed by considering $r = 0.1$ which, as described in the next section, is close to present upper-limit on its value.

- A polarized signal in the CMB radiation can be observed at large angular scales, for both tensor and scalar modes and for both E and B power spectra. This signal (shown on figure 1.7 with light green and pink colored lines) is due to CMB photons scattering off free electrons generated during the reionization epoch (happened at redshift $6 \lesssim z \lesssim 20$). The amplitude of the E and B-modes spectra at
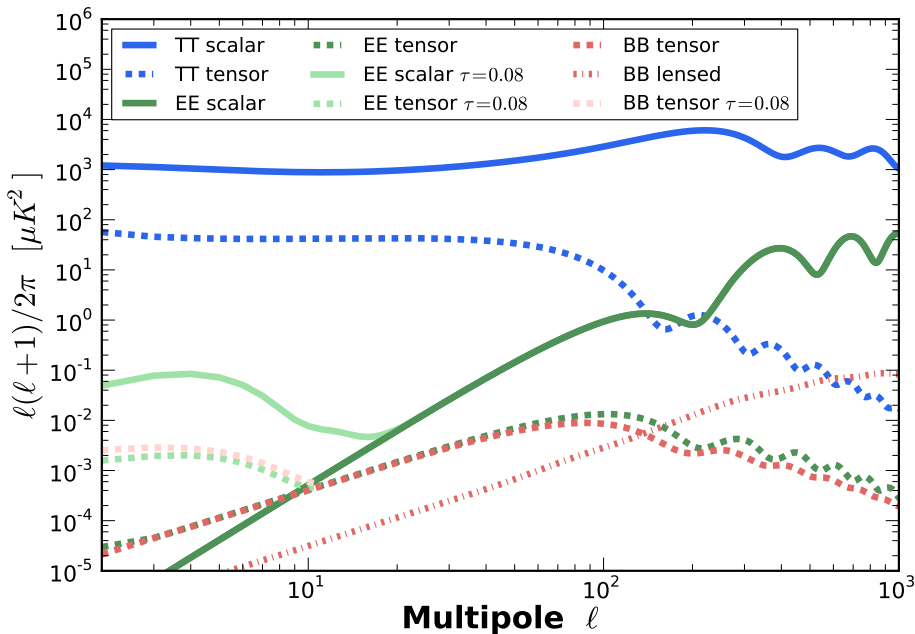
Figure 1.7: Temperature and polarization CMB angular power spectra. Solid lines show simulated spectra for scalar modes, dashed lines represent tensor modes ($r = 0.1$). Light green and pink lines represent the large scale spectra for $\tau = 0.08$. The dotted-dashed line shows the expected B-mode power spectrum from gravitational lensing. Spectra are obtained from sky simulations with the CAMB code (Web interface at `http://lambda.gsfc.nasa.gov/toolbox/tb_camb_form.cfm`).

large angular scales ($\ell \lesssim 20$) depends on the value of the optical depth of Thomson scattering τ. On figure 1.7 curves have been obtained considering $\tau = 0.08$ as constrained by Planck observations (see section 1.4.1).

- At small angular scales B-modes are generated principally by gravitational lensing. The presence of massive structure in our universe, such as galaxy clusters, can deviate the path of the CMB photons traveling from the last scattering surface toward us, generating secondary anisotropies and distorting the shape of the CMB power spectrum. This distortion affect both temperature and polarization power spectra. In particular for the polarization case, gravitational lensing can reshape the polarization pattern of the CMB, commuting E-modes into B-modes. This effect is larger for small angular scale, and dominates the B-modes power spectrum for multipoles $\ell \gtrsim 100$ (considering $r = 0.1$).

The inflationary paradigm together with the theory of primordial quantum fluctuations predicts the existence of tensor perturbations produced by gravitational waves in the early universe. The amplitude of their signature in the CMB polarization anisotropies, parametrized by the tensor-to-scalar ratio r, is strictly related to the energy scale of in-

flation according to the relation (see for example Baumann et al. 2009):

$$\mathcal{E}_{\text{inflation}} = 1.06 \times 10^{16} \, \text{GeV} \left(\frac{r}{0.01} \right)^{\frac{1}{4}}. \tag{1.35}$$

Detecting the B-modes signal in the CMB radiation at large angular scale, which we recall is generated only by primordial tensor perturbation, would thus give us an important evidence in favor of the inflationary paradigm, this is the reason why B-modes are often call the *smoking gun* of inflation. Moreover, reconstructing the B-modes power spectrum at low multipoles would allow to constraint the value of the r parameter and thus to shed light on the inflation process and the physics of the very early instant of our universe.

1.5.2 Status of observations and constraints on tensor-to-scalar ratio

In the past several years many experiments have been built with the primary scope of measuring and detecting the CMB polarized signal, pushing the sensitivity of the instruments as further as possible.

In 2002 the DASI (*Degree Angular Scale Interferometer*) experiment has been the first one to detect the polarized signal of the CMB, in the multipole range $300 < \ell < 450$, with the characteristic E-modes pattern (Kovac et al. 2002). Since then many other experiments were able to observe, study and characterize this polarized radiation. Recently, in particular, the Planck collaboration released the E-modes power spectrum obtained from its full sky observations of the CMB polarization (figure 1.9). As we have seen in
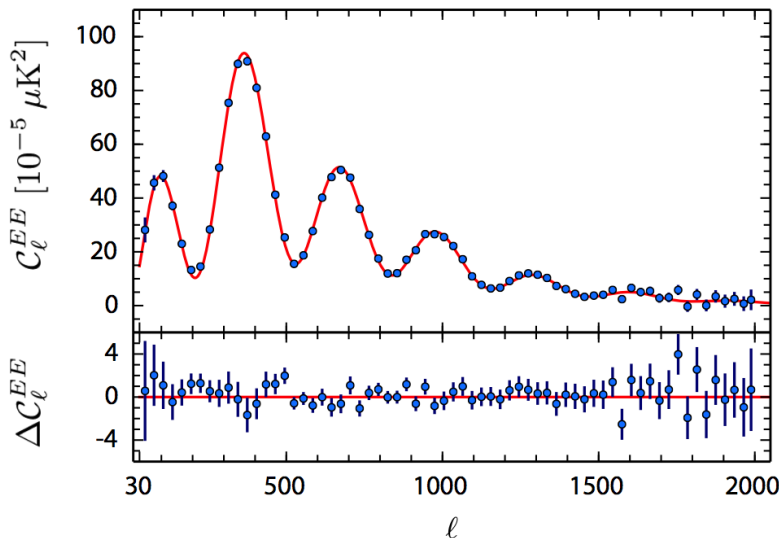

Figure 1.8: Planck E-modes power spectrum together with the best-fit model obtained considering also temperature data (red curve). On lower panel the difference between data and model is reported (Planck Collaboration XIII 2015).

the previous section, the low-ℓ part of the E-modes power spectrum can give us information on the reionization epoch of our universe and to constrain the value of the optical depth τ. From the joint analysis of the Planck temperature and E-modes power spectrum the value of τ has been obtain, as reported in section (1.4.1).

Even though the analysis of the E-modes of the CMB can give us extremely important information on the evolution of the universe, the detection of the CMB B-modes has become one of the biggest and most interesting challenges in modern observational cosmology. Figure (1.9) shows the status of B-modes observations (as before March 2014). Due to the extreme faintness of this signal none of the experiments reported in the plot was able to detect the primordial tensor signal and upper limits on the value of the r parameter have been obtained from these observations.
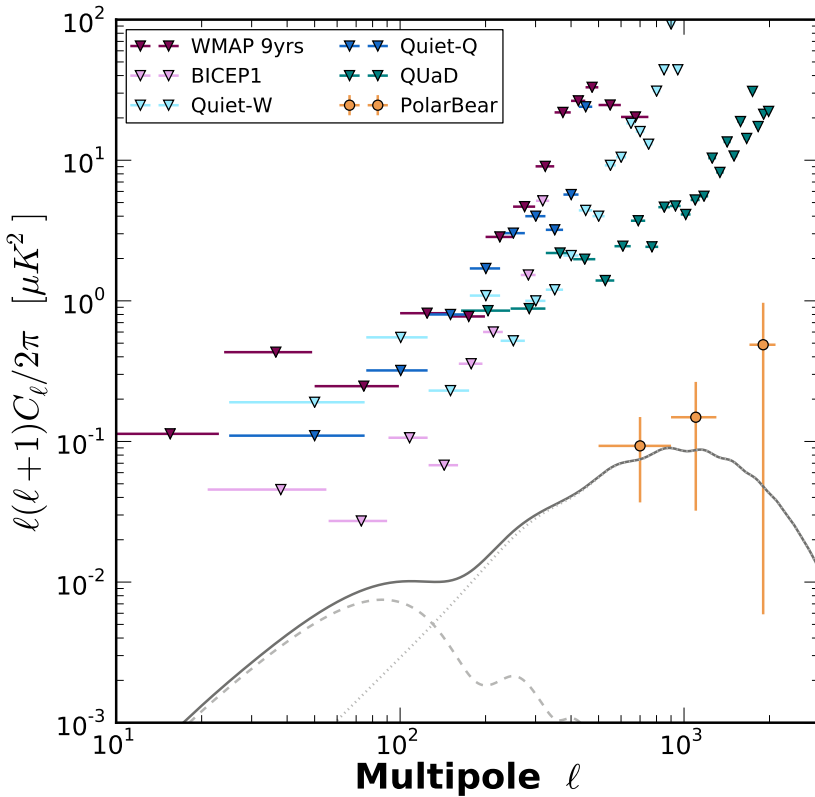
Figure 1.9: 95% confidence level upper limits on CMB polarization B-modes from several experiments (Bennett et al. 2013; QUIET Collaboration 2011, 2012; Brown et al. 2009; Barkats et al. 2014). Orange points represent the measurement of B-modes signal from gravitational lensing from PolarBear observations (Polarbear Collaboration 2014). Grey dashed line is the expected B-modes spectrum from primordial tensor mode ($r = 0.1$), dotted line is the expected signal from gravitational lensing (solid line is the sum of the two).

The BICEP1 (*Background Imaging of Cosmic Extragalactic Polarization*) experiment was the first microwave polarimeter designed specifically to target the B-modes signature of inflation in the CMB polarization. It consisted of 49 orthogonal pairs of polarization-sensitive bolometers observing at two frequencies (100 GHz and 150 GHz). A small aperture refracting telescope provided angular resolution of $\sim 0.93°$ and $\sim 0.60°$ at 100 and 150 GHz, respectively. BICEP1 operated from the Dark Sector Lab at Amundsen-Scott South Pole Station from January 2006 through December 2008. Data were collected during three seasons of observations of a small patch in the sky located in the so called "Southern Hole" which was thought to be a region with low emission of galactic foregrounds (right ascension and declination range in celestial coordinates of approximately $|\alpha| < 60°$ and $-70° < \delta < -45°$). Thanks to these measurements the BICEP1 collaboration set an upper limit on the tensor-to-scalar ratio, reporting a value of $r = 0.03^{+0.27}_{-0.23}$ corresponding to $r < 0.70$ at 95% confidence level (for a detailed description of the BICEP1 instruments and scientific results see Chiang et al. 2010; Barkats et al. 2014).

Planck polarization data also allowed to put upper limit on the value of r. In particular, thanks to the observations of the B-modes of the CMB, the value of r has been constraint to $r \lesssim 0.27$ at 95% confidence level (Planck Collaboration XI 2015). Moreover, since tensor modes also leave an imprint in the temperature signal, the value of the tensor-to-scalar ratio can be inferred also from these measurements. Thanks to Planck data the upper limit on r from the temperature power spectrum has been constraint to $r \lesssim 0.11$ at 95% confidence level, which represent to most stringent upper limit in the tensor-to-scalar ratio to date (Planck Collaboration XIII 2015).

BICEP2 is the successor of BICEP1, using the same small aperture telescope design but increasing the number of detectors in the focal plane reaching thus a higher sensitivity. BICEP2 operated from January 2010 through December 2012 observing the sky at a single frequency of 150 GHz. In March 2014 the BICEP2 collaboration published the first scientific results based on their observations (BICEP2 collaboration I 2014). They reported the detection of an excess in the B-modes signal in the multipole range $30 < \ell < 150$, inconsistent with the null hypothesis at a significance of $\gtrsim 5\sigma$. This signal has been originally interpreted as the first detection of primordial B-modes of the CMB polarization constraining the tensor-to-scalar ratio $r = 0.2^{+0.07}_{-0.05}$.

The analysis, verification and interpretation of the BICEP2 B-modes detection represent a large portion of the work done for this thesis and will be fully described and investigated in chapter 3.

At smaller angular scales, the B-modes polarization pattern can be generated by gravitational lensing. The first detections of this signal have been made in July 2013 and March 2014 by the SPT (*South Pole Telescope*) (Hanson et al. 2013) and Polarbear collaborations (Polarbear Collaboration 2014). Polarbear data are shown in orange on figure (1.9).

Challenges in observing CMB polarization: foregrounds and systematics

In this chapter, we review two of the main obstacles to the measurement of the B-modes polarization of the CMB, represented respectively by the diffuse emission from our own Galaxy and the instrumental performance in terms of overall sensitivity and control of systematic effects. These two topics represent the framework in which I developed the work done for this thesis, as described in the following chapters.

This chapter is organized ad follows: in section (2.1) the characteristics of the polarized Galactic foreground emissions are described and in particular the proprieties of synchrotron (2.1.1) and thermal dust radiation (2.1.2) are summarized. The level of contamination, arising from this kind of emissions, on CMB measurements is also reviewed in section (2.1.3) together with a brief explanation about the available methods for astrophysical component separation (2.1.4). In section (2.2) the principal systematic effects that may have significant impact on CMB observation are summarized, focusing, as usual, on the ones relevant for polarization measurements.

2.1   Polarized Galactic foregrounds

One of the main source of uncertainty in CMB precision measurements is the contamination by foreground emissions from our Galaxy. We do know, in particular, that Galactic synchrotron emission from cosmic ray electrons spiralizing around the lines of the Galactic magnetic fields dominates for low microwaves frequencies ($\lesssim 70\,\mathrm{GHz}$), while thermal dust emission from large molecules heated by starlight does at higher frequencies ($\gtrsim 100\,\mathrm{GHz}$).

Even though it is observationally evident that, in total intensity, CMB dominates at high Galactic latitudes over foreground emissions, this is not the case for polarization.

Indeed, both synchrotron and thermal dust emissions are partially linearly polarized with polarization degree which is not constant over the sky. The CMB B-modes signal, without considering the contribution from lensing, is at least one order of magnitude (and possibly more), fainter than the one in total intensity. This makes the foreground emission a source of contamination even far from the Galactic plane and, for this reason, the separation between cosmological and Galactic signals represents a great challenge.

In the next two sections we summarize the main properties of these foreground emissions basing our review on WMAP and Planck observations. We refer to general papers for more details (Planck Collaboration X 2015; Gold et al. 2011).

2.1.1   Synchrotron emission

Synchrotron emission results from the acceleration of cosmic rays electrons in the Galactic magnetic field. If we consider a power law spectrum, $N(E) \propto E^{-p}$, for the energy distributions of electrons propagating in a uniform magnetic field, the resulting emission is partially polarized with linear polarization fraction:

$$f_s = \frac{p+1}{p+7/3},$$

(2.1)

and aligned perpendicularly to the magnetic field (Rybicki & Lightman 1979). The frequency spectrum of the synchrotron emission can be described by a power law $T(\nu) \propto \nu^{\beta_s}$ (where T is the brightness temperature) with spectral index:

$$\beta_s = -\frac{p+3}{2}.$$

(2.2)

As described in the following, observations tell us that a typical value of this spectral index is $\beta_s \sim -3$, implying that synchrotron emission could have a polarization fraction as high as $f_s \sim 0.75$. This prediction is based on the assumption that the magnetic field is uniform. In practice one expects the orientation of the field to vary along the line of sight, reducing the degree of polarization observed.

The WMAP satellite observed the sky in five frequency bands centered at 22, 33, 41, 61 and 95 GHz. In the two lowest frequency bands (respectively K and Ka) the synchrotron radiation dominates the polarized maps, giving the possibility to gain information on spectral index and polarization fraction of the emission (Kogut et al. 2007). The recovered mean spectral index is $\langle \beta_s \rangle = -3.2$ with evidences of steepening from $\beta_s \sim -3.05$ along the Galactic plane to $\beta_s \sim -3.25$ at latitude $|b| > 30°$. To evaluate the polarization fraction, the total polarization of synchrotron in the K-band (defined as $P = (Q^2 + U^2)^{1/2}$) is compared with the unpolarized K-band synchrotron model (for details on how the model was constructed from the multi-frequency WMAP data see Hinshaw et al. 2007). The mean polarization fraction rises from $\sim 4\%$ near the Galactic plane up to $\sim 20\%$ at high Galactic latitude ($|b| > 50°$). Figure (2.1) shows the maps of
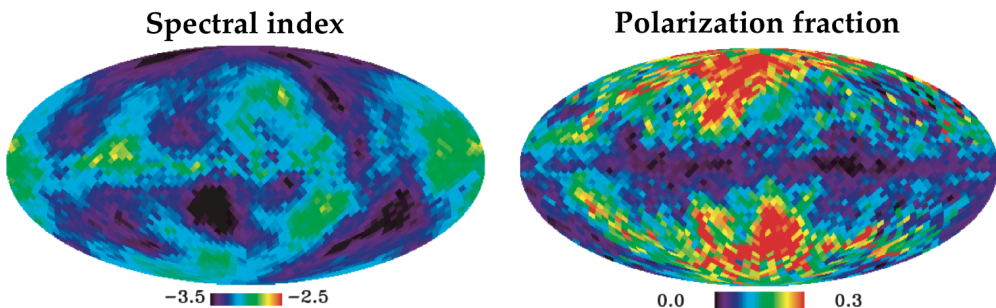

Figure 2.1: Synchrotron polarization polarization fraction (right) and spectral index β_s (left) maps as recovered by WMAP low frequency observations (Kogut et al. 2007).

synchrotron spectral index and polarization fraction as recovered by WMAP (three years of observations).

In Planck Collaboration X (2015) the full set of polarized sky maps at the seven frequencies of observations of the Planck satellite were used to recovered the most precise maps of polarized foreground emissions to date. To obtain these foreground maps the Galactic emissions have been disentangled from the CMB signal using a component separation algorithm based on parametric fitting (see section 2.1.4). Figure (2.2) shows the resulting Stokes Q an U maps of the synchrotron emission at the frequency of 30 GHz and at a smoothed angular resolution of 40 arcmin. From these maps it is possible to appreciate the complex morphology of the synchrotron emission on the Galactic plane, reflecting the tortuous structures of the Galactic magnetic field. Moreover, the emission extends at the very high Galactic latitudes following magnetic fields that elongated mostly perpendicularly to the Galactic plane.

2.1.2 Thermal dust emission

For frequencies $\gtrsim 100\,\text{GHz}$ the thermal emission from interstellar dust grains, mostly made of graphites and silicates, dominates. The frequency spectrum of thermal dust is well described by a modified blackbody with functional form $I_d(\nu) \propto \nu^{\beta_d} B_\nu(T_d)$, where $B_\nu(T_d)$ is the Planck spectrum. The temperature T_d is determined by the dust grain characteristics (such as composition and shape), the interstellar radiation field (causing heating) and efficiency of emitting far-infrared light of the dust grains themselves (causing cooling).

Photons emitted from thermal dust with aspherical shape can be polarized (Lazarian & Finkbeiner 2003), with dust grains emitting photons most efficiently along the longest axis. Combining this with the fact that the alignment mechanism tends to make the long grain axis perpendicular to the local magnetic field leads to linear polarization perpendicular to the magnetic field. The degree of alignment varies according to the size of dust grains, leading to a frequency dependent polarization.

WMAP highest frequency channel, at 95 GHz, is too low to get a signal to noise ratio in polarization high enough to well constrain the dust proprieties, particularly at high Galactic latitude. Planck, instead, with a frequency channel at 353 GHz sensitive to polarization, has recently permitted to obtain a first full sky map where the polarized emission of thermal dust dominates the observed signal. Figure (2.3) shows the Stokes Q and U maps of this emission at 353 GHz, smoothed at an angular resolution of 10 arcmin (Planck Collaboration X 2015). As for the synchrotron maps we can see that the thermal dust emission extends even far away from the Galactic plane.

Planck Collaboration Int. XIX (2015) reports an overview of the thermal dust emission in polarization at low and intermediate Galactic latitudes. Figure (2.4) shows the map of polarization fraction as measured by Planck. The map is masked excluding the 21% of the sky and has an angular resolution of $1°$. Similarly to synchrotron, the polarization fraction can reach up to $\sim 20\%$ is several large regions of the sky at intermediate latitude, while on the Galactic plane the typical polarization fraction is of few percent.

In Planck Collaboration Int. XXII 2015 the Planck and WMAP data in 12 frequency channels (from 23 GHz to 353 GHz) are used to determine the spectral index β_d of the thermal dust emission both in intensity and polarization. In particular, data show that

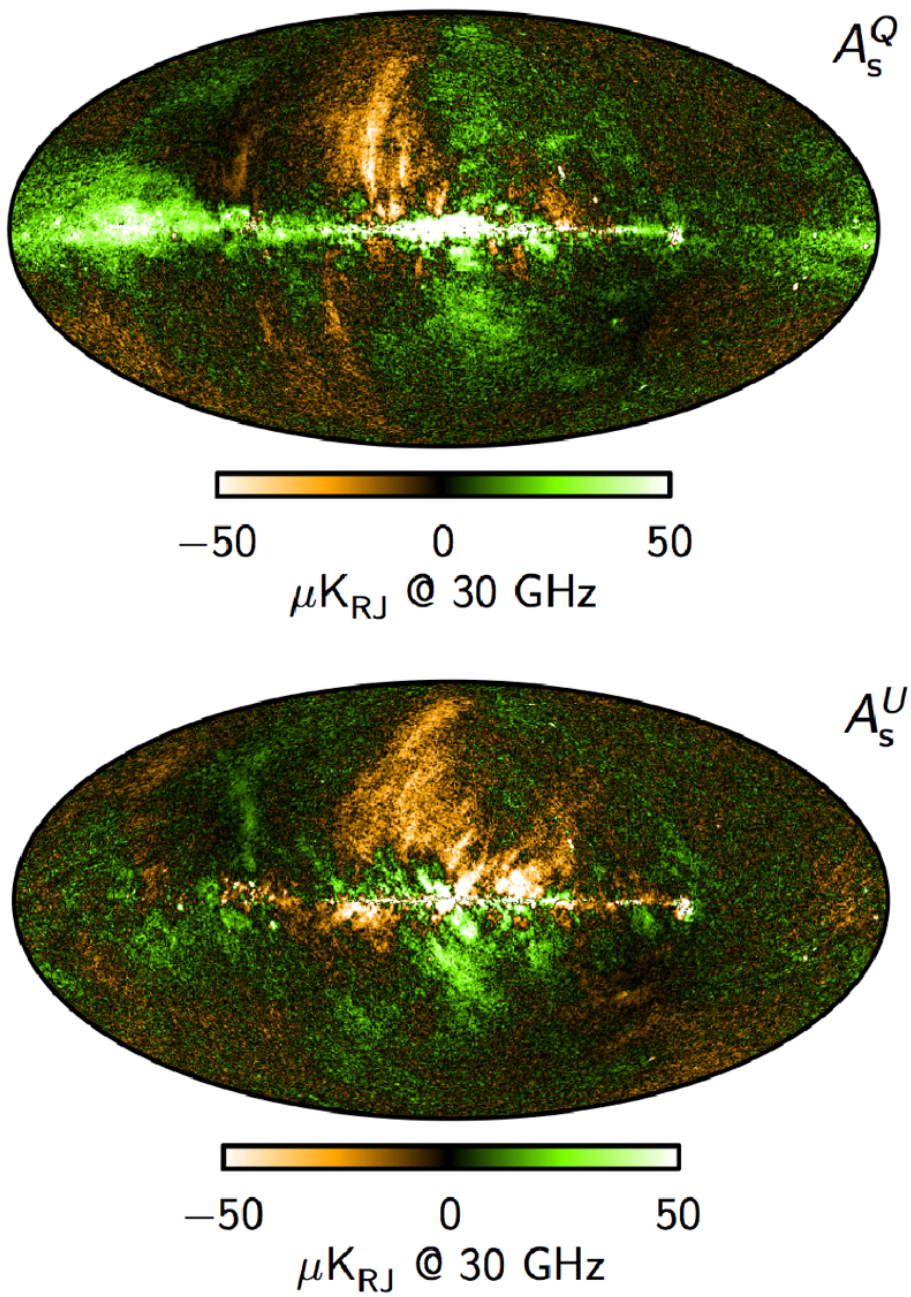**Figure 2.2:** Stokes Q and U maps of polarized synchrotron emission at 30 GHz, smoothed to an angular resolution of 40 arcmin, recovered from Planck observations (Planck Collaboration X 2015).
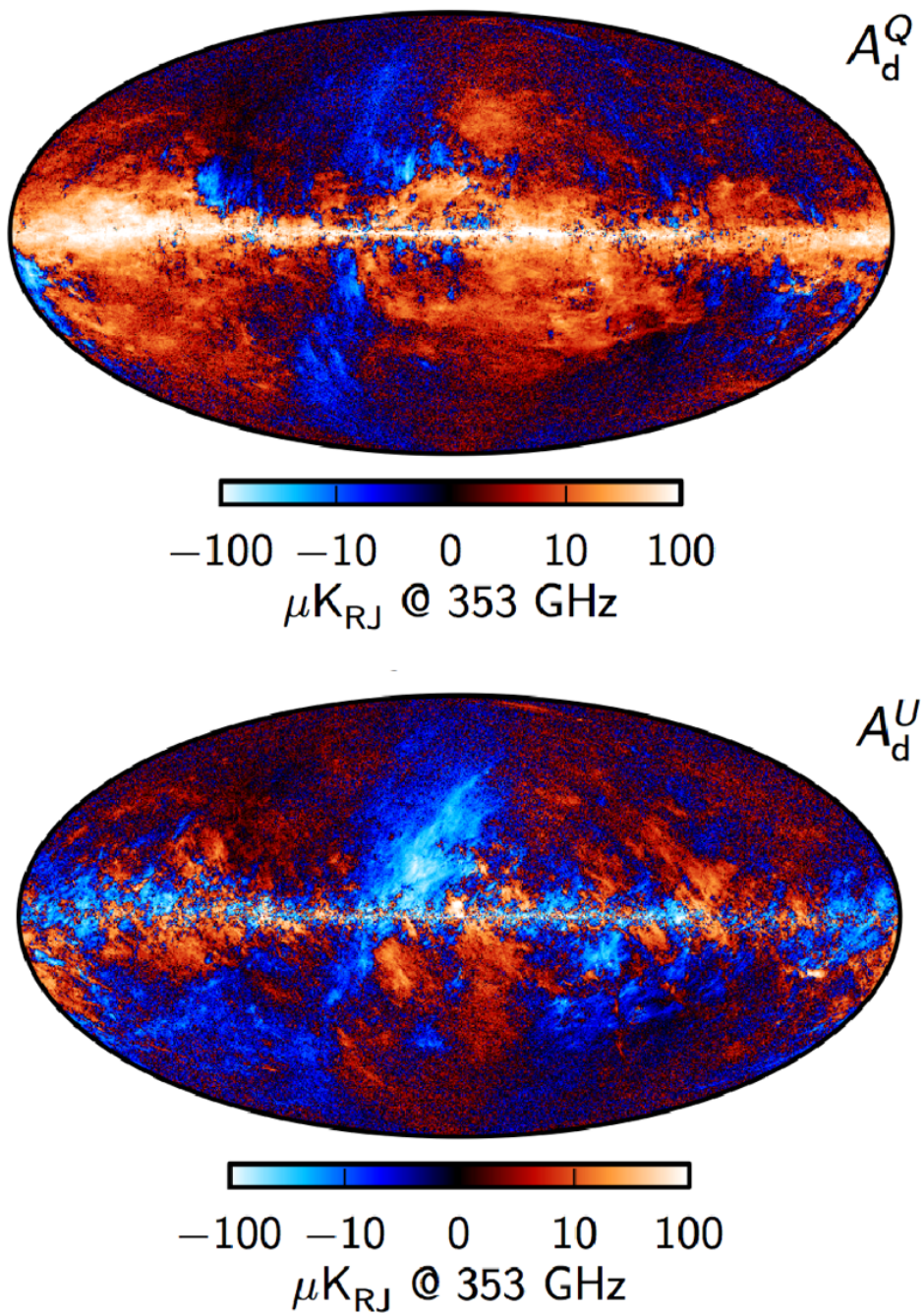
Figure 2.3: Stokes Q and U maps of thermal dust polarized emission at 353 GHz, smoothed to an angular resolution of 10 arcmin, recovered from Planck observations (Planck Collaboration X 2015).
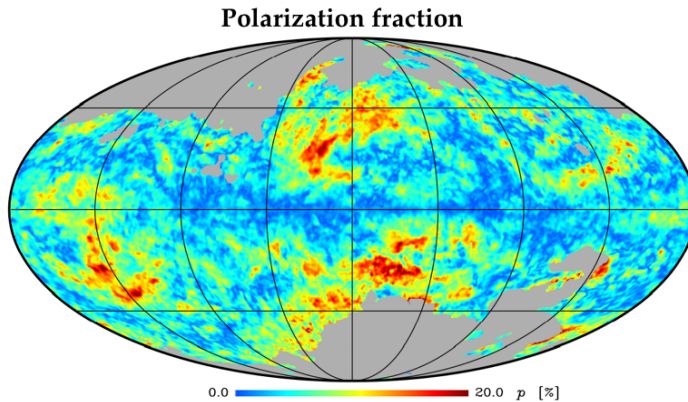
Polarization fraction

Figure 2.4: Polarization fraction at 353 GHz as observed by Planck. The map is at $1°$ angular resolution on 79% of the sky (Planck Collaboration Int. XIX 2015).

the Spectral Energy Distribution (SED) of this kind of emission in polarization between 100 and 353 GHz is consistent with a modified blackbody law with spectral index $\beta_d = 1.59$ for $T_d = 19.6\,\mathrm{K}$. This spectral index has been obtained for 400 circular regions with radius of $10°$ at intermediate Galactic latitude on 39% of the sky and appears to be quite constant among these patches with a dispersion of 0.17 for a constant temperature T_d.

Part of this thesis addresses the study and characterization of the thermal dust emission at high Galactic latitude aiming to understand its impact on recent CMB polarization measurements, as described and analyzed in chapter (3).

2.1.3   Contamination for CMB observations

Figures (2.2) and (2.3) show how the structures of the foreground emissions in polarization extend at high Galactic latitude for both synchrotron and thermal dust radiations implying that they can contaminate the CMB observations even when looking far away from the Galactic plane.

In Planck Collaboration X (2015) this level of contamination is estimated by calculating the RMS of the foreground polarized maps at the various Planck frequencies and by comparing that with the CMB one. Figure (2.5) shows the result of this calculation. The RMS is computed on the retrieved synchrotron, thermal dust and CMB polarization maps, at the Planck frequencies, smoothed to 40 arcmin angular resolution and on sky fraction between 73 and 93% (corresponding to the lower and upper edges of each line). The plot shows how the Galactic foreground dominates over the CMB signal at all the frequencies, having a minimum of the emission close to 70 GHz.

Another way to estimate the level of contamination from polarized foreground emission for the CMB observations, is to calculate B and E-modes power spectra of the Planck maps and compare them with the expected CMB spectra. For each Planck frequency channel we computed the cross-spectrum of the two "Half-Ring" (HR) independent maps. To obtain the two HR maps the approximately 60 circles scanned during a sta-
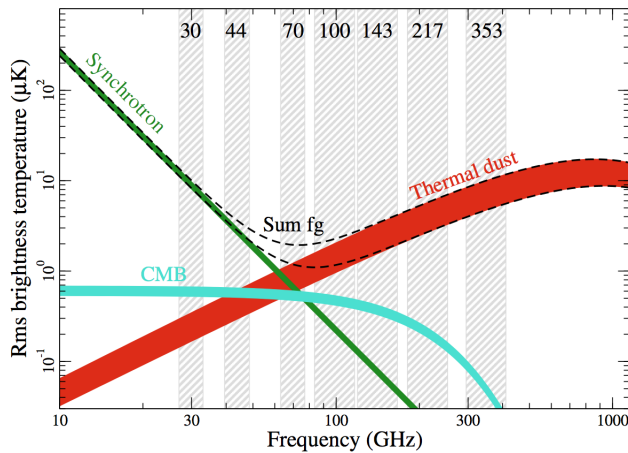
Figure 2.5: Brightness temperature RMS as a function of frequency and astrophysical components for polarization emission. The rms is calculated on maps at angular resolution of 40 arcmin on sky fraction between 73 and 93%, corresponding to the lower and upper edges of each line. (Planck Collaboration X 2015).

ble pointing period are divided into two independent subsets of 30 circles (see Planck Collaboration VI 2014 for details). The resulting maps have uncorrelated white noise and computing the cross-correlation between them leads to noise unbiased spectra. Figure (2.6) shows the resulting spectra. These spectra represent a generalization of those shown in Page et al. (2007) which were obtained from WMAP data (see figure 17 on the paper). They are computed on the same portion of the sky, the so called P06 mask (also shown in figure 2.6, upper panel) which masks the 25.7% of the sky, mostly near the Galactic plane, leaving the remaining 74.3% of the sky available for data analysis.

Spectra in figure (2.6) are for all the seven Planck frequency channels and are computed with the *CrossSpect* algorithm to correct for the incomplete sky coverage (see section 3.3.1) considering a multipole binning with $\Delta\ell = 10$. These spectra confirm that, even at intermediate and high Galactic latitude away from the Galactic plane, the foreground emission dominates over the expected CMB signal (shown as black dashed lines on the plot, for BB spectra we consider the presence of tensor signal with $r = 0.2$) at large angular scales. In particular, at LFI frequencies the synchrotron Galactic emission for the E-modes dominates over CMB for $\ell \lesssim 100$ even at the highest frequency of 70 GHz. For the B-modes case we have noise dominated spectra for $\ell \gtrsim 100$, but at lower multipoles Galactic emission is larger than the expected CMB one of at least one order of magnitude at 70 GHz up to about three orders of magnitude at 30 GHz.

For the HFI channels we have a similar situation. At 100 GHz, the thermal dust polarized Galactic signal dominates over the CMB one for $\ell \lesssim 100$ in the E-modes spectrum. Comparing the plots for the LFI and HFI we can conclude that the minimum of foreground polarized emission lies at frequencies between 70 and 100 GHz. At higher frequencies the level of foreground emission increases and at 353 GHz, in this region of the sky, dominates over the CMB even at the smaller angular scale with $\ell \sim 10^3$. Looking at the B-modes spectra for the HFI case we can clearly see how the Galactic emission ab-
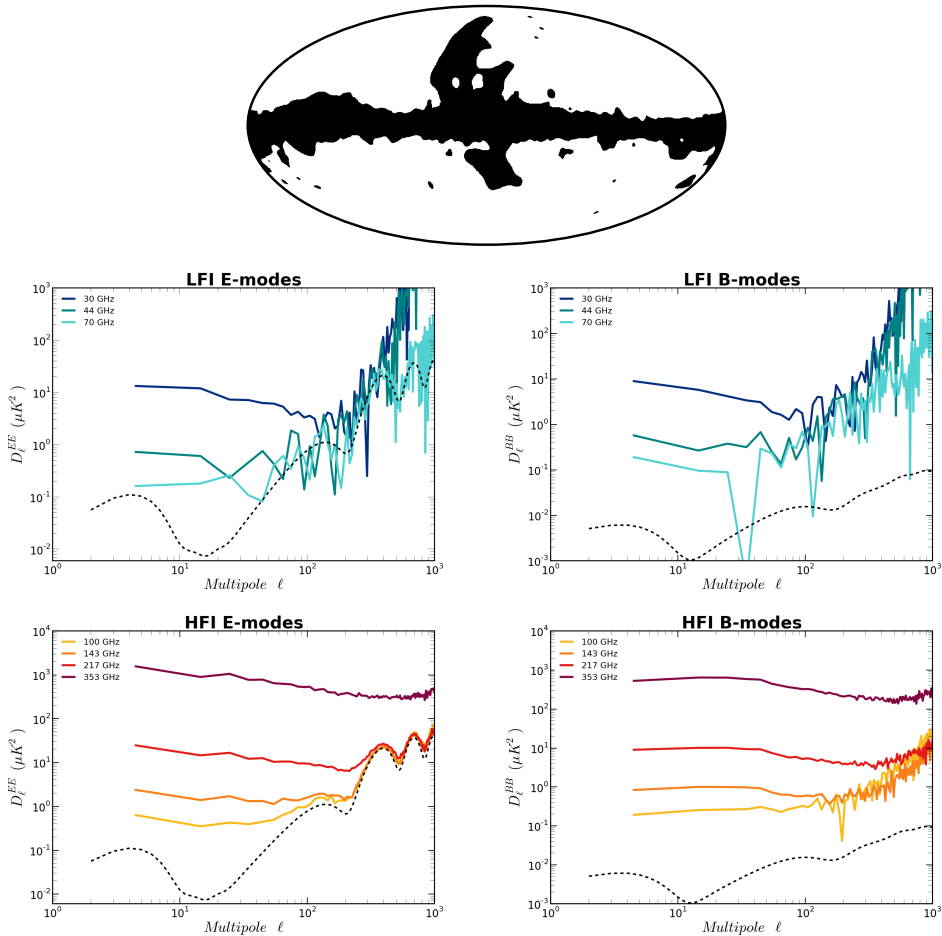
Figure 2.6: Planck E-modes and B-modes power spectra on P06 mask (the mask is shown in the upper panel, white area is the sky region left for analysis). For each channel the spectra are computed by cross-correlating the HR1 and HR2 maps. Dashed lines are the expected CMB spectra.

solutely needs to be taken into account to perform any measurement of the CMB signal on large portion of the sky.

In the next section we will briefly review the component separation methods which allow to isolate the cosmological signal from the foreground emission. Moreover, chapter (3) is precisely focused on the contamination from polarized thermal dust radiation on CMB observations at high galactic latitude and it presents a detailed analysis of the characteristics of this kind of emission.

2.1.4   Component separation methods

We have seen in the previous section how foreground contamination represents a great challenge for the measurement of CMB polarization. In the past several years the problem of the separation of the different astrophysical emissions from the cosmological

signal has been deeply investigated and different methods to perform this component separation have been developed. Even though in this thesis we do not report the application of these methods to the cases we have studied, we briefly review them in this section, for completeness.

The feasibility of component separation is based on the fact that the CMB and the foreground emissions present different frequency dependencies and are expected to be uncorrelated. CMB has a pure blackbody spectrum, while foreground has its own behavior, depending on the particular kind of emission (for example, power law frequency dependence for synchrotron emission or modified blackbody radiation for thermal dust). For this reason, in order to isolate the CMB signal, multi-frequency observations of the sky are essential. The framework in which this topic has reached its maximum exploitation so far is represented by the Planck component separation efforts in total intensity (Planck Collaboration XII 2014) and polarization (Planck Collaboration IX 2015).

One approach to perform the component separation is the so called parametric fitting. In this case, assumptions on the characteristics of the different emissions are made, meaning that their frequency spectra are parametrized. The values of these parameters needs to be fitted by using the multi-frequency observations. In this way the maps of the different foreground emissions are recovered and then removed form the measured sky maps, to isolate the CMB signal (Eriksen et al. 2006; Stompor et al. 2009). We can assume that the observed data take the form of a multi-frequency set of sky maps (d_ν) each of which may be written in the form

$$d_\nu = As_\nu + n_\nu \tag{2.3}$$

where ν identifies the frequency bands, $\mathbf{s}_\nu$ is a vector containing the unknown values of Stokes parameters for each of the n_c components and $\mathbf{n}_\nu$ is the instrumental noise. $A \equiv A(\beta)$ is a component "mixing matrix", which is assumed to be parameterized by a set of unknown parameters $\{\beta_i\}$. These parameters usually consist in the spectral indices and amplitude of the various astrophysical components which, in general, vary from pixel to pixel on the maps. Without going into the details, from this definition and model it is possible to define a likelihood function retrieving the estimated values of the parameters via standard Maximum Likelihood techniques and therefore reconstructing the maps of the different foreground emissions.

A second approach is the so called minimum variance method. In this case the only assumption which is made concerns the spectral behavior of the CMB radiation (blackbody spectrum), and no other prior on the foregrounds is considered. With a multi-frequency set of sky maps, the CMB signal is retrieved by performing a linear combination of them:

$$s_{CMB} = \sum_\nu w_\nu d_\nu \tag{2.4}$$

where the w_ν represents the weight given at each single map d_ν at frequency ν. Imposing the condition of a blackbody spectrum for the CMB radiation implies having $\sum_\nu w_\nu = 1$. The weights are obtained by minimizing the variance of s_{CMB} component.

We have described here the two different approaches for component separation applying them to the map domain. Nevertheless parametric fitting and minimum variance can be efficiently applied to other domains, for example the harmonic one or the needlet (wavelet) one.

In Planck Collaboration IX (2015) four different implementations of the above criteria were exploited, corresponding to parametric fitting in the pixel and harmonic domain, and minimum variance in the pixel and needlet spaces. CMB reconstruction and foreground separation were efficiently achieved (within the limits of the Planck performance) in total intensity, and for Q/U Stokes parameters. Nevertheless, the setup of current experiments, with non optimal sensitivity in the very low and very high frequency channels, does not permit to perform foreground cleaning with the accuracy needed to recover the faint CMB B-modes signal. Current experiments are equipping themselves with appropriate foreground monitoring channels in order to include the B-modes component separation within their data analysis pipeline.

2.2   Instrumental systematic effects

A second critical aspect for CMB observations is the control of instrumental systematic effects. Indeed, accurate measurements of the CMB signal require instruments with very high sensitivity. This is true for observations of temperature anisotropies of the CMB (which we recall are of the order of 10^{-5} K), but the situation is even more dramatic for observations of the polarized signal and in particular the B-modes power spectrum.

The RMS on Q and U maps of a B-modes CMB signal with $r = 0.1$ is of the order of $8 \times 10^{-2}\,\mu$K (at 1 degree angular resolution), implying that we need instruments with a sensitivity of few tens of nK. To reach such a high sensitivity we need complex instruments composed by large arrays of detectors. Moreover, pushing the sensitivity to this level, requires an extremely good knowledge of the instruments to achieve a remarkable control of systematic effects which can contaminate the measurements.

In this section we briefly review the main systematic effects impacting on CMB measurements. A detailed analysis of instrumental systematic effects would require a full description of the different instruments which are usually used to perform CMB observations. Such a description is beyond our purpose which is to allow the reader to understand the several criticalities that a CMB experiment must face. Moreover, the general review that we report here is useful to introduce one of the topic of this thesis. In chapter (4), indeed, we analyze the impact of possible systematic effects on the measurements of a future CMB experiment, called *Large Scale Polarization Explorer*. In this section, we focus our description mainly on those effects that have an impact Planck measurements, since in this work we analyzed data coming from this satellite.

We can classify the possible systematic effects in three categories (as in Planck Collaboration III 2014, 2015): (i) effects which are independent of the sky signal; (ii) effects which couple with the observed sky signal and impact both total intensity and polarization observations; (iii) effects which specifically have an impact only on polarization measurements. In the following sections we give a brief description of the principal effects in each of these categories.

2.2.1   Effects independent of the sky signal

Some systematic effects are characteristic of the instrumentation used in the experiments and do not depend and couple with the observed sky signal. Here we describe two specific examples within this category.

1/f noise due to amplification in radiometers: in radiometric detectors a $1/f$ noise component is present due to long term instability in the amplification of the signal. This effect is typically suppressed by making use of radiometers with pseudo-correlation differential design, as for the Planck-LFI and WMAP instruments (see for example Seiffert et al. 2002). Residual long term variations can be minimized by using a destriping technique, which during the map making process, minimizes the discrepancies between multiple observation of the same single pixels in the sky (Maino et al. 1999), leading, in the LFI case, to negligible effect on the final sky measurements.

Spurious fluctuations in the detected signal: the signal detected by instruments can be contaminated by the presence of fluctuations that do not depend on the observed sky emission.

In bolometric instruments (as the Planck-HFI instrument, see appendix A), this kind of fluctuations can, for example, arise from cosmic particles hitting the bolometer grid or thermometer, causing spikes in the timelines.

Differently, the LFI detected signal is affected by systematic periodic fluctuations at various frequencies, some generated by thermal instabilities in the focal plane, some caused by a spurious cross-talk between the scientific and housekeeping data causing a 1 Hz square wave in the data. This latter effect is modeled using templates obtained from flight radiometric data and removed from science data (Mennella et al. 2011).

2.2.2 Effects dependent on the sky signal

Several instrumental systematic effects have an impact on final sky measurements that critically depends on the observed sky signal and sky scanning strategy. We report here some key examples.

Main beam asymmetries: optical beams can present asymmetries which need to be taken into account to recover the correct beam window functions and properly deconvolve the observed signal to compute angular power spectra.

New generation of CMB experiment often consist of very large array of detectors, up to thousands of detectors, located in wide focal planes. On such large focal planes, it is not always possible to optimize the detector beam proprieties, especially for detectors located at the edges of the focal surface, which therefore can be asymmetric. These asymmetries, if not properly taken into account in the beam window function, can also cause spurious polarization signals, critical for polarization measurements (Carretti et al. 2004). A proper characterization of the beam proprieties is therefore essential and can be achieved during the instrument test phase or by observing specific point sources (such as Jupiter) during sky signal measurements.

Straylight contamination: the light incident on the focal plane that does not reflect directly off the primary mirror (straylight) can be a major source of systematic effects, especially when the Galactic plane intersects the direction of the main spillover. This effect is therefore larger at the lowest and highest observing frequencies, where the Galactic signal is stronger.

In Planck-LFI, for example, the fraction of power intercepted by intermediate side-lobes (at less than $5°$ from the main beam) ranges from 0.02% to 0.08% of the total beam power, while for the far sidelobes it ranges from 0.18% to 0.68% (Planck Collaboration III 2014). The pickup from the intermediate sidelobes appears to be negligible, while, in this case, the effect caused by far sidelobes needs to be corrected. In particular, in the LFI data processing, the far sidelobes convolution with the Galactic signal is simulated and removed directly from the data time streams (Planck Collaboration II 2015).

Pointing uncertainties: errors in the reconstruction of the pointing direction can reflect into uncertainties in pixel total intensity and polarization measurements. In particular, if pointing uncertainties are not constant in time, the statistics of the sky anisotropy measurements may be not preserved, with a impact on angular power spectra. Typically this effect is larger for small angular scales, where, nevertheless, the CMB polarized signal is stronger (for B-modes is dominated by lensing) and, therefore, usually it does not have a critical impact.

ADC non linearity: A wide dynamic range at the ADC input is needed in CMB experiment to measure both the CMB and the Galactic foregrounds. Non-linearity in the ADC response over the entire dynamic range can be present, reflecting essentially in calibration errors.

In Planck, both LFI and HFI instruments are affected by this problem which is corrected using specific templates in the data processing phase (Planck Collaboration II 2015; Planck Collaboration VII 2015).

Imperfect responsivity calibration: responsivity calibration is another critical aspect of CMB experiments. Typically, for an experiment sensitive to unpolarized radiation, calibration is performed observing radiation coming from planets or using the CMB Solar Dipole, caused by the motion of the Solar System with respect to the CMB rest frame. In polarization, bright and well characterized polarized sources in the sky are needed. Calibration errors, in general, lead to uncertainties in the normalization factor of the recovered angular power spectra. Moreover, if calibration is performed several times during sky observations (as in the Planck case, see Planck Collaboration V 2014; Planck Collaboration VIII 2014), calibration errors couple with the sky scanning strategy possibly affecting the recovered power spectra.

Bolometers long time constant: the detector time response is a key calibration parameter for bolometers. It describes the relation between the optical signal incident on the detectors and the output of the readout electronics. This relation is characterized by a time shift, which depend on the incoming optical signal. It is described by a linear complex transfer function in the frequency domain, which must be used to deconvolve the data in order to correct the time shift, which otherwise significantly distorts the sky signal. A description on how this transfer function is recovered and used to correct data in the HFI instrument is reported in Planck Collaboration VII (2015).

2.2.3 Effects impacting polarization measurements

Leakage effects can have a not negligible impact on measurements of CMB polarization. Two type of leakage effects are possible: total intensity radiation which leaks into the detected linearly polarized signal ($I \rightarrow Q/U$ leakage), or a mixing between the Stokes Q and U sky signals ($Q/U \rightarrow U/Q$ leakage).

Several non-idealities, that depend on the instrument architecture and characteristics, can cause these leakage effects. In section (4.4) we analyze in detail the possible non-idealities that can affect polarimeters based on radiometric technologies.

I $\rightarrow$ Q/U leakage: this kind of effect can have a relevant impact on final measurements of both CMB polarization and Galactic foreground emissions. This is because, as we have seen in previous sections, the signal emitted in total intensity is larger than the polarized one, for both CMB and foregrounds (up to more than one order of magnitude for CMB B-modes). Minimizing this effect in hardware and, eventually, developing strategies to remove the residuals from the data is therefore essential to obtain clean polarization measurements.

Q/U $\rightarrow$ U/Q leakage: typically the main source for this kind of effect is the uncertainty on the polarization angle of detectors. Values of the Stokes Q and U parameters depends on the chosen reference frame. Since each detector measures Q and U in its own reference frame, knowing the detector polarization angle is essential to report all the measurements in a unique coordinate system. If Q and U are the values of Stokes parameter of the sky radiation, in the astronomical coordinate frame[1], and Q' and U' the measured values in the detector coordinate frame we have that:

$$Q = Q' \cos(2\theta) - U' \sin(2\theta) \quad \text{and} \quad U = Q' \sin(2\theta) + U' \cos(2\theta) \tag{2.5}$$

where θ is the detector polarization angle. Uncertainties in the detector polarization angle leads, therefore, to $Q/U \rightarrow U/Q$ leakage. The final impact on E and B-modes power spectra depends on the uncertainty level, the characteristics of the instruments and also on the sky scanning strategy.

---

[1]Astronomical convention takes $\hat{x}$ along the local meridian towards the north direction and and $\hat{y}$ along the local parallel towards the east, in the chosen coordinate system (i.e. galactic, equatorial or ecliptic).

Part I

Foreground contamination: the Planck & BICEP2 case

Planck observation of polarized dust at high galactic latitude

In this chapter we summarize the recent Planck results on polarized thermal dust radiation at high Galactic latitude, focusing our analysis on the contamination of this kind of emission on CMB measurement of B-modes polarization. In particular, we will focus on the relevance that diffuse Galactic foregrounds have on the observations of the BICEP2 experiment.

This chapter is organized as follows: in section (3.1) we review the results obtained from the three seasons of observations of the BICEP2 telescope. These results, and their original interpretation in terms of primordial gravitational waves caused a great debate in the scientific community, bringing upfront the key role of polarized foregrounds. In section (3.2) we summarize the general results about the proprieties of the polarized dust at high Galactic latitude obtained from Planck data. Section (3.3) contains the bulk of my work on this topic, concerning the contamination of foreground emission in the field observed by the BICEP2 experiment. In section (3.4) we report the results of the BICEP2/Planck joint analysis. Finally in section (3.5) we draw the conclusions on this analysis.

3.1 BICEP2 detection of B-modes signal

The BICEP experiments have been specifically designed to search for primordial B-modes of the CMB polarized radiation on degree angular scales, by making very deep maps of relatively small patches of sky from the South Pole.

BICEP1 observations of the sky, carried out from January 2006 through December 2008, allow to put an upper limit on the tensor-to-scalar ratio corresponding to $r < 0.70$ at 95% confidence level (see section 1.5.2).

BICEP2 was the successor of BICEP1 and differed principally in the focal plane, where a very large increase in the detector count resulted in more than an order of magnitude improvement in mapping speed. BICEP2 observed essentially the same region of the sky as BICEP1, for three seasons from 2010 to 2012. The instrument was equipped with a 26 cm aperture telescope (same as BICEP1) provided with 512 antenna coupled bolometers in the focal plane. The bolometers worked at the single frequency of 150 GHz and each of them had a temperature sensitivity of $\sim 300 \, \mu K_{CMB} \sqrt{s}$ (The BICEP2 instrument is fully described in BICEP2 collaboration II 2014). The observed region of

the sky has an effective area of about 380 square degrees. The final reached sensitivity is of ~ 87 nK on Stokes Q and U maps with an angular resolution of about $0.5°$.

Here we summarize the scientific results obtained from the BICEP2 observations and their initial interpretation, as reported in BICEP2 collaboration I (2014).

The data analysis procedure is fully described in the cited paper. Nevertheless, to understand the analysis described in the following sections, it is important to highlight here few important steps of this pipeline. In the data processing, time ordered data coming from the detectors are first filtered to remove any scan synchronous component. Filtering the data implies mixing of E and B-modes. This problem arises also because of the limited sky coverage and affects all CMB experiment where a sky cut is performed. Data need a correction (also referred to as "purification") to recover the pure E and B-modes power spectra (or maps) to get reliable results. This problem and the power spectrum estimator algorithms able to address it are discussed in section (3.3.1).
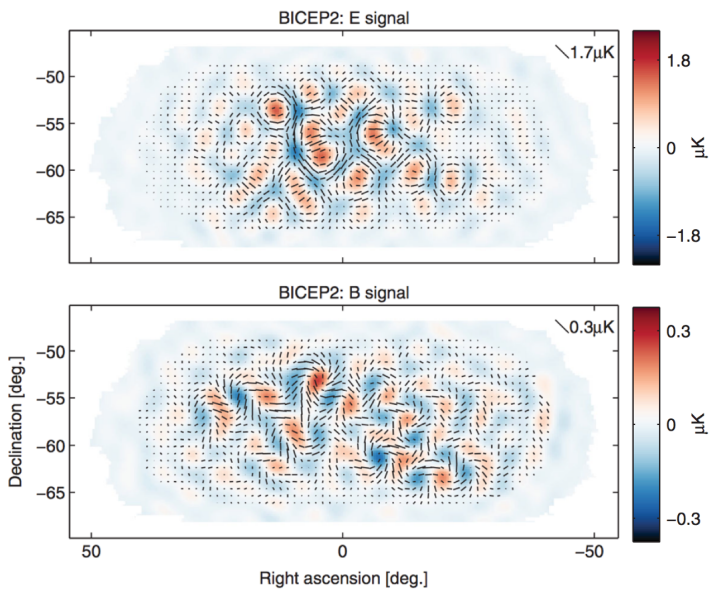

Figure 3.1: BICEP2 pure E-modes and B-modes maps. Segments represent the polarization orientation (BICEP2 collaboration I 2014).

Figure (3.1) shows the pure E and B-modes maps observed by the BICEP2 instrument, as obtained after purification. A clear B-modes pattern is detected, with a peak-to-peak amplitude of $\sim 0.6\,\mu$K (30 arcmin angular resolution). This signal appears to be evenly distributed over the field, as expected for a cosmological signal.

Figure (3.2) shows the B-modes power spectrum calculated from the previous map. This spectrum has been computed considering nine multipole bins (bandpowers) spanning the range $20 < \ell < 340$. At low multipoles ($\ell < 150$) the data show an excess. Compared to the expectation of a pure gravitational lensing spectrum (solid red curve), this excess has a high signal-to-noise ratio and is compatible with the predicted signal of primordial B-modes with tensor-to-scalar ratio $r \neq 0$. In particular considering the first
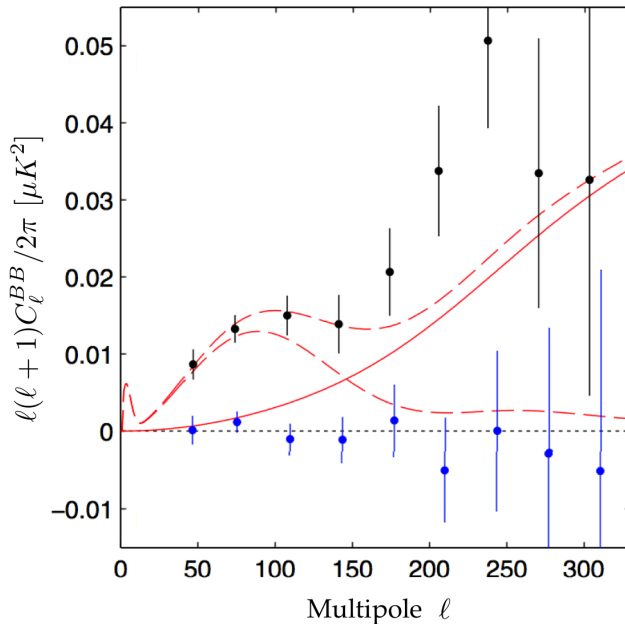
Figure 3.2: B-modes angular power spectrum as computed from BICEP2 maps (figure 3.1). The spectrum obtained from the data (black points) shows an excess over the signal expected from pure gravitational lensing (solid red line) at angular scale of $\sim 1°$. This is compatible with primordial gravitational waves with $r = 0.2$ (red dashed lines). Blue point represent the result of null-test obtained from temporal split data (see text) (BICEP2 collaboration I 2014).

five multipole bins, the most likely value for the tensor-to-scalar ratio, obtained from a maximum likelihood analysis, is $r = 0.20^{+0.07}_{-0.05}$ (68% confidence interval).

The BICEP2 collaboration checked for the presence of residual systematic effects in the data which could have caused the observed signal (see section VIII in the paper). All the effects were found to be negligible and thus unlikely to affect the measurements. In figure (3.2) blue points represent the temporal-split null-test. This spectrum is computed from a null map obtained considering different temporal data subsets. As expected, the spectrum is consistent with zero, ruling out a significant contamination by systematic effects.

We mention that a detection of primordial B-modes with $r = 0.2$ is in tension with the previous upper limit on r obtained from the Planck temperature data ($r < 0.11$, see section 1.5.2). One modification to relieve this tension is to allow the initial scalar perturbation spectrum to depart from the simple power law form, which is assumed in the base ΛCDM model (section 1.4.1). A standard way in which this is done is by introducing a "running" parameter $dn_s/d\ln(k)$ (with k the wavenumber of the primordial perturbation and n_s the power law spectral index). By adding this modification to the model the Planck constraint relaxes to $r < 0.26$ (Planck Collaboration XVI 2014).

A significant contamination to BICEP2 CMB observations can come from the Galactic foreground emission. In particular, as seen in chapter 2, at 150 GHz (frequency of observation of the BICEP2 instrument) polarized emission of thermal dust starts to be domi-

nant and can be an important factor of contamination for CMB measurements event at high Galactic latitudes. At the time when the BICEP2 paper was submitted, no public data of thermal dust emission in polarization were available. The BICEP2 team estimated the level of foreground contamination to the observed signal using several existing models of thermal dust emission and found no evidence for relevant contamination.

The Planck satellite with full sky coverage and its polarization sensitive frequency channels at 100, 143 and 353 GHz gives the unique capability to shed light on this topic. Part of the work for this thesis has been done with this purpose, with the primary goal to understand the characteristics of the polarized dust emission at high Galactic latitude and, in particular, in the BICEP2 field, as explained in the following sections.

3.2   Polarized dust emission at high galactic latitude

In this section we summarize the results obtained from Planck 353 GHz data on the characteristics of thermal dust emission at intermediate and high Galactic latitudes. These results are reported in a paper published in september 2014 with the title "Planck intermediate results. XXX. The angular power spectrum of polarized dust emission at intermediate and high Galactic latitudes" and accepted for publication on the international scientific journal *Astronomy and Astrophysics* (Planck Collaboration Int. XXX 2014, hereafter PIPXXX). The analysis concerns the estimation of the angular power spectra of thermal dust in polarization, on different regions of the sky. It includes also the study of the BICEP2 observed region and on this last point in particular, my work has been focused, has described in section (3.3).

Six large regions of the sky have been selected, in order to measure the dust polarization power spectrum with high signal to noise ratio with an effective coverage of the sky from 30 to 80% (figure 3.3). The details about the selection process are reported in section 3.3.1 of the article.

The angular power spectra at 353 GHz are estimated from Stokes Q and U maps by cross-correlating the so called HFI "Detector-Set" (DS) maps obtained using two distinct subsets of polarization sensitive bolometers. This procedure cancels uncorrelated noise minimizing the noise bias in the spectra.
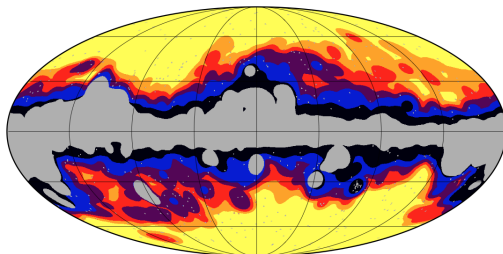

Figure 3.3: Masks and complementary selected large regions that retain fractional coverage of the sky f_{sky} from 0.8 to 0.3. The retained regions can be identified by the colors yellow (0.3) to black (0.8), inclusively (Planck Collaboration Int. XXX 2014).
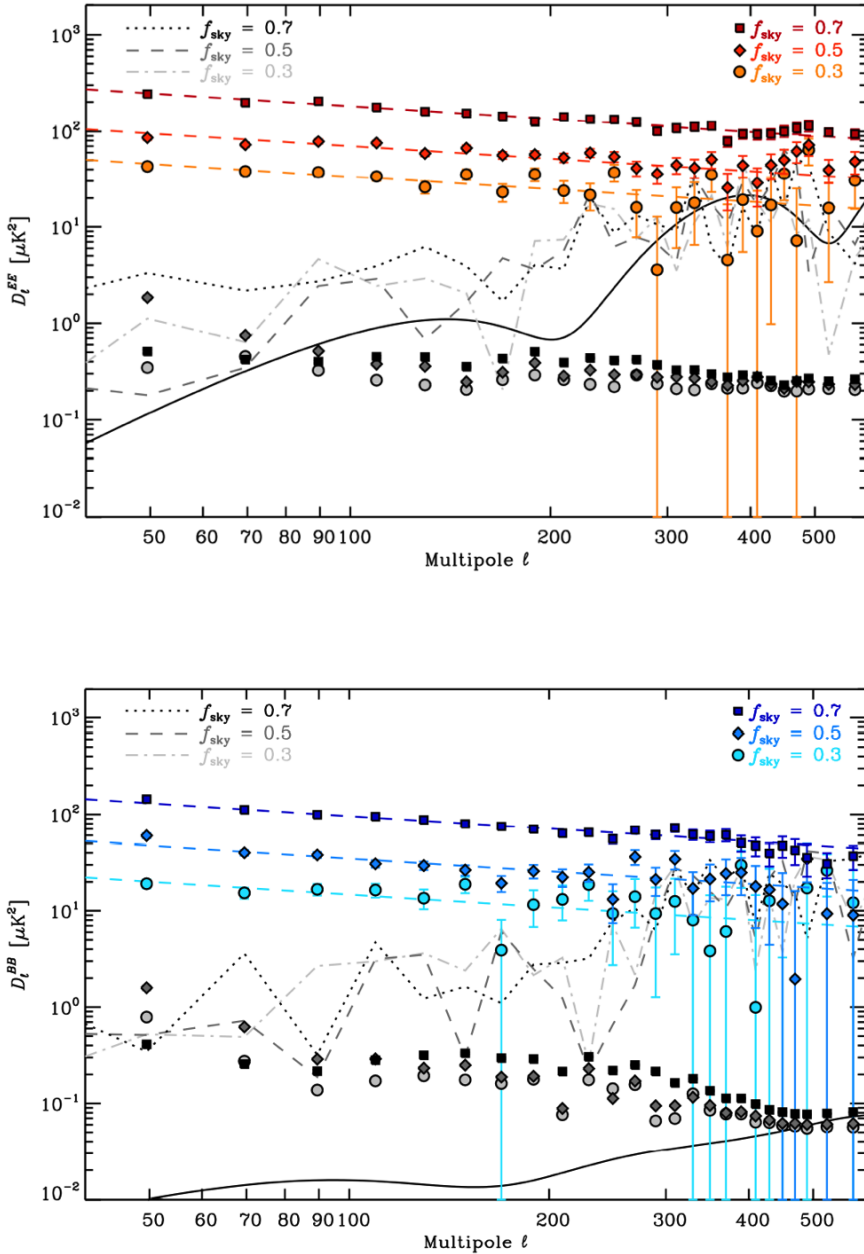
Figure 3.4: Power spectra computed from the Planck 353 GHz Stokes Q and U DS maps for both E-modes (red points, upper panel) and B-modes (blue points, lower panel) for three different regions of the sky. Grey points represent the estimation of the intensity-to-polarization leakage. Grey dotted, dashed and dotted-dashed lines are the results of the null-tests. Solid black lines represent the CMB power spectra models. For a detailed description see text. (Planck Collaboration Int. XXX 2014)

Figure (3.4) shows the obtained E-modes (upper panel) and B-modes (lower panel) angular power spectra computed on the regions with $f_{sky} = \{0.3, 0.5, 0.7\}$ (regions defined by black, purple and orange colors on figure 3.3 respectively). Colored symbols represent the actual spectra of the dust polarized emission. Grey symbols represent the expected level of intensity-to-polarization leakage, showing that this spurious signal is negligible compared to the dust emission. The dashed, dotted and dashed-dotted grey lines are the absolute values of the null-test spectra. These spectra are obtained considering again different and independent data subsets and in particular the DS maps and the HR maps (defined in section 2.1.3). The null-test spectra are computed as follows: $(353_{DS1,HR1} - 353_{DS1,HR2}) \times (353_{DS2,HR1} - 353_{DS2,HR2})$. The resulting $\mathcal{D}_\ell^{EE}$ and $\mathcal{D}_\ell^{BB}$ (we recall that $\mathcal{D}_\ell = \ell(\ell+1)C_\ell/2\pi$) spectra show a behavior that is consistent with what is expected from a white noise dominated spectrum (i.e. $\propto \ell^2$), implying that there is no evidence for any residual systematic effect.

Figure (3.4) also shows the CMB E and B-modes spectra, for comparison (black solid lines). The $\mathcal{D}_\ell^{EE}$ CMB power spectrum is computed from the Planck best-fit ΛCDM model obtained from temperature data (Planck Collaboration XVI 2014) while the $\mathcal{D}_\ell^{BB}$ represent the expected B-modes signal with $r = 0.2$ and gravitational lensing. At 353 GHz, the $\mathcal{D}_\ell^{EE}$ angular power spectrum of the dust is about 3-4 orders of magnitude larger than the CMB at $\ell = 30$, 1-2 orders of magnitude larger at $\ell = 100$, and about the same order of magnitude as the CMB at $\ell > 300$. For the $\mathcal{D}_\ell^{BB}$ at 353 GHz the dust power spectrum is much greater than the CMB model for all ℓ values.

The thermal dust power spectra for all the sky regions are fit with a power law ($C_\ell^{XX} \propto \ell^{\alpha_{XX}}$). The results of this fit, computed in the multipole range $40 < \ell < 500$, are
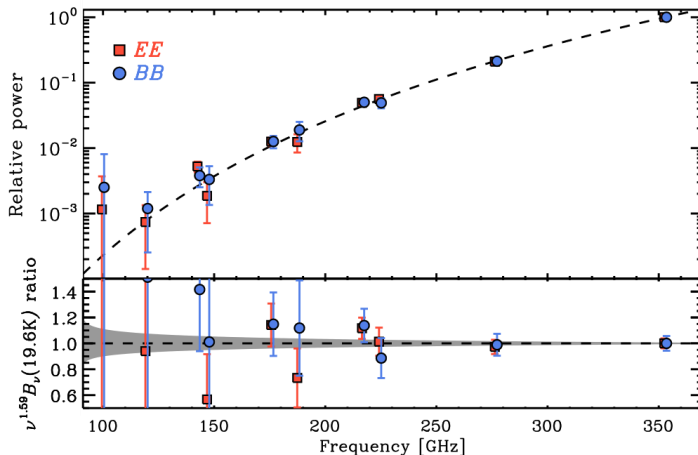
Figure 3.5: Frequency dependence of the amplitudes $A^{EE,BB}$ of the angular power spectra, relative to 353 GHz. The dashed lines represent the model emission for dust (modified blackbody with $\beta_d = 1.59$ and $T_d = 19.6$ K. The bottom panel shows the relative discrepancy with respect to this model spectrum. The $\pm 1\sigma$ uncertainty area from the expected dispersion of β_d is displayed in grey (Planck Collaboration Int. XXX 2014).

consistent with constant values of $\alpha_{EE} = -2.41 \pm 0.02$ and of $\alpha_{BB} = -2.45 \pm 0.03$.

The relative amplitude of the $\mathcal{D}_\ell^{BB}$ with respect to $\mathcal{D}_\ell^{EE}$ is also calculated and presented in the paper. It is estimated considering a single power law with a fixed spectral index of $\alpha = -2.42$ for both EE and BB spectra, and computing the ratio of the amplitude derived from this fit, A^{BB}/A^{EE}. This ratio is consistent with $A^{BB}/A^{EE} = 0.52 \pm 0.03$ for all the considered sky regions and is significantly different from unity. This result implies that the thermal dust emits almost twice the power in E-modes compared to B-modes. This behavior is not taken into account in any of the existing models of polarized microwave dust emission. Further investigations into the structure of the dust polarization sky are required to account for the observed ratio.

Planck multi-frequency data allows to study the frequency dependence of the thermal dust polarized emission. Angular auto and cross-spectra are calculated from Q and U DS maps at 100, 143, 217 and 353 GHz (for a total of ten power spectra). The E-modes power spectra are obtained after subtracting the best-fit ΛCDM model for CMB. All these spectra are consistent with a power law in ℓ, with the exponent α=-2.42 measured at 353 GHz. Therefore for each of these spectra the amplitude of the power law function with this fixed exponent has been obtained. Figure (3.5) shows the dependence of these amplitudes as a function of frequency, calculated for the sky mask with $f_{sky} = 0.3$ (results on the others mask are consistent). For cross-spectra between different frequency channels the plot reports the geometric mean frequency ($\bar{\nu} = \sqrt{\nu_1 \nu_2}$). This frequency dependence is in good agreement with the SED distribution measured for total intensity thermal dust emission, i.e a modified blackbody spectrum with $\beta_d = 1.59$ and $T_d = 19.6$ K (see section 2.1.2). The residual of the fit do not show any evidence for and excess power at 100 GHz, which might arise from polarized synchrotron emission.

3.3 Polarized foreground emission in the BICEP2 field

We now use the characteristics of the polarized dust radiation derived at high Galactic latitude to infer the level of contamination in the BICEP2 field. To study the CMB radiation, in principle, the polarization power spectra of Planck data could be computed directly in the BICEP2 field considering the frequency channels with low foreground emission (70, 100, 143 GHz). Unfortunately the Planck sensitivity, on such a small sky patch, is too low to do cosmological B-modes studies. The mean noise level on the BICEP2 patch, computed considering Q and U maps at $Nside = 128$ corresponding to a pixel dimension of about 30 arcmin, is of the order of $\sim 8.3 \,\mu\text{K}$ at 70 GHz, $\sim 1.8 \,\mu\text{K}$ at 100 GHz and $\sim 2.5 \,\mu\text{K}$ at 143 GHz, one to two orders of magnitude worst than BICEP2 ($\sim 87 \,\text{nK}$), making impossible to draw any conclusion on the BICEP2 results using independent measurements from Planck in these bands.

Although the 353 GHz channel has comparable sensitivity, using this frequency allows us to gather additional information where the Galactic emission is brighter and the signal-to-noise ratio on maps is higher. Figure (3.6) shows the Q and U maps at 353 GHz in the BICEP2 region smoothed at an angular resolution of 30 arcmin, the same as BICEP2. At this frequency the thermal dust signal is clearly visible on the maps with an RMS, calculated considering the entire region, of the order of $20 \,\mu\text{K}$ for both Q and U.

We can have a first estimate of the thermal dust signal power at the BICEP2 frequency by scaling the measured value of the RMS from 353 GHz to 150 GHz. To do this, we
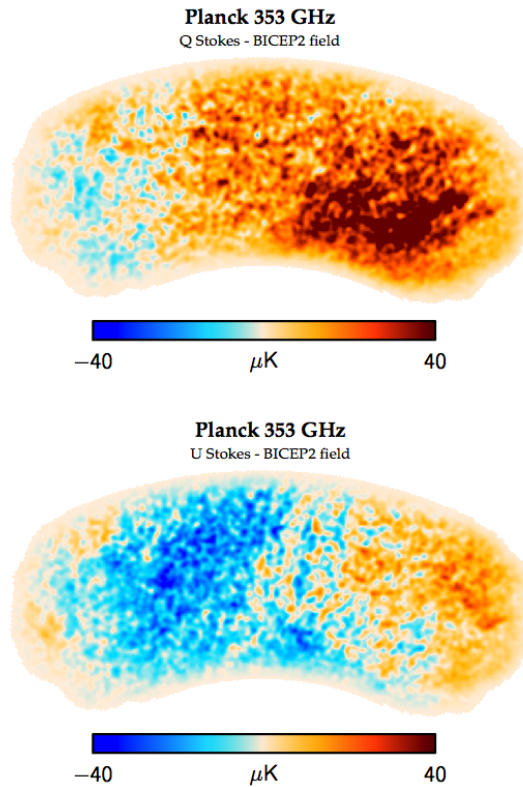
Figure 3.6: Q and U Planck maps at 353 GHz in the BICEP2 region, smoothed at an angular resolution of 30 arcmin.

consider the modified blackbody spectrum with $\beta_d = 1.59$ and $T_d = 19.6$ K, which agrees with Planck polarization data (see figure 3.5). The scaling factor, from 353 to 150 GHz, is ~ 0.04 implying that the expected RMS at 150 GHz is of the order of $0.8\,\mu$K. We recall that the BICEP2 B-modes map has a peak-to-peak signal amplitude of $\sim 0.6\,\mu$K (figure 3.1). Even though Planck and BICEP2 maps are not directly comparable, since the in the BICEP2 pipeline a filter which removes the large scale structure is applied to data, this simple qualitatively analysis tells us that the thermal dust signal in not negligible and needs to be taken into account to better understand the signal observed by BICEP2.

In order to perform a more quantitative analysis, it is necessary to compute the angular power spectrum of the Planck 353 GHz signal, as it is described in the next sections.

3.3.1   Power spectrum estimators

Computing angular power spectra from maps with an incomplete sky coverage required the application of specific tools. For temperature-only spectra the cutting of the sky sphere implies a coupling between different modes. For polarization, as sky cut introduces new modes that arise from mixing together a fraction of the E and B-modes (see for example Bunn et al. 2003). These ambiguous modes are not negligible, in particular when the E-modes signal is much stronger than the B-modes one, as for the CMB case.

If we call $\tilde{C}_\ell$ the pseudo-C_ℓ obtained by computing power spectra directly on the sky patch, we have:

$$\begin{pmatrix} \tilde{C}_\ell^{TT} \\ \tilde{C}_\ell^{EE} \\ \tilde{C}_\ell^{BB} \end{pmatrix} = \begin{pmatrix} \mathcal{M}_{\ell\ell'}^{TT,TT} & & \\ & \mathcal{M}_{\ell\ell'}^{EE,EE} & \mathcal{M}_{\ell\ell'}^{EE,BB} \\ & \mathcal{M}_{\ell\ell'}^{BB,EE} & \mathcal{M}_{\ell\ell'}^{BB,BB} \end{pmatrix} \begin{pmatrix} C_\ell^{TT} \\ C_\ell^{EE} \\ C_\ell^{BB} \end{pmatrix} \tag{3.1}$$

where, for simplicity, we have considered only the temperature and polarization E-modes and B-modes spectra. The C_ℓ^{XX} represent the pure-C_ℓ we want to measure and the $\mathcal{M}_{\ell,\ell'}^{XX,YY}$ describes the mode-mode coupling resulting from the sky cut. This kernel depends only on the geometry of the sky cut and can be expressed in terms of the power spectrum of the applied mask (see Hivon et al. 2002).

The BICEP2 telescope observed a small region of about 1% of the sky. To compute the power spectra of the Planck data in this region we need to apply an algorithm to calculate the $\mathcal{M}_{\ell,\ell'}^{XX,YY}$ kernel of the mask and recover the pure-C_ℓ spectrum. In our analysis we used two different codes to do this:

- **CrossSpect**[1]**:** this code implements the MASTER (Monte Carlo Apodized Spherical Transform Estimator) algorithm described in Hivon et al. (2002) generalized for the polarization analysis. It computes the $\mathcal{M}_{\ell,\ell'}$ matrix of equation (3.1) inverting it to recover the pure-C_ℓ.

- **Xpure:** this algorithm represents a numerical implementation of the pure pseudo-spectral approach described and validated in Grain et al. (2009). The method is optimized for computing CMB B-modes power spectra over small sky patches. It uses a suitably chosen sky apodization that vanishes (along with its first derivative) at the edges of the patch, in order to minimize the effects of E-to-B leakage due to the presence of the ambiguous modes.

Before applying these two algorithms to the data we validated them on simulations considering both the CMB and the thermal dust cases. For the CMB case we generated one hundred simulated sky maps using the *synfast* code which creates HEALPix maps (Górski et al. 2005), computed as realizations of random gaussian fields on a sphere, characterized by the user provided theoretical power spectra. In our case, the theoretical power spectrum is a standard CMB ΛCDM spectrum including gravitational waves B-modes signal with $r = 0.2$. The maps are created considering a gaussian beam of 30 arcmin and at $Nside = 512$. Then we computed the E and B-modes spectra of the one hundred Q and U maps with *CrossSpect* and *Xpure* on a sky cut corresponding to the region observed by BICEP2 (details on how we computed the mask corresponding to the BICEP2 field are reported in the next section).

We applied the same procedure for the thermal dust case, even though the approximation of random and stationary gaussian field can be applied only partially to a dust polarization map. The theoretical input power spectrum chosen for dust is the one observed in the Planck data described in section (3.2) with C_ℓ^{EE} and C_ℓ^{BB} proportional to $\ell^{-2.42}$ and the B/E power asymmetry with $C_\ell^{BB} = 0.53 C_\ell^{EE}$.

---

[1]The code has been implemented by Dr. Simona Donzelli of the University of Milan and has been fully validated and tested on the CMB data used for the Planck 2013 results papers.

Figure (3.7) shows the results of this validation on simulated maps for both CMB and dust maps. Green points are the mean of the one hundred B-modes power spectra recovered with *CrossSpect*, while the error bars are are the standard deviations. Orange points refers to the same spectra computed with *Xpure*. Dashed and dotted lines represent the theoretical input power spectra for CMB and dust, respectively, associated with the sample variance displayed as a grey shaded area and calculated as (Hivon et al. 2002):

$$\Delta C_\ell = \sqrt{\frac{2}{(2\ell+1)f_{sky}\Delta b}} C_\ell, \qquad (3.2)$$

where f_{sky} is the sky fraction of the considered region ($\sim 1.7\%$ of the sky for BICEP2 patch) and Δb is the width of the chosen multipole binning.

Both estimators are able to correct for the coupling between modes and to reconstruct the input B-modes power spectrum. *CrossSpect* estimation appears to be biased in the first and last multipole bin and the dispersion is larger than in the *Xpure* case, where error bars are compatible with what expected from the sample variance for both CMB and dust.

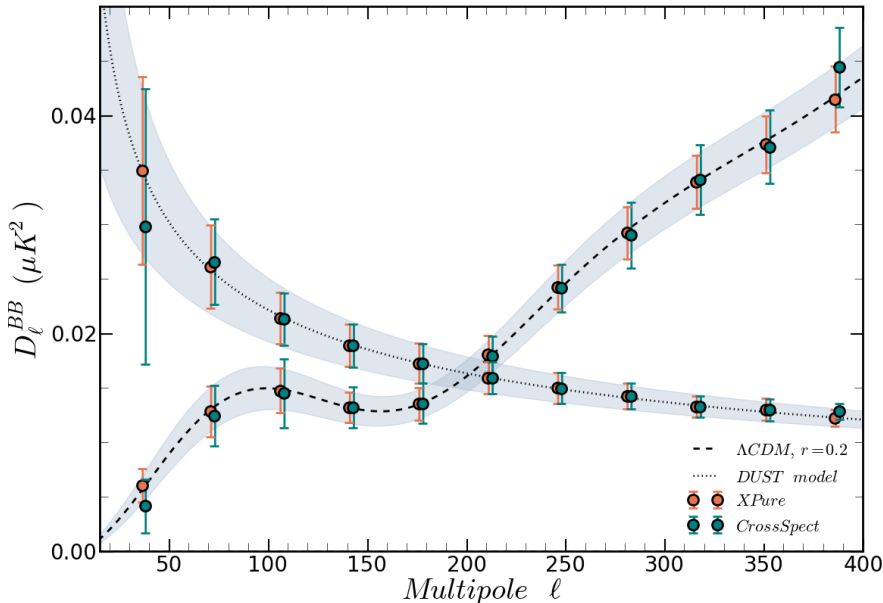**Figure 3.7:** Validation of the power spectrum estimators from simulations. Points in orange are computed with the $Xpure$ code, while green points are from $CrossSpect$. The dashed black line represent the input power spectrum model for CMB B-modes with $r = 0.2$. Dotted black line is the model for the dust spectrum with $D_\ell \propto \ell^{-0.42}$. Grey areas represent the sample variance calculated with equation (3.2).

3.3.2   Planck power spectra in the BICEP2 field

Once we have validated the performance of the power spectrum estimators in the BICEP2 field on simulated maps, we can compute the power spectra of the Planck data in the various frequency channels.

Power spectra are computed on an approximation of the BICEP2 observed region, which is the one we have chosen for the analysis reported in the PIPXXX paper. This mask has been constructed in the following way: (i) we constructed a mask M_0 by filling the inside of the BICEP2 deep-field outline[2] with 1 and 0 outside; (ii) we took the complement of this mask $M' = 1 - M_0$; (iii) we used the HEALPix *iprocess_mask* procedure to compute the angular distance of each pixel from the border of this mask; (iv) we computed the 7.5° FWHM (Full Width Half Maximum) Gaussian weight of this distance map to obtain M''; (v) we took the complement of M'' to be our definition of the BICEP2 field ($M_{B2} = 1 - M''$). The resulting field has an $f_{sky} = 0.017$ ($689 \deg^2$) which is larger than the BICEP2 $373 \deg^2$ deep-field region but is similar to the BICEP2 inverse noise variance map presented in the BICEP2 collaboration paper, even if it extends further in declination but less in right ascension. Nevertheless, in section (3.3.4) we show that the conclusions of our work do not depend significantly on the definition of this field.

Figure (3.8) shows the B-modes power spectra calculated from Planck data in the previously defined BICEP2 field for all the seven frequencies sensible to polarization (from 30 GHz to 353 GHz). We computed cross-spectra (to avoid noise bias) with the *Xpure* algorithm. For the HFI frequencies (shown in red) the cross-spectra are from the independent DS maps, for the LFI frequencies (shown in light blue) we cross-correlated the HR maps. The error bars are estimated from noise simulations. At each frequency we generated one hundred random realizations of white noise for each independent DS or HR map starting from the QQ and UU covariance matrices. We then cross-correlated these noise maps to get one hundred different cross-spectra and computed the error bars by calculating the standard deviation of these spectra. All the recovered BB spectra appear to be compatible with zero, with the only exception of the 353 GHz one.

At 353 GHz the power spectrum shows the detection of a signal at large angular scales, in the first four bins with $\ell < 150$. Table (3.1) reports the signal-to-noise ratio for each of these bins. A positive detection at 353 GHz in the power spectrum confirms the presence of dust emission in the BICEP2 field, as it was already pointed out by looking at the Q and U maps, and permits to a make more quantitative prediction on its impact on the BICEP2 results.

To be able to directly compare the signal at 353 GHz with that measured by the BICEP2 telescope, we need to rescale the dust emission at 150 GHz. We have already seen that on large portions of the sky the polarized dust emission scales as a modified blackbody. We want now to evaluate whether this assumption is valid also for the BICEP2 field. Similarly to what has been done in the PIPXXX paper on large sky regions of the sky to get figure (3.5), we compute the ten possible cross-spectra from the Planck maps from 353 GHz to 100 GHz in the BICEP2 field (353×353, 353×217, 353×143, 217×217, 353×100, 217×143, 217×100, 143×143, 143×100, 100×100). We defined a specific multipole binning, to optimize the signal-to-noise ratio, choosing three ℓ-bins defined by the intervals between multipoles 40, 120, 250, and 400. We fit each of these B-modes spectra

---

[2]This outline encloses the effective $373 \deg^2$ of deep integration
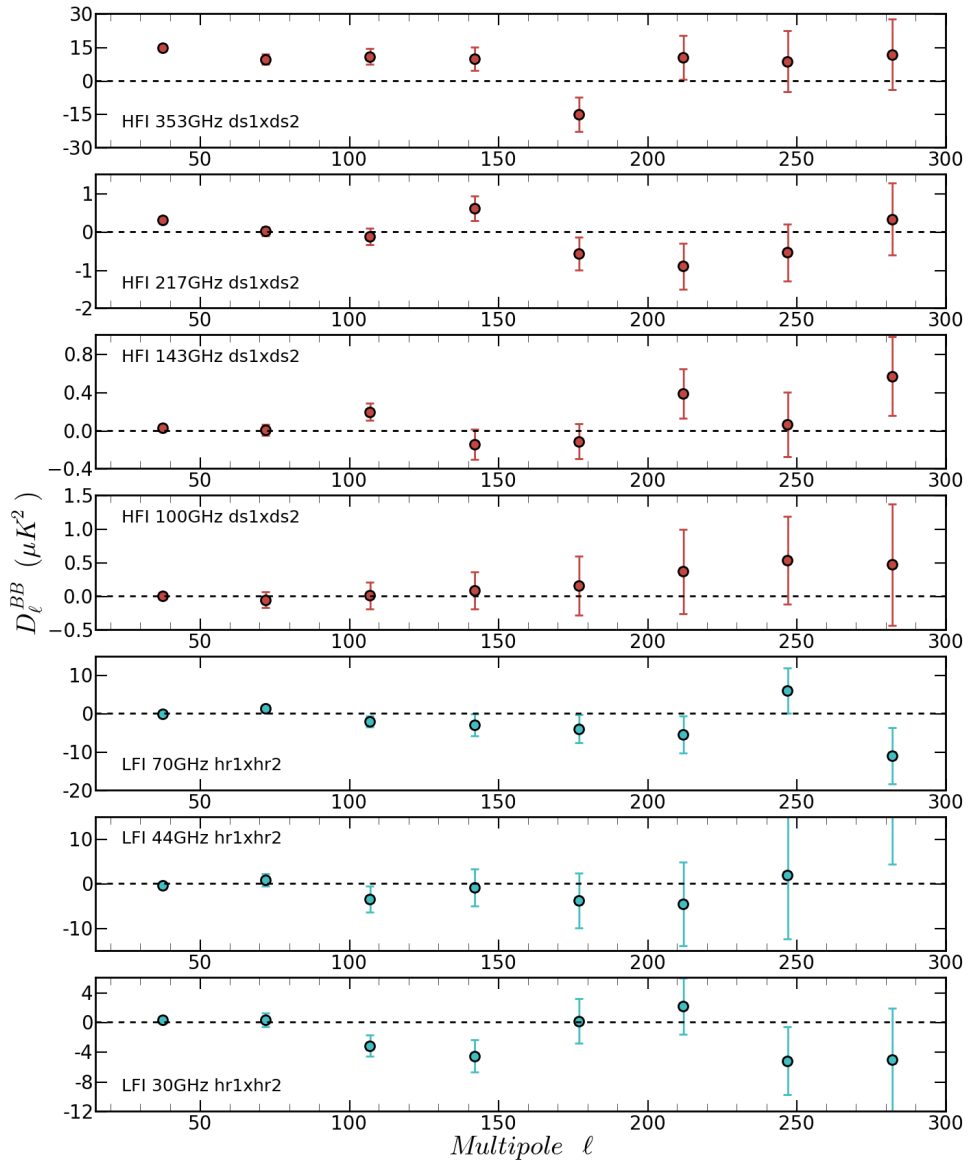
Figure 3.8: B-modes angular power spectra computed on the BICEP2 field of the Planck maps at all the seven frequencies sensible to polarization. HFI spectra are shown in red, LFI spectra in light blue color.

Multipoles	S/N
$21 < \ell < 55$	17.6
$56 < \ell < 90$	9.5
$91 < \ell < 125$	3.1
$126 < \ell < 160$	1.8

Table 3.1: Signal-to-noise ratio for the 353 GHz Planck power spectrum in BICEP2 region (upper panel in figure 3.8) for the first four multiple bins.
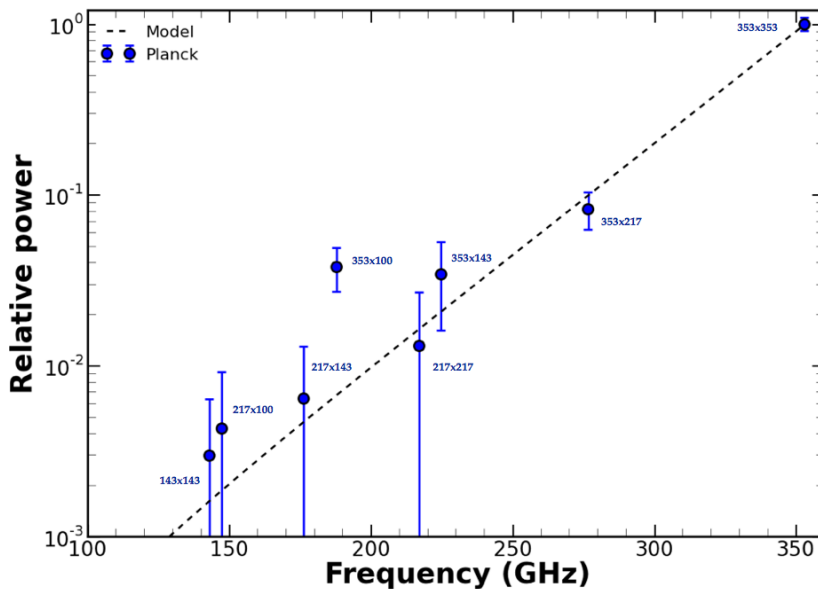

Figure 3.9: Frequency dependence of the amplitude A^{BB} of the angular power spectrum $\mathcal{D}_\ell^{BB}$ computed on BICEP2 field normalized to the 353 GHz amplitude (blue points); amplitudes for cross-power spectra are plotted at the geometric mean frequency. Dashed black line represents the modified blackbody model for dust emission with $\beta_d = 1.59$ and $T_d = 19$ K.

with the expected power law dependence for thermal dust emission ($C_\ell = A^{BB} \times \ell^{-2.42}$) and recover the value of the amplitude A^{BB}. Figure (3.9) shows these amplitudes as a function of the effective frequency. Data for frequencies below 143 GHz are not plotted because they are noise dominated. We compare the relative power of the amplitudes with the expected behavior for thermal dust (modified blackbody with $\beta_d = 1.59$ and $T_d = 19$ K, black dashed line) finding a good agreement between model and data. This result justifies the use of the modified blackbody model to extrapolate the power of the dust emission detected at 353 GHz to 150 GHz.

3.3.3   Impact of foreground on BICEP2 results

We now rescale the B-modes Planck measurements of the polarized thermal dust signal from 353 to 150 GHz, to compare it directly with the BICEP2 observations. This is shown in figure (3.10), where the red boxes are centered on the values of the Planck power spectrum, in the first four multipole bins of table (3.1), extrapolated to 150 GHz and their vertical width is the $\pm 1\sigma$ uncertainty obtained from noise simulations. Black points are the BICEP2 bandpowers with error bars that include both the statistical uncertainties and the sample variance of the B-modes CMB signal with $r = 0.2$ (BICEP2 collaboration I 2014). In the three multipole bins at $\ell \sim 75, 110, 145$ the Planck estimate of the dust contribution is in very good agreement with the signal observed by BICEP2 with discrepancies between 0.1 and 0.3σ. In the first bin at $\ell \sim 40$ the Planck estimate of $\mathcal{D}_\ell^{BB}$ lies a factor ~ 2.5 above that of BICEP2. The behavior of the Planck power spectrum is, as already described, the one expected for a dust signal with $\mathcal{D}_\ell^{BB} \propto \ell^{-0.42}$. Various effects may be responsible for this discrepancy and are discussed in the next section.

The result of this comparison clearly shows that thermal dust emission is not negligible in the BICEP2 patch of the sky at 150 GHz and must be taken into account to draw any conclusion about the physical origin of the detected signal. Nevertheless, as pointed out, the Planck sensitivity on such small region of the sky is not optimal, leading

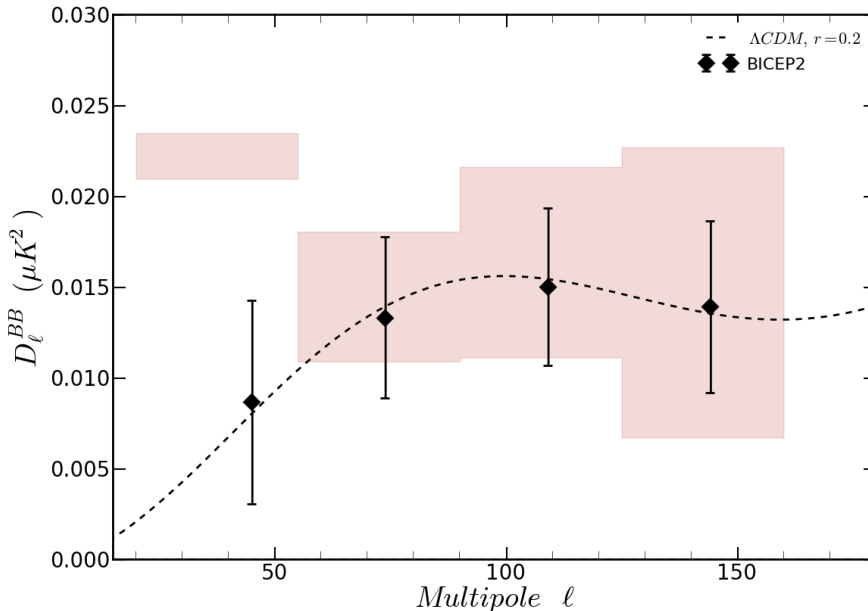**Figure 3.10:** Planck B-modes power spectrum at 353 GHz extrapolated to 150 GHz and compared to BICEP2 measurements. Red boxes are centered on the value of the Planck power spectrum estimate, the vertical width of the boxes is the $\pm 1\sigma$ statistical uncertainty. Black points are the BICEP2 bandpowers from BICEP2 collaboration I (2014). Dashed black line is the ΛCDM CMB model with $r = 0.2$.

to uncertainties of the order of 25% ($\ell \sim 75$), 30% ($\ell \sim 110$) and 55% ($\ell \sim 145$). These large uncertainties leave open the possibility of the existence of a residual cosmological gravitational waves signal with $r < 0.2$ in the BICEP2 data after the removal of the dust contribution. The best way to understand whether this is the case or not is to put together BICEP2 and Planck data and to cross-correlate them. The results of this joint analysis are presented in section (3.4).

We also estimate the contribution of the polarized synchrotron emission to the BICEP2 spectrum. The Planck B-modes power spectrum at 30 GHz, the lowest of the Planck frequency where the synchrotron emission is dominant, does not show any positive detection of signal in BICEP2 region implying that data are dominated by instrumental noise. Nevertheless, we can extrapolate the B-modes power spectrum at 30 GHz, shown in figure (3.8), to 150 GHz and use it to put an upper limit on the amplitude of the synchrotron emission at this frequency. Fuskeland et al. (2014), analyzing the WMAP 9 years K and Ka maps, found a mean spectral index of $\beta_s = -3.12 \pm 0.04$ for the power law frequency dependence of synchrotron emission at high Galactic latitude. Using this value to rescale the Planck power spectrum and considering a 3σ upper limit, we found that the maximum synchrotron contribution to the BICEP2 B-modes spectrum is of about 1.9% at $\ell \sim 40$ and about 1.3% at $\ell \sim 75$. This result implies that the synchrotron contribution to the BICEP2 observation is negligible.

3.3.4 Possible sources of systematic effects

In this section we discuss possible systematic effects that may impact the Planck measurement of polarized dust.

First of all, we checked whether the Planck power spectrum at 353 GHz in the BICEP2 region depends on the estimator algorithm. Figure (3.11) shows a comparison of the power spectra obtained with the two algorithm described in section (3.3.1). Red boxes represent the estimation of *Xpure* and are just the same as in figure (3.10), blue boxes have been obtained in the same way described previously (from 353 GHz DS1×DS2 cross-correlation extrapolated to 150 GHz) using *CrossSpect*. The width of the boxes represents the statistical uncertainty obtained from the Monte Carlo noise simulations computed from the QQ and UU noise covariance matrices of the input maps. Points are the mean value of the estimated power spectra, while error bars are calculated from the simulations described in section (3.3.1) used to validate the algorithms. In practice, they represent an estimate of the error that the algorithms may perform in recovering the power spectrum (including also the sample variance). The two estimators give compatible results in the last three multipole bins, for both the mean value and the statistical uncertainties, with discrepancies below 2% in the central value. On the contrary, in the first bin *CrossSpect* gives about half the power of the *Xpure* estimate even though the two results are marginally compatible within the uncertainties. Nevertheless, in both cases the Planck first bin of the power spectrum of thermal dust lies above the ΛCDM CMB model with $r = 0.2$, confirming our conclusion that the foreground emission is not negligible in the BICEP2 field at 150 GHz.

As second test to check for residual systematic effects we computed null-tests on the different and independent sets of full sky maps available from Planck observations at 353 GHz. In particular, we calculated the cross-spectra on BICEP2 region between the
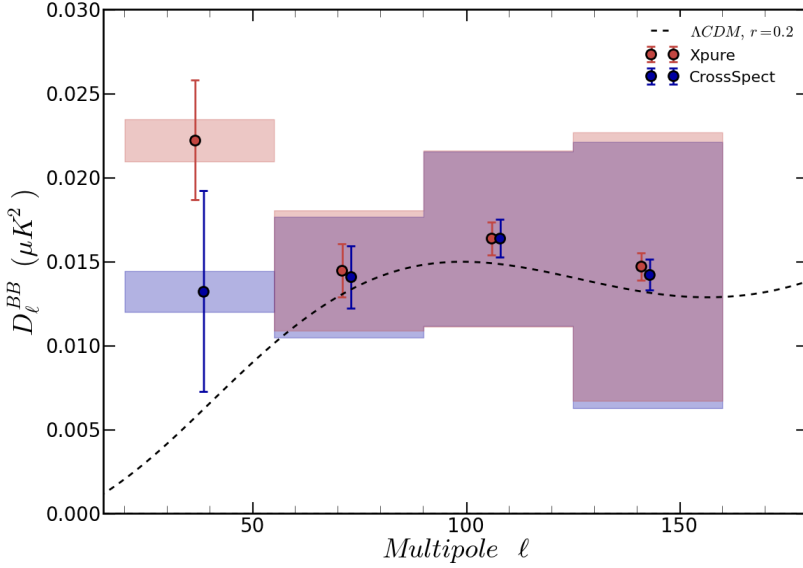
Figure 3.11: Comparison between the estimations of Planck power spectra at 353 GHz extrapolated to 150 GHz in BICEP2 field obtained with *Xpure* (red) and *CrossSpect*. The vertical width of the boxes represents the $\pm 1\sigma$ statistical uncertainty on the measurements, error bars are an evaluation of the bias that the power spectrum estimators might have. The black dashed line is the ΛCDM CMB model with $r = 0.2$.

usual DS maps, the HR maps (see section 3.2), and the two independent maps obtained from the first and the second year of observation of the Planck satellite (YR maps). The differences among these spectra are shown in figure (3.12) together with their statistical uncertainties from noise simulations. As expected, They are all compatible with zero within 2σ, showing thus no evidence of any residual systematic effect that might compromise our results.

Finally we checked whether the Planck power spectrum depends on the extent and specification of our approximation of the BICEP2 field. In order to do this we construct a set of nested masks, starting from the BICEP2 deep field binary mask (previously named M_0). We increase the size of M_0 by exactly $1°$ in every direction (performing a smoothing and a cutting) to get a binary mask M_1 and from it we proceed in the same way up to M_5 which, therefore, is $5°$ larger than M_0 in every direction. This set of masks is shown in the upper right side of figure (3.13). We apodized each of these masks with *Xpure* considering a radius of apodization of $4°$ and then computed the Planck 353 GHz power spectrum rescaling it to 150 GHz in the usual way. We calculated the difference between the BB power spectrum in the previously defined BICEP2 field (named M_{B2}) and the spectra in each of these new masks. These differences are plotted in figure (3.13). With the only exception of the first bin, they are compatible with zero, implying that our estimation of the polarized dust signal does not depend on the detailed specification of the field we choose. The power in the first bin, on the contrary, is sensible to the
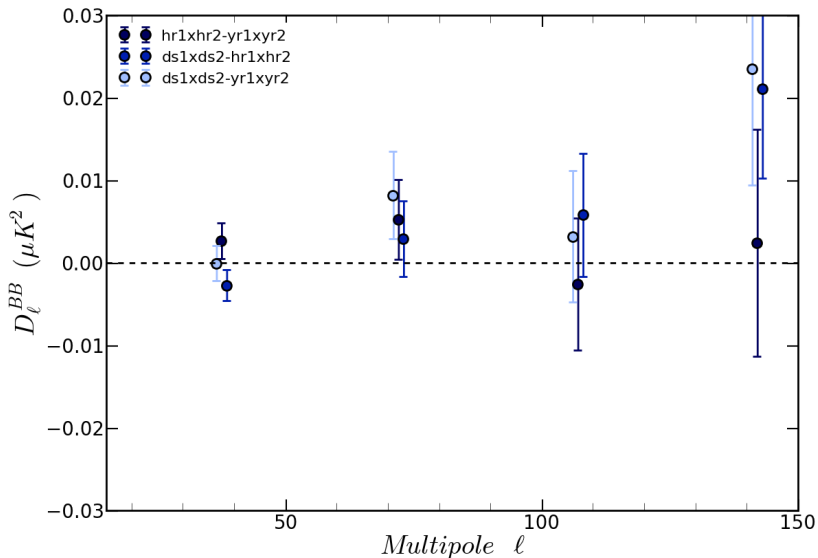
Figure 3.12: Null-test power spectra computed from 353 GHz Planck maps on BICEP2 region and rescaled to 150 GHz. The spectra are calculated with the *Xpure* algorithm.

Figure 3.13: Planck 353 GHz BB angular power spectrum differences extrapolated to 150GHz, determined from the spectra computed on the M_{1-5} regions (presented in the text and shown in the upper right panel) and the spectrum computed on BICEP2 field (M_{B2}). The spectra are calculated with *Xpure*.

definition of the field, with discrepancy between M_0 and M_5 of the order of 10σ. We have already seen that in this bin the error from the power spectrum estimation may be large and moreov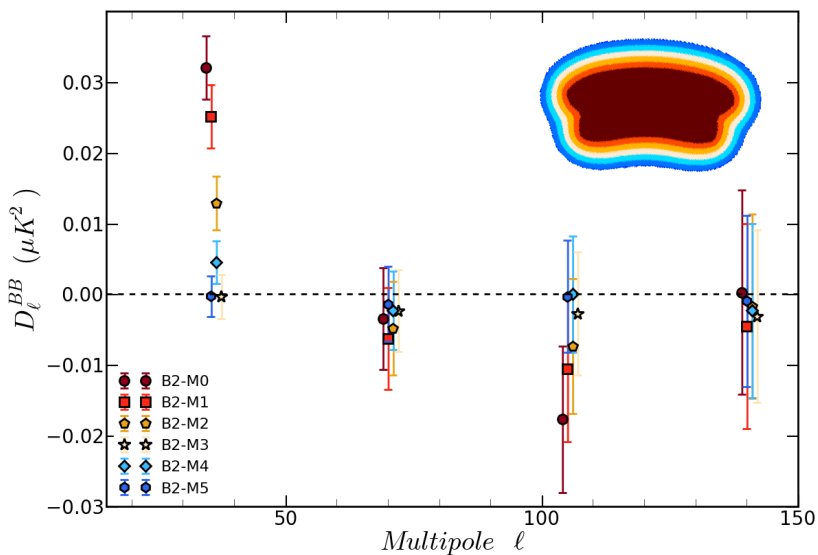er shrinking the mask results in a lack of power in the large angular scale modes. In any case, as we noticed previously, the uncertainty on the power of this bin does not change our conclusion about the strong level of contamination from thermal dust emission in the BICEP2 data.

3.4   Planck and BICEP2/Keck joint analysis

We have seen that the analysis of Planck data at 353 GHz reveals a strong contamination by the presence of polarized thermal dust radiation in the BICEP2 field. The Planck B-modes power spectrum computed in this patch of the sky showed a level of foreground emission at 353 GHz sufficient to explain the 150 GHz excess observed by BICEP2 (figure 3.10). Nevertheless, the non optimal sensitivity of the Planck detectors on such a small region of the sky leads to large uncertainties on the Planck spectrum, so that the presence of a residual primordial tensor signal in the BICEP2 data, after the removal of the dust contribution, can not be ruled out.

To better understand this situation the Planck and BICEP2 collaborations jointed their efforts performing a combined analysis of the data coming from the two telescopes. This joint analysis is reported on a paper published in March 2015 on the *Physical review letters* journal with the title "A Joint Analysis of BICEP2/Keck Array and Planck Data" (BICEP2/Keck Array and Planck Collaborations 2015, hereafter B2KP). My specific contribution to this analysis was focused on understanding the impact of the filter applied to data on the power spectra. In the next sections the main and general results of this joint analysis are summarized.

3.4.1   Data preparation

In the B2KP paper data from the Planck satellite, the BICEP2 telescope and the Keck Array telescope are cross-correlated with the primary goal to obtain a constraint on the tensor-to-scalar ratio r after having taken into account the thermal dust contribution.

The Keck Array is a system of BICEP2-like receivers also located at the South Pole. During the 2012 and 2013 season, the Keck Array observed the same field in the sky as BICEP2 in the same single frequency band centered at 150 GHz. Combining the BICEP2 and Keck Array observations yields to Q and U maps with noise RMS of the order of 57 nK, considering pixel dimension of $1°$, which represents the highest sensitivity ever reached in CMB observations.

Keck Array data showed again an excess in the B-modes power spectrum over the lensed-ΛCDM expectation with statistical significance $\gtrsim 5\sigma$ in the range $30 < \ell < 150$, compatible with a primordial tensor signal with $r = 0.2$ in agreement with BICEP2 measurements, confirming that this signal is not due to residual systematic effects (BICEP2 and Keck Array collaboration V 2015).

Since Planck and BICEP2/Keck data are coming for extremely different instruments and are processed through different pipelines, some data preparation was needed before cross-correlating the data. In particular BICEP2/Keck maps are filtered such that large angular scales are suppressed anisotropically to avoid atmospheric and ground-fixed

contamination. For these reasons, and in order to facilitate the comparison, we prepared "Planck as seen by BICEP2/Keck" maps. Planck maps were masked considering the actual BICEP2/Keck field, then were smoothed with the BICEP2/Keck beam profile, assuming azimuthal symmetry for the beam. Moreover, the T, Q and U maps were rotated from Galactic (the standard Planck coordinate system) to celestial coordinates. Finnaly, the obtained maps, were passed through and "observing" matrix which applied the BICEP2/Keck filter.

Figure (3.14) shows the Planck Q and U maps at 353 GHz after having applied to them the BICEP2/Keck reobservation process. By comparing these maps with the original Planck maps reported in figure (3.6) we can clearly see the effect of the filtering which totally removes the large angular scale structures along the BICEP2/Keck scanning direction, suppressing the thermal dust signal. The RMS on these filtered Planck maps is of the order of $10\,\mu K$ for both Q and U, about a half of the RMS on the original Planck maps (see section 3.3).

In figure (3.15) the effect of the filtering is shown on power spectra. To compute these spectra we used gaussian dust simulations as described in section (3.3.1), with the usual input model for thermal dust emission with $\mathcal{D}_\ell^{BB} \propto \ell^{-0.42}$. We first computed the power spectrum of the one hundred simulated thermal dust maps, with *Xpure*, to
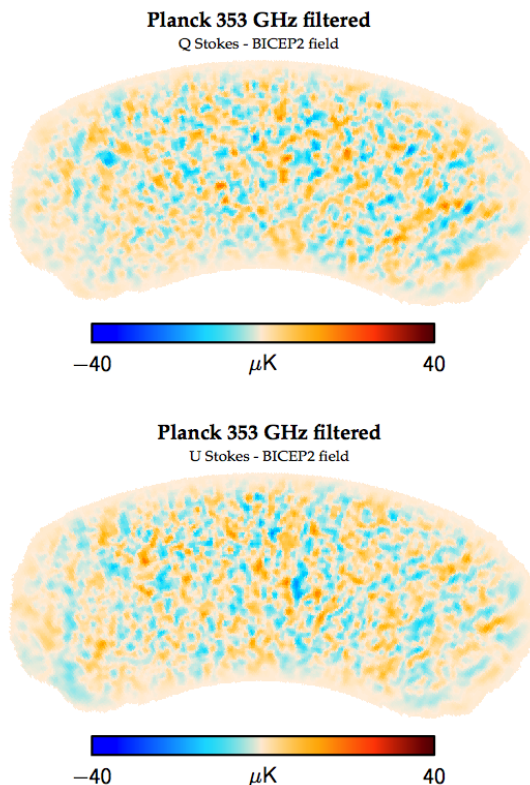

Figure 3.14: Q and U Planck maps at 353 GHz in the BICEP2 region of the sky after the BICEP2/Keck reobservation process which applies the filtering.

get the orange points on the plot. We the processed the simulated maps through the BICEP2/Keck reobservation procedure and estimated again the power spectra on the resulting maps (purple points). Error bars are calculated from the standard deviation of the one hundred spectra computed for the two cases. The difference between the input spectrum and the reobserved spectrum represents the effect of the filtering which suppress the power of the $\mathcal{D}_\ell^{BB}$ at all the angular scales, but more drastically at low multipoles.
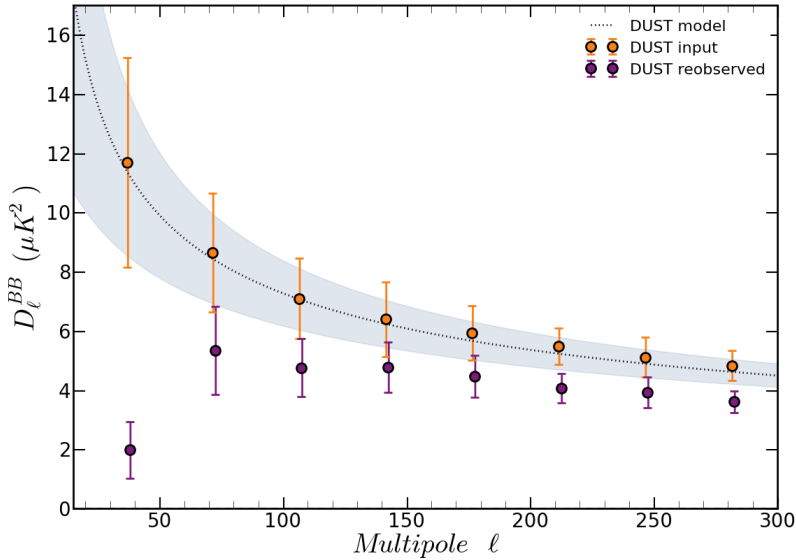

Figure 3.15: Effect of the BICEP2/Keck filtering on power spectra obtained from simulated thermal dust map. The dotted line is the input dust model with $\mathcal{D}_\ell^{BB} \propto \ell^{-0.42}$, the grey area represents the sample variance computed from equation (3.2). Orange points are the estimation of the B-modes power spectrum from the input simulated maps, purple points are obtained after having applied the reobservation procedure to these input maps.

3.4.2 Planck and BICEP2/Keck cross-spectra

Once the reobservation process is applied to the Planck polarization maps, we can compute cross-spectra between the BICEP2/Keck maps at 150 GHz and each of the Planck maps at the seven polarized Planck frequencies. Figure (3.16) shows the resulting B-modes cross-spectra in the multiple range $20 \lesssim \ell \lesssim 300$. These spectra are corrected for the effect of the filter described previously and error bars are computed from the standard deviation of noise simulations. The BK150×P353 BB spectrum shows an highly significant detection of a signal in the first four multipole bins, with signal-to-noise ranging from 1.7 to 6.2 (see table 3.2). Additionally, there is an evidence for excess also in the BK150×P217 spectrum. There is also a weak indication of excess in the BK150×P70 spectrum, but none in the BK150×P30 as would be expected in the case of synchrotron contamination in the BICEP2/Keck measurement, since synchrotron emission is stronger at
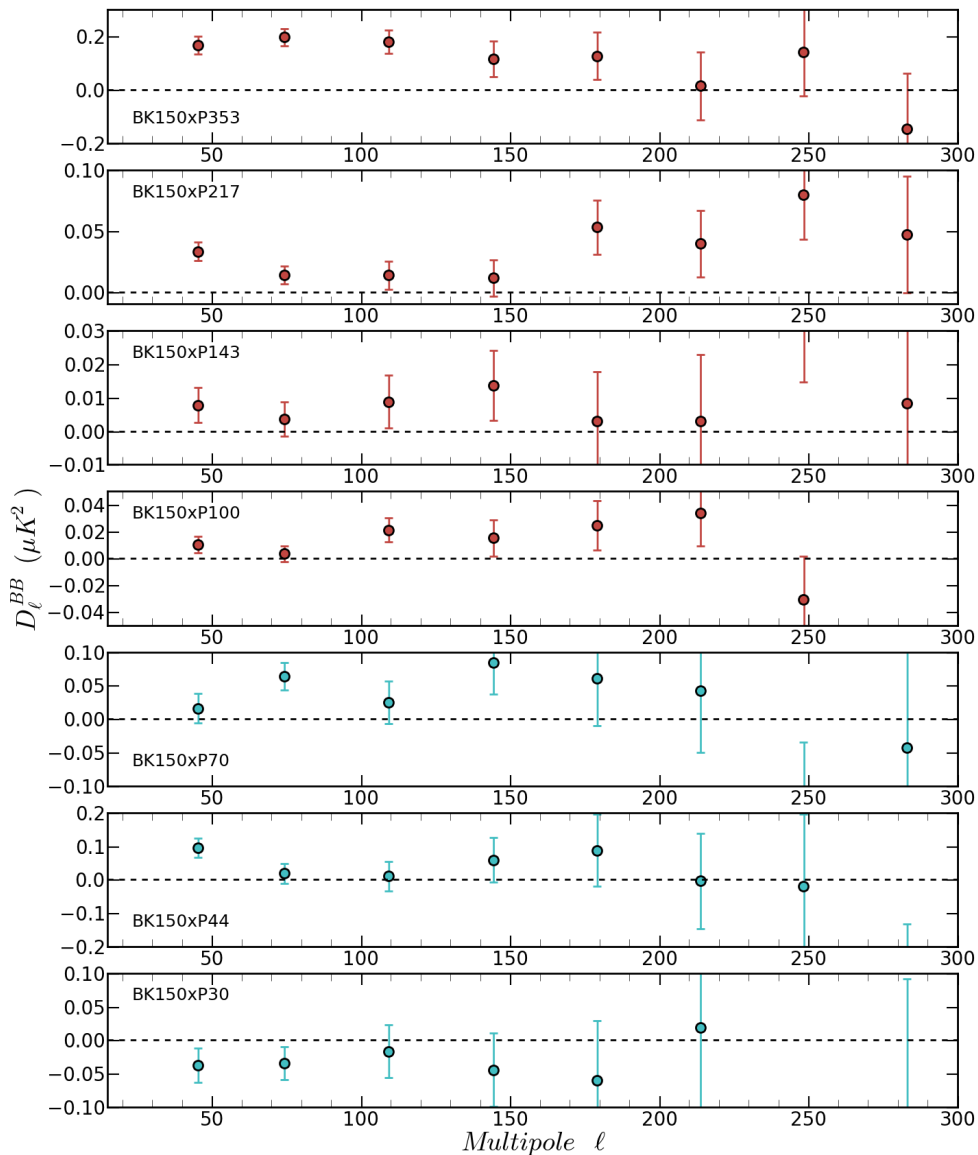
Figure 3.16: B-modes cross power spectra between the BICEP2/Keck combined map at 150 GHz and the HFI (red points) and LFI (light blue points) Planck maps on BICEP2 field (adapted from BICEP2/Keck Array and Planck Collaborations 2015).

Multipoles	S/N
$21 < \ell < 55$	5.0
$56 < \ell < 90$	6.2
$91 < \ell < 125$	4.1
$126 < \ell < 160$	1.7

Table 3.2: Signal-to-noise ratio for the BK150×P353 B-modes power spectrum (upper panel in figure 3.16) for the first four multiple bins.

30 GHz than at 70 GHz, meaning that presumably the signal in BK150×P70 is due to noise fluctuations.

The presence of a positive correlation between BICEP2/Keck and Planck data at 353 GHz in the B-modes power spectrum strongly supports the fact that BICEP2/Keck data at 150 GHz are contaminated by thermal dust emission, as was already indicated by the analysis of the Planck data alone reported in the previous sections.

An optimal way to remove the foreground contribution from BICEP2/Keck maps would obviously be to apply a component separation algorithm as described in section (2.1.4) using the Planck high frequency data (at 353 and 217 GHz) as foreground monitor in order to isolate the CMB radiation and eventually reveal the presence of residual primordial gravitational waves signal. Nevertheless the poor signal-to-noise ratio of Planck maps in this sky region and the additional filtering applied to the BICEP2/Keck
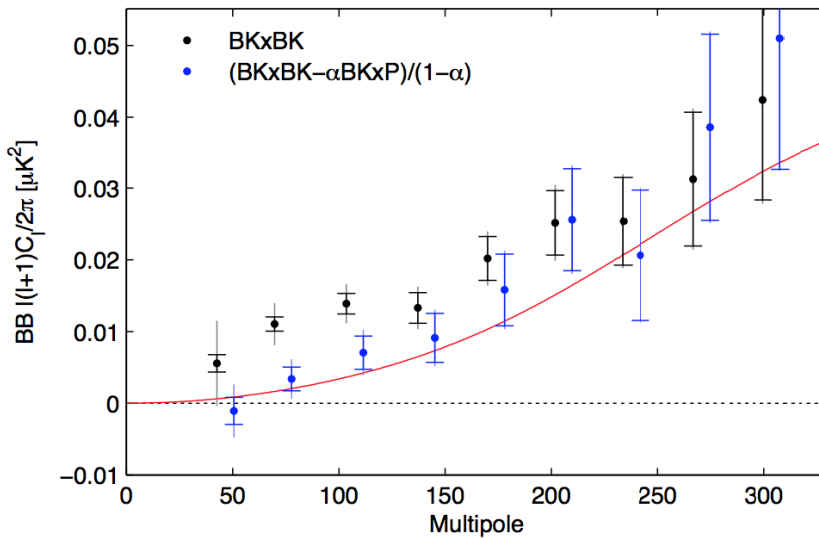

Figure 3.17: B-modes spectrum of the BICEP2/Keck maps before and after subtraction of the dust contribution, estimated from the cross-spectrum with Planck 353 GHz (BICEP2/Keck Array and Planck Collaborations 2015).

data prevent from using this kind of methods. We can anyway make an estimate of the B-modes signal of the CMB radiation, cleaned out from the thermal dust contribution, by calculating the following cross power spectrum: (BK×BK-αBK×P353)/(1-α), where the α coefficient represent the scaling factor of the thermal dust from 353 GHz to 150 GHz. Considering the usual modified blackbody spectrum for the dust frequency dependence, as described in section (3.2), we have $\alpha \simeq 0.04$. The result of this calculation is shown in figure (3.17) in blue and is compared with the original BICEP2/Keck auto-spectrum (black points). The cleaned spectrum is compatible with a lensed-ΛCDM model with $r = 0$ (red solid line).

3.4.3 Constraint on r

Bayesian statistics can be used to constrain the tensor-to-scalar ratio taking into account the presence of the thermal dust radiation in the data. The B2KP paper reports the results of this analysis in section III and here, for completeness, we summarized the main ones, even though I was not directly involved in this specific part of the analysis.

To sample the parameter space a joint likelihood function has been constructed considering the BICEP2/Keck and Planck bandpower values of the auto and cross-spectra. The used fiducial model took into account a standard lensed-ΛCDM paradigm with tensor modes with amplitude r, plus thermal dust with amplitude A_d (specified at 353 GHz and $\ell = 80$). The model has been fit to B-modes bandpowers of the BICEP2/Keck and Planck auto and cross-spectra at 353 and 217 GHz considering the first five multipole bins with $20 < \ell < 200$. For the Planck single frequency case the cross-spectrum DS1×DS2 has been used. The dust is modeled as the usual power law $\mathcal{D}_\ell^{BB} \propto \ell^{-0.42}$, with free amplitude A_d and frequency scaling according to a modified blackbody (with fixed $T_d = 19\,\text{K}$, and gaussian prior on the spectral index $\beta_d = 1.49 \pm 0.11$).

Figure (3.18) shows the resulting likelihood for the r and A_d parameters. On the
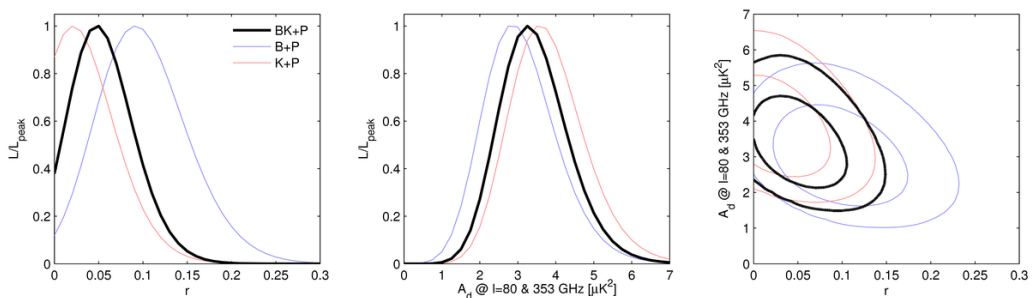
Figure 3.18: Likelihood results obtained from the power spectra of BICEP2/Keck array data at 150 GHz and Planck data at 353 and 217 GHz, considering a model of lensed-$\Lambda CDM + r$+dust. Solid black lines have been obtained using the combined BICEP2/Keck Array map, blue and red lines show how the results vary taking into account the BICEP2 and Keck Array map alone respectively. The left panel shows the estimation for the tensor-to-scalar ration r; the central panel gives the likelihood curve for the thermal dust amplitude (at $\ell = 80$ and 353 GHz). In the right panel the two dimensional contours enclose 68% and 95% of the total likelihood (BICEP2/Keck Array and Planck Collaborations 2015).

plots solid black lines correspond to the analysis performed considering the Planck and BICEP2/Keck combined maps, while blue and red curves refer to Planck plus BICEP2 or Keck data alone respectively. BICEP2 and Planck data alone produce and r likelihood that peaks at higher value than that for the Keck Array and Planck case. This is because for $\ell < 120$ the auto-spectrum B150×B150 is higher than for K150×K150, while the cross-spectrum B150×P353 is lower than K150×P353. However, both B2KP paper and BICEP2 and Keck Array collaboration V (2015) show that these discrepancies are compatible with noise fluctuations. Given the consistency between the two experiments, the combined result gives the best available measurement of the sky.

The combined likelihood curves give the following results: $r = 0.048^{+0.035}_{-0.032}$ ($r <$ 0.12 at 95% confidence level) and $A_d = 3.3^{+0.9}_{-0.8}\,\mu K^2$ (left and central panel of figure 3.18 respectively); the maximum likelihood on the grid has parameter $r = 0.05$ and $A_d = 3.30\,\mu K^2$ (right panel in figure 3.18). The probability to get a number smaller than what has been found for the tensor-to-scalar ratio, if in fact $r = 0$, is estimated to be of about 8%.

This important results put a stringent upper limit on the r parameter using purely B-modes measurements of the CMB. Several tests, to asses the robustness of this finding, have been made and are reported in the B2KP paper. In particular we describe here same variations from the fiducial model used to compute the likelihood analysis.

- **Planck spectra:** in the fiducial analysis Planck single frequency spectra have been evaluated considering the cross-correlation DS1×DS2. Switching to YR1×YR2 or HR1×HR2 makes little difference in the estimation of r (yellow curve on figure 3.19).

- **Excluding 217 GHz data:** dropping the Planck 217 GHz data from the likelihood analysis also makes little difference (red curve on figure 3.19).

- **Excluding 353 GHz auto-spectrum:** excluding the Planck 353 GHz spectrum from the analysis, leaving only the BK150×BK150 and BK150×P353 gives little changes (green curve on figure 3.19).

- **Extending the bandpower range:** in the fiducial analysis only the first five multiple bins of the power spectra have been taken into account. Extending the multipole range considering $20 < \ell < 330$ (nine bandpowers) has small effect on the results (magenta curve on figure 3.19).

- **Including E-modes spectra:** the EE spectra can be included in the analysis. In this case and fixing the BB/EE ratio to 0.5 for the dust emission (this is the value reported in the PIPXXX paper for large region of the sky) the estimation of r slightly shifts over higher value (blue curve on figure 3.19).

- **Relaxing the β_d prior:** using a less stringent prior on the thermal dust spectral index with $\beta_d = 1.59 \pm 0.33$ also pushes the peak of the r constraint up (cyan curve on figure 3.19).
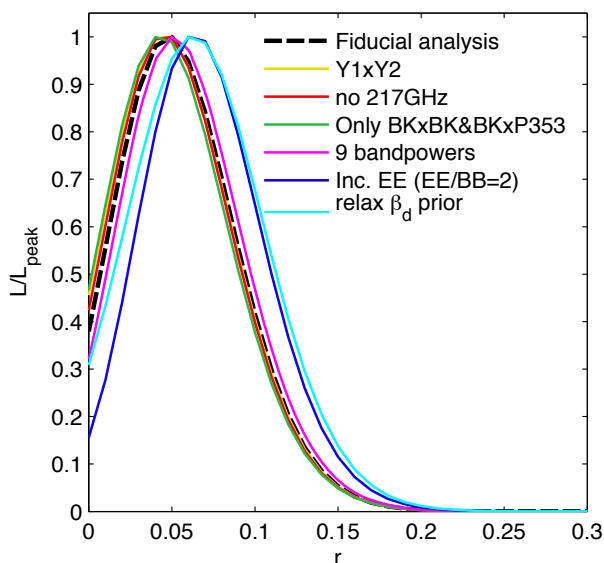
Figure 3.19: Variation in the likelihood results for r when changes are applied to the fiducial models. See text for details (adapted from BICEP2/Keck Array and Planck Collaborations 2015).

3.5 Concluding remarks

The BICEP2 and Keck Array data, with their combined sensitivity of about 57 nK on polarization maps at one degree resolution, represent a great progress toward the realization of CMB experiments with extremely high sensitivity. Their observations of an excess in the B-modes power spectrum over the lensed-ΛCDM model at angular scale of about on degree, compatible with a primordial gravitational waves signature with $r = 0.2$, forced the BICEP2, Keck Array and Planck collaborations to deeply analyze their data in order to get a correct interpretation of this signal.

The analysis of the Planck data at high frequency showed that the level of contamination from thermal dust emission is critical even in the BICEP2 field which is located far away from the Galactic plane. Nevertheless, even though Planck observations gave the unique possibility to get fundamental information on the polarized foreground emissions, their sensitivity is not optimal.

The joint analysis of the BICEP2/Keck Array and Planck maps and power spectra allowed us to estimate this level of contamination by cross-correlating data at 150 GHz from the two telescopes located at the South Pole, and data at 353 and 217 GHz from the Planck satellite. The results showed that the excess observed by BICEP2 and Keck Array in the B-modes spectrum is compatible with the sole emission from Galactic thermal dust. The likelihood analysis which has been performed by taking into account a lensed-$\Lambda CDM + r$+dust model gave a constraint on the value of the tenor-to-scalar ratio: $r = 0.048^{+0.035}_{-0.032}$. This statistical significance is too low to be interpreted as a detection of primordial B-modes of the CMB, but allows to put an upper limit at 95% confidence level with $r < 0.12$, which represents the most stringent upper limit on r obtained thanks to

only B-modes observations.

The final results from the BICEP2/Keck Array and Planck joint analysis confirm that the emission from our own Galaxy is absolutely not negligible even at high Galactic latitude. Therefore, to achieve in the future a possible detection of the CMB primordial B-modes, which still represents one of the great challenges of the modern observational cosmology, we will need to know in detail the polarized foreground emissions[3].

PIPXXX paper reports a complete analysis of the spatial dependence of polarized sky emission at 353 GHz at high Galactic latitude ($|b| > 35°$) on patches with dimension of about $400 \, \text{deg}^2$. This analysis has the goal to search for the cleanest regions of the sky, where the polarized thermal dust emission is low, which would be the optimal observation fields for future CMB experiments.

In particular, the amplitude of the B-modes power spectra of the Planck map at
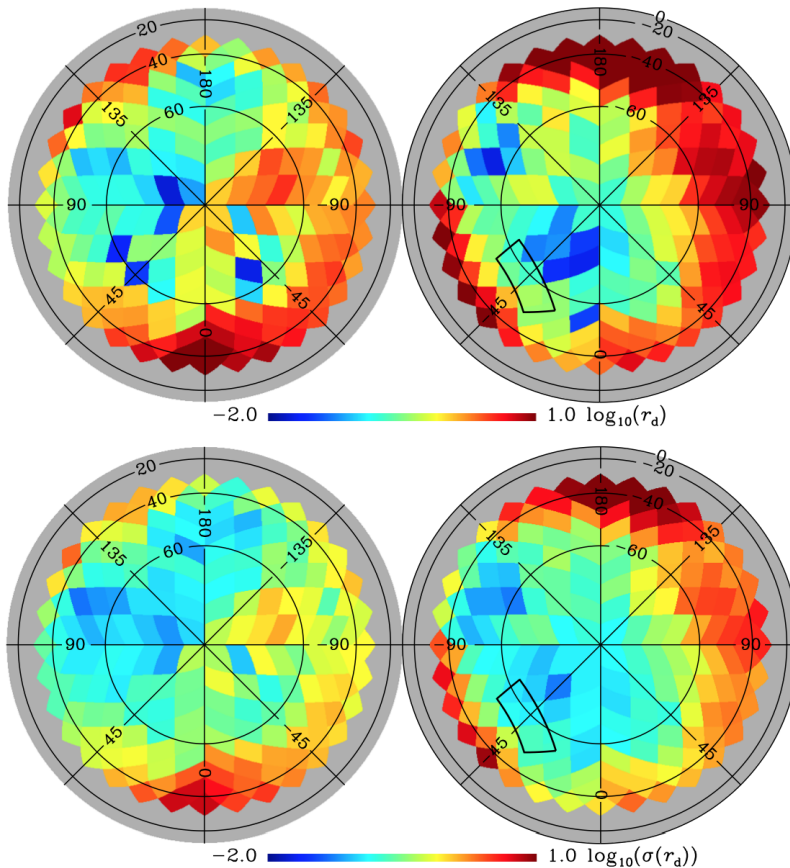
Figure 3.20: Thermal dust amplitude defined as $r_d = \mathcal{D}_{\ell=80}^{BB}(Dust)/\mathcal{D}_{\ell=80}^{BB}(CMB)$ (upper panel) and uncertainty $\sigma(r_d)$ (lower panel) on North (left panel) and South (right panel) polar caps , see text for details on how these values have been computed. The region highlight in black is the BICEP2 observing field (Planck Collaboration Int. XXX 2014).

---

[3]For a different approach to the problem see: https://www.youtube.com/watch?v=2INJiNpZFBI

353 GHz has been evaluated on 352 patches of the sky defined by the pixels in the HEALPix map at $Nside = 8$ having Galactic latitude $|b| > 35°$. The amplitude of the thermal dust B-modes spectra is computed in the usual way, by fitting the spectra with a power law $\mathcal{D}_\ell^{BB} \propto \ell^{-0.42}$ and evaluating the amplitude A^{BB} at $\ell = 80$ (where the maximum of the recombination bump of the CMB primordial B-modes is located). The value of the so obtained A^{BB} is rescaled to 150 GHz, a typical observation frequency for CMB experiment, with the usual modified blackbody frequency dependence and then is divided by the amplitude of the CMB B-modes spectrum at $\ell = 80$ in the case of $r = 1$ ($\mathcal{D}_{\ell=80}^{BB}(CMB) = 6.71 \times 10^{-2}\,\mu\text{K}^2$). The absolute value of $r_d = \mathcal{D}_{\ell=80}^{BB}(Dust)/\mathcal{D}_{\ell=80}^{BB}(CMB)$ is shown in the upper panel of figure (3.20) for each of the 352 pixels. Because the CMB primordial tensor B-modes power scales linearly with r, a value $r_d = 0.1$ would mean that the expected contamination from dust at $\ell = 80$ is equal to the amplitude of the primordial tensor of CMB for $r = 0.1$. For each of these estimates the uncertainties $\sigma(r_d)$ has been also computed as the quadratic sum of the fit errors on A^{BB} of the dust and the uncertainty arising from the extrapolation to 150 GHz (lower panel in figure 3.20). The r_d values[4] vary from -0.17 to more than 10 and $\sigma(r_d)$ ranges from as small as 5.6×10^{-2} to larger than 10. Taking the smallest value of $\sigma(r_d)$ we see that Planck measurements of the dust $\mathcal{D}_\ell^{BB}$ spectra for such small patches have, at best, a statistical uncertainty of 0.17 (3σ) in r_d units.

On the maps in figure (3.20) we can see that there is a high latitude region in the southern Galactic hemisphere for which r_d is quite low (located around Galactic coordinates $l = -30°$, $b = -70°$). This region is also associated with a rather small estimated uncertainty and thus might be an optimal observation field for future CMB experiment.

Nevertheless we want to stress again that, even though these maps of the spatial dependence of dust polarization amplitude give a great indication of where the emission is low, we would need future experiments with multiple frequency channels with high sensitivity in order to be able to characterize the foreground emissions and separate their contribution from the cosmological signal and eventually detect the footprint of primordial gravitational waves in the CMB radiation, if it exists.

---

[4]The fitted amplitudes A^{BB} for five of these patches are negative, but are consistent with $r_d = 0$ at 1σ

Part II

Systematic effects control for LSPE/STRIP experiment

Simulation pipeline for the STRIP instrument

In this chapter we focus on the second topic of the work done for this thesis: the implementation of a simulation pipeline for the low frequency instrument onboard a future balloon-borne experiment aimed at observing the CMB polarization, called *Large Scale Polarization Explorer* (LSPE).

The control of instrumental systematic effects is another important challenge for polarization CMB experiments. An extremely good knowledge of the instruments is mandatory to achieve a high level of control on systematic effects and limit their impact on the final scientific results. The implementation of simulation pipelines able to perform end-to-end simulations of the instrument architecture and behavior is a key step to identify the most important effects and to study removal and control strategies. The pipeline developed for the STRIP (*STRatispheric Italian Polarimeter*) instrument onboard LSPE, described in this chapter, has precisely this goal.

The chapter is organized as follows. Section (4.1) describes the LSPE experiment, the characteristics of the two focal plane instruments (4.1.1) and the expected scientific performance (4.1.2). Section (4.2) sketches the simulation pipeline developed for the STRIP instrument. Along with the description of the pipeline, some other technical concepts, useful to better understand the work done, are presented, regarding in particular the mission specification (4.2.1) and the characteristics of the detectors that composed the instrument (4.2.2). In section (4.3) and (4.4) we report the main obtained results. Finally, in section (4.5) we draw our conclusions.

4.1 The Large Scale Polarization Explorer

In the first chapter of this thesis we have emphasized the importance that the detection of the primordial B-modes signal of the CMB polarization would have in giving us information about the very first instants of the evolution of our universe and the inflationary period. Many experiments have been developed in the past several years with the primary goal to observe this signal and the actual status of the observations is reported in figure (1.9).

From the BICEP2 and Planck joint analysis, described in the previous part of this thesis, we have an upper limit on the tensor-to-scalar ratio, with $r < 0.12$ at 95% confidence level. As already pointed out, this limit represents, to this day, the most stringent constraint on r obtained from CMB B-modes observations. A similar constraint with

$r < 0.11$ at 95% confidence level comes from CMB temperature data collected by the Planck experiment (Planck Collaboration XIII 2015).

To further constraint the value of r or, hopefully, achieve the detection of primordial tensor modes, new generation of ground based and balloon-borne experiments are currently observing or are presently being developed or assembled. Moreover, new CMB dedicated space missions have been proposed to space agencies and their feasibility is under consideration.

Reaching a high sensitivity is obviously the first requirement for the new experiments. Furthermore, as the BICEP2/Planck joint analysis clearly has shown, the characterization of the foreground emissions is also extremely important. In order to achieve this characterization, it is fundamental to observe the sky at different wavelength and therefore to construct experiments with detector working in different frequency ranges. The LSPE experiment is set within this framework.

LSPE is a balloon-borne experiment aimed at observing the CMB and Galactic foreground polarized radiation in the frequency range between 43 and 240 GHz, at large angular scales, with angular resolution of $\sim 1.5°$ (LSPE Collaboration 2012). The experiment is financially supported by the Italian Space Agency (ASI) and is currently in the stage of assembling and testing. The balloon flight and sky observations are expected to take place during the arctic polar night of 2016/2017 (December 2016, January 2017).

In particular, the balloon and its payload will fly from the Svalbard Islands, reaching an altitude of about 40 km, in order to avoid atmospheric absorption and distortion of the sky signal. The balloon will perform a revolution around the Earth in about 15 days at the approximately constant latitude of $78°$ North, dragged by the stratospheric circular polar wind. In the past years, several experiments have been successfully carried out using balloons flying from Antartica around the South Pole (see for example BOOMERanG, Netterfield et al. 2002; SPIDER, Crill et al. 2008; EBEX, MacDermid et al. 2014). However, LSPE will be the first one to observe the sky during polar night flying around the North Pole. Test flights with dummy payloads have been performed and in figure (4.1) the path executed by one of them, similar to the path foreseen for LSPE, is shown.
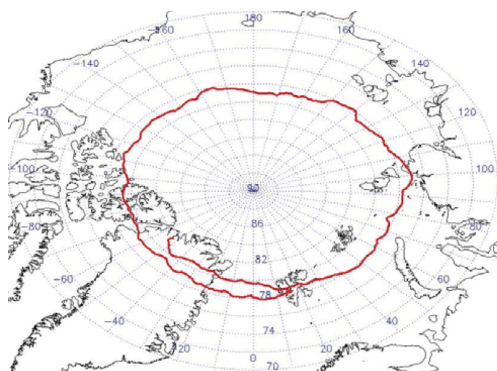

Figure 4.1: Path followed by one of the test flights performed by ASI to test the stratospheric circulation near the North Pole

A long duration flight during the polar night, therefore with the Earth shading the Sun radiation, has the great advantage to allow for the spinning of the gondola, giving the possibility to observe a large portion of the sky with the onboard instruments. LSPE gondola will indeed spin around its vertical axis at a constant angular velocity of 3 rpm.

LSPE is equipped with two instruments, composed by array of detectors, working in different frequency range: the STRIP instrument, sensible to radiation at 43 GHz, and the *Short Wavelength Instrument for the Polarization Explorer* (SWIPE) sensitive to radiation at 140, 220 and 240 GHz. Both instruments will observe the same portion of the sky, which will cover a wide fraction of the sky of about 30%.

Figure (4.2) shows simulated maps of Galactic (synchrotron and thermal dust) and CMB polarized radiations at the lowest (43 GHz) and highest (240 GHz) LSPE observing frequencies. On the maps the sky region observed by the STRIP instrument is highlighted. The impact of the foreground radiation for CMB measurements in the observed area is discussed in section (4.1.2).
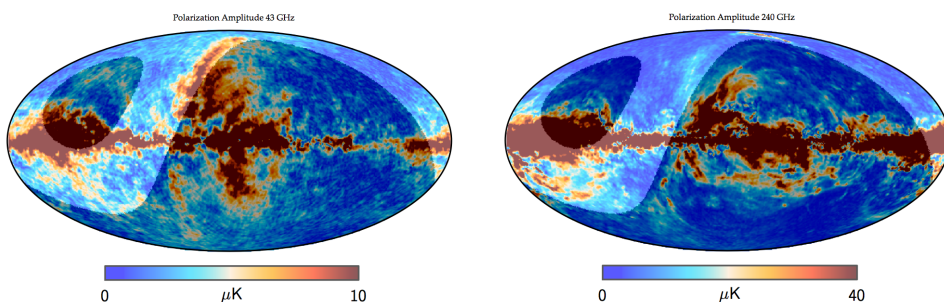

Figure 4.2: Polarization amplitude ($P = (Q^2 + U^2)^{\frac{1}{2}}$) of simulated maps at 43 (left panel) and 240 GHz (right panel) at 1.5 degree angular resolution. Maps (in Galactic coordinate system) contain polarized synchrotron, thermal dust and CMB radiation. The highlighted region corresponds to the sky region observed by the LSPE instruments.

4.1.1 Onboard instrumentation

LSPE is equipped with two instruments working in two different frequency ranges, in order to observe the foreground emissions and separate their contributions to isolate the CMB polarized signal. The SWIPE instrument uses bolometers to detect radiation in three frequency bands with $\nu > 140$ GHz (LSPE-SWIPE Collaboration 2012). The STRIP instrument, instead, uses an array of polarimeters, based on radiometric technology, working in a single frequency band centered at $\nu \simeq 43$ GHz (LSPE-STRIP Collaboration 2012).

The two instruments will share the same gondola carried by the stratospheric balloon, but they will work independently, with two different cryostats and two independent telescopes. Figure (4.3) reports a sketch of the envelopes of the instruments onboard the LSPE gondola. The green block represents the STRIP instrument, while the yellow one shows the SWIPE position and dimension. The brown part shows the location of the star tracker that will be used to locate the position of the gondola and set the system coordinate frame.
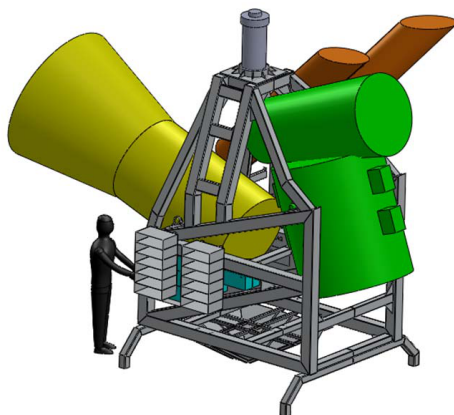
Figure 4.3: Sketch of the volume of the instruments onboard the LSPE gondola. The green block represents the STRIP instrument, while the yellow one shows the SWIPE position.

In the following, we briefly describe the two instruments focusing, in particular, on the STRIP characteristics, since the simulation pipeline developed in the context of this thesis is specifically built for this instrument.

SWIPE instrument

We describe here the SWIPE instrument architecture, which is also sketched in figure (4.4). The optical system consists of a single 470 mm diameter lens. Incoming radiation, passing through the lens, is split by a fixed polarizer into the two orthogonal linear polarization components that are focused on two different curved focal planes, where the detectors are located. the SWIPE detectors are bolometers coupled with multi-mode feed horns, working in three different frequency bands. In the current configuration (still in phase of optimization) the SWIPE design consists of about 130 detectors with central frequency $\nu \simeq 140\,\mathrm{GHz}$, 90 detectors with $\nu \simeq 220\,\mathrm{GHz}$ and 110 detectors with $\nu \simeq 240\,\mathrm{GHz}$. The two focal planes, which have a diameter of about 300 mm, have an identical configuration, so that half of the detectors for each band are located in each of them.

The propagation of several modes is obatined using parabolic Winston horns (Maffei et al. 2004). Unlike other bolometric balloon-borne missions, like EBEX and SPIDER, which use a very large number of detectors (> 1000), SWIPE uses a limited number of bolometers, coupled with multi-mode antennas, to achieve comparable sensitivity. This approach considerably simplifies the detector array at the cost of a coarser angular resolution. The modes propagating in the antennas are coupled in such a way that gives comparable angular resolution of about 90 arcmin at all the three frequencies.

A rotating Half Wave Plate (HWP) is located in front of the optical system and modulates the incoming linearly polarized signal. The presence of this polarization modulator, together with the fixed polarizer placed in front of the focal planes, permits to measure both the orthogonal polarization with the same detector giving the possibility to recover both the Stokes Q and U parameter of the incoming radiation.
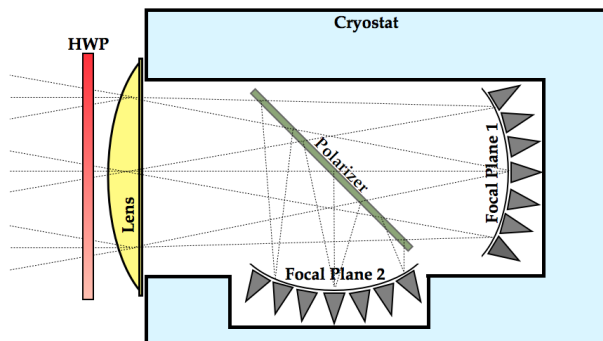
Figure 4.4: Sketch of the SWIPE instrument onboard the LSPE experiment. For a description of the different components see text.

The full instrument is enclosed in a large liquid ^{4}He cryostat with an available volume of about 250 liters, enough for more than 30 days of operation. The focal planes are cooled down to a temperature of about 0.3 K.

STRIP instrument

The STRIP instrument is aimed at observing the sky polarized radiation in a single frequency band centered at $\nu \simeq 43$ GHz with a bandwidth of about 20%, giving thus the possibility to monitor the synchrotron Galactic emission which dominates at this frequency.

STRIP detectors are coherent polarimeters based on the design of the QUIET receivers (QUIET Collaboration 2011), which provides excellent redundancy and suppression of systematic effects inherent to the receivers themselves (see section 4.4). In the STRIP focal plane an array of 49 polarimeters is coupled with corrugated feed horns, circular polarizers and OrthoMode Transducers (OMT). Each module measures directly the Stokes Q and U parameters of the observed sky. The radiometric chain is based on cryogenic High Electron Mobility Transistor (HEMT) low noise amplifiers and on high-performance waveguide components cooled to 20 K and integrated in Monolithic Microwave Integrated Circuits (MMIC). A description of the complete functioning of the radiometric chain is reported in section (4.2.2).

The STRIP corrugated feed-horns modules have been realized with the platelet technique, consisting in the overlapping of metal plates with holes of proper sizes in order to realize the electromagnetic profile of the feed-horns (Del Torto et al. 2011). Fabrication techniques normally used for corrugated feed-horns, such as direct machining or electroforming, become time-consuming and cost-ineffective for the production of arrays with large number of elements. The platelet technique allows for reduced times and costs with respect to typical techniques, realizing more elements at the same time. The STRIP focal plane unit consists of seven hexagonal modules each composed by seven
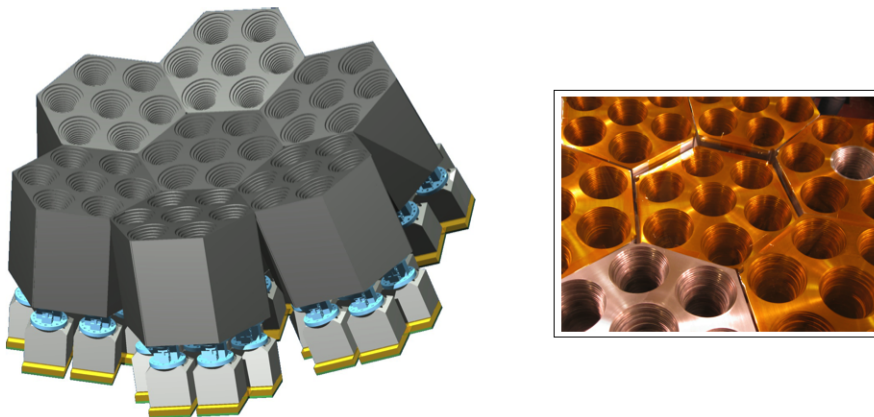
Figure 4.5: Left panel: rendering of the LSPE-STRIP 43 GHz focal plane unit. Each hexagonal feed horns module (dark gray) is connected to Polarizers (blue), OMT (light gray) and polarimeters (yellow). Right panel: photo of the constructed feed horn modules.

feed horns[1]. Figure (4.5) shows a rendering of the STRIP focal plane unit, together with a photo of the already constructed feed horns. The antennas angular response has been tested with results showing excellent agreement with what expected from previously computed simulations (maximum discrepancy between tested response and simulations at the level of $0.1\,\mathrm{dB}$).

The STRIP optical system, independent from the SWIPE one, is composed by a dual reflector telescope in the dragonian configuration (Dragone 1978), with primary mirror diameter of about 600 mm. This scheme offers excellent performance (angular resolution, polarization purity, symmetry) over a wide focal region. The final angular resolution of the telescope-antenna system is of ~ 90 arcmin.

The instrument baseline design calls for an operating temperature of ~ 20 K, with a temperature stability requirement of $\sim 1\,\mathrm{mK}$.

4.1.2   Scientific performance

Figure (4.6) summarizes the expected performance of the LSPE experiment. The primary target of the experiment is to constraint the tensor-to-scalar ratio of primordial perturbations amplitudes down to $r \simeq 0.05$. Given the described sky scanning strategy of the experiment, covering a large portion of the sky of about 30% and the angular resolution of about 90 arcmin for all the frequencies, LSPE will be able to constraint the CMB power spectra observing the very large angular scales.

In figure (4.6) the level of Galactic foreground emissions is compared with the CMB

---

[1]The entire module, composed by the 49 feed horns has been fully designed, assembled and tested at the Physics Department of the University of Milan.
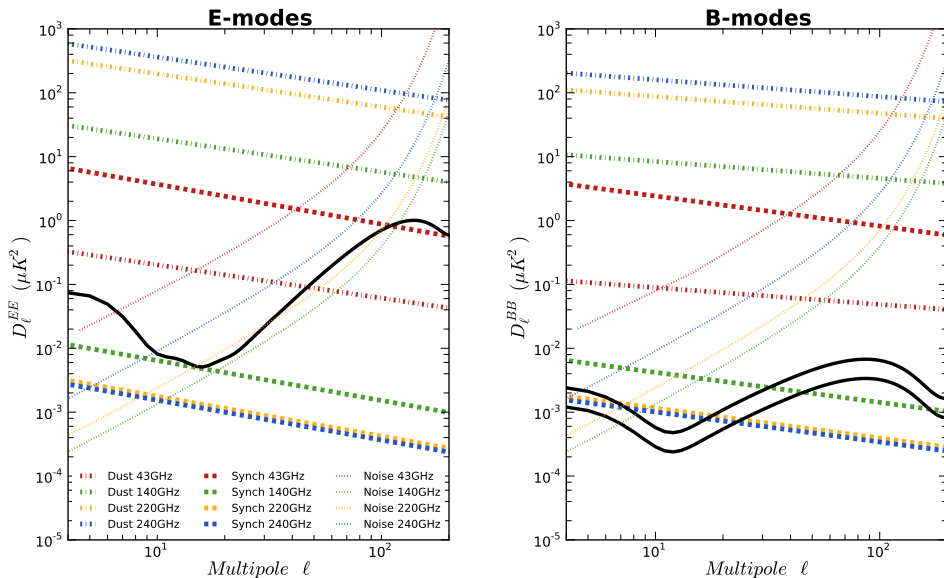
Figure 4.6: Expected scientific performance for the LSPE experiment. Different colors in the plots refer to the four frequency channels of the experiment: 43 GHz (red), 140 GHz (green), 220 GHz (yellow) and 240 GHz (blue). Dashed and dashed-dotted curves show the level of Galactic synchrotron and thermal dust polarized emission respectively at the various frequencies, and are computed by considering the sky region observed by the instruments from simulated maps. Dotted lines represent the expected spectra of noise. Black lines are the power spectra of the CMB computed considering $\tau = 0.08$ and $r = 0.1/0.05$ (upper/lower black curves on right panel).

power spectra and the expected noise of the detectors in the four frequency channels. In particular, we considered maps of the synchrotron and thermal dust emissions at the various frequencies, simulated using the Planck Sky Model (PSM) package (Delabrouille et al. 2013). In each case the linear spectra shown on the plots are obtained by fitting with a power law in ℓ the foreground spectra computed from these simulated maps, considering only the sky region observed by the LSPE experiment (see figure 4.2).

On such a large portion of the sky and at the considered angular scales, the thermal dust emission dominates over the CMB B-modes signal at all the four frequencies. Moreover, the synchrotron emission also contributes to the overall signal even at the highest frequency of 220 and 240 GHz, with power spectra comparable with those of the CMB B-modes radiation for $r = 0.1/0.05$. For this reason, having the STRIP instrument as low frequency foreground monitor is crucial to perform the separation of the astrophysical components and isolate the CMB signal.

4.2 Overview on the pipeline modules

In this section we describe the simulation pipeline we have built as a preliminary step to asses the scientific performance of the STRIP instrument onboard the LSPE ex-

periment. The pipeline has the goal to study the actual behavior of the instrument with
end-to-end simulations.

The inputs of the pipeline are realistic simulated maps of the sky, which can include
the polarized signal of the different astrophysical components (CMB and foreground
radiations). The pipeline simulates the observation of these maps by the instrument,
considering the pointing direction, the sky scanning strategy, the optical characteristics
and the polarimeter architecture. Its outputs are the Time Ordered Data (TOD) of this
simulated observations which include realistic representations of the noise and the pres-
ence of different possible systematic effects. The obtained TOD can then be projected on
maps to get a representation of the sky as observed by the instrument and from them the
related power spectra can be computed.

The pipeline is composed by two parts: the first one is based on the Planck Level-
S simulation pipeline (Reinecke et al. 2006), modified according to the LSPE mission
specification; the second part accounts for the STRIP polarimeter architecture. A flow
chart of the implemented pipeline is shown in figure (4.7), the detailed description of the
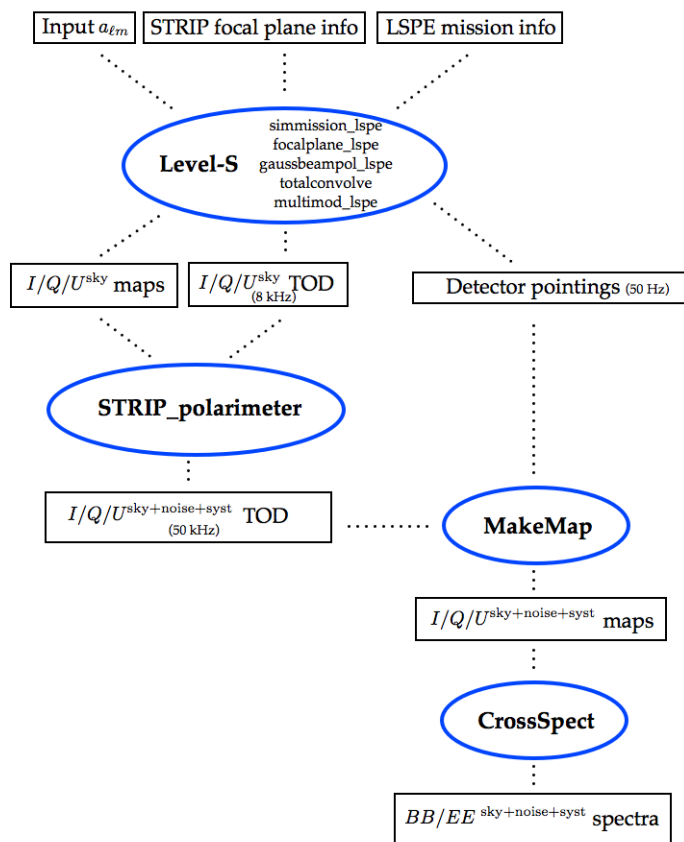different blocks is reported in the next sections.

Figure 4.7: Flow chart representation of the simulation pipeline for the STRIP instrument onboard
the LSPE balloon.

4.2.1 Simulating the LSPE mission and scanning strategy

The first part of the implemented STRIP simulation pipeline is based on the simulation modules developed for the Planck space mission, the so called Level-S pipeline. The entire set of modules and their application to the Planck instrumentation are fully described in Reinecke et al. (2006) and references therein. Here we describe the ones adapted to the LSPE mission and STRIP characteristics. The module described below are represented in figure (4.7) as a single block in the flow chart named Level-S.

focalplane_lspe: this module converts a text file containing several information on the instrument focal plane (the so called focal plane database) into the `fits` format[2]. The focal plane database includes data about each focal plane detector, in particular: a detector ID string, the position in the focal plane, the polarization angle, the observing frequency, the sampling frequency at which the final output TOD are sampled, the detector beam FWHM, ellipticity and orientation. In the case of STRIP simulations the focal plane database is thus composed by 49 lines, corresponding to the 49 detector elements of the instrument. In the simulations discussed in this work, each detector has the same characteristics (i.e: beam property, observing frequency, sampling frequency, polarization angle), the only difference is the position in the focal plane that reflects the actual configuration of the detector array.

simmission_lspe: the output of this module is a table containing the position and orientation of the LSPE gondola in fixed time intervals during the entire mission. In particular, this module has been modified in order to account for the actual sky scanning strategy: a flight at constant latitude (fixed at $78°$ North in our simulations), performing a complete revolution around the Earth in 15 days. The module also takes into account the gondola spinning around its vertical axis with a constant velocity of 3 rpm.

gaussbeampol_lspe: this module generates the optical beam $a_{\ell m}$ coefficients that are then convolved with the $a_{\ell m}$ of the input simulated sky maps. In particular it takes a detector name as input, looks up the detector beam characteristics in the focal plane database and produces the coefficient accordingly. The module can generate axisymmetric or elliptical Gaussian beams with and without polarization.

totalconvolve: this module takes as input the spherical-harmonic coefficients of the simulated sky map that we want to observe with our simulations and the beam $a_{\ell m}$ of each detector (computed with the *gaussbeampol_lspe* module). It then computes the convolution of sky and beam for all possible directions and orientations of the beam relative to the sky (see Wandelt & Górski 2001 for details on how the convolution is performed). Both unpolarized and polarized convolutions are supported. In the polarized case, three sets of spherical harmonics are required for sky and beam, respectively, for the Stokes $I/Q/U$ parameters.

---

[2]Flexible Image Transport System (`fits`) is a digital file format useful for storage, transmission and processing of scientific images and tables. `fits` files are most commonly used in astronomy. The input and output files used in the developed pipeline and shred between modules are all written and stored in this format.

multimod_lspe: this module produces the time stream of the detector pointings for each detector in the focal plane database, at the wanted sampling frequency and the so called *hits* map, which gives the number of detector pointings falling in each pixel at the desired HEALPix $Nside$ resolution. The module obtains the detector pointings, at the desired sampling frequency, by interpolating the gondola positions and orientations obtained with the *simmission_lspe* module and rotating them considering the actual position and orientation of each detector relative to the gondola coordinate frame. Then the module uses these detector pointings and the output of the *totalconvolve*, to calculate the radiation falling into each detector (for the three Stokes parameter $I/Q/U$) producing the final TOD files that take into account the convolution of the simulated sky with the beam. $I/Q/U$ maps of the simulated observed sky can also be produced.

In our simulation pipeline we used the described Level-S modules with two main purposes. The first one is to simulate the scanning strategy of the experiment and, by changing the STRIP telescope elevation and the detectors configuration in the focal plane (i.e the position of the antenna modules in the focal plane), to obtain the effective sky coverage and hits map. The second purpose of the Level-S modules is to obtain the input for the following part of the pipeline, which simulates the polarimeter architecture as described in the next section.

In the first phase of our analysis we studied different configurations for the STRIP focal plane, obtaining for each of them the final sky coverage of the mission and the expected sensitivity in the observed region. The final configuration which will be assembled on the LSPE gondola is shown in the left panel of figure (4.8). This configuration, among the other considered in the analysis, is the most compact one, implying a slightly
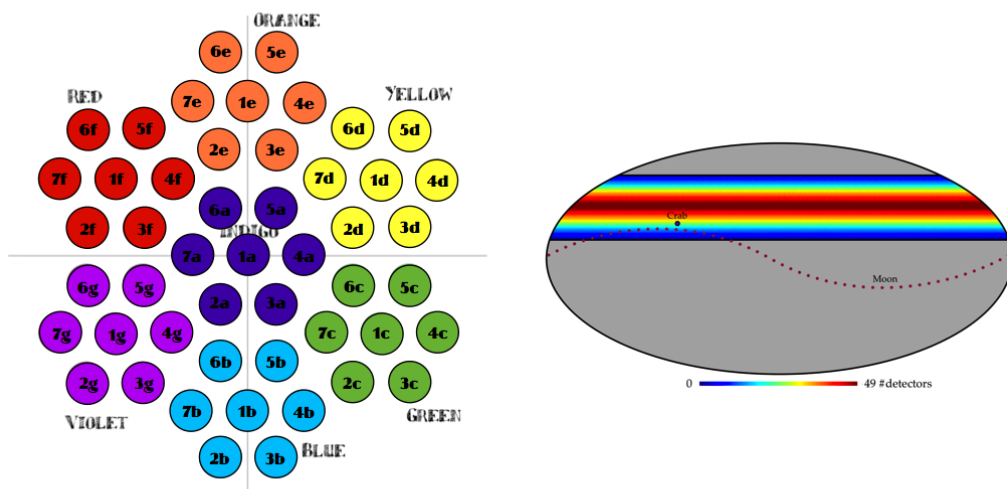

Figure 4.8: Configuration of the LSPE antenna modules in the focal plane (left panel) and sky map, in equatorial coordinates, showing the total number of detectors observing each pixel (right panel). On the map the position of the Crab Nebula and the Moon (December 2016) are also reported.

smaller final coverage of the sky but a higher sensitivity.

The right panel of figure (4.8) shows the total number of detectors observing each pixel on the map, for an elevation of the STRIP telescope[3] of $34.8°$. This elevation provides the maximum superposition between the region observed by STRIP and SWIPE. The observed sky fraction considering this configuration is $f_{sky} \simeq 0.30$. The scanning strategy is such that antennas located on the same vertical axis in left panel of figure (4.8) will observe exactly the same region of the sky. A central region covering about 3% of the sky will be observed by all the 49 detectors. This scanning strategy, with multiple detectors observing the same area of the sky, will give the possibility to perform several null tests in order to check for the presence of systematic effects.

The map in figure (4.8) also shows the position of the Crab Nebula and the Moon in the period of December 2016. These two sources will be the primary STRIP in-flight calibrators. In particular the Crab Nebula represents the brightest polarized point source in the sky and, considering the nominal scanning strategy, will be observed by 24 of the total 49 STRIP antennas, twice per day. A temporary change of the telescope elevation during the flight is an option, in order to observe this source with all the STRIP antennas and perform an in-flight absolute responsivity calibration for all the detectors. The Moon is a possible polarization angle calibrator, as shown by past experience with the QUIET instrument (QUIET Collaboration 2011). With the nominal scanning strategy, and considering December 2016 as the flight period, the Moon will be observed by 14 STRIP antennas.

The second purpose of the Level-S simulation block is to obtain Stokes $I/Q/U$ time stream data as observed by the STRIP optics (the output files of the *multimod_lspe* module). These TOD files are then the input for the second block of our pipeline, named in figure (4.7) as *STRIP_polarimeter*, which is described in the following sections.

4.2.2   Simulating the polarimeters architecture

STRIP is equipped with the Q-band polarimeteres designed for the QUIET experiment. Each of the 49 polarimeters is coupled with a feed horn, a circular polarizer and a OMT. Figure (4.9) shows a sketch of the radiometric chain, reporting all the different passive and active components. Each polarimeter has two legs (denoted as A and B) where, as described in the following, the two orthogonal polarization states of the incoming radiation propagate. The outputs of the two pairs of diodes are proportional to the Stokes Q and U parameters of the observed signal (in the polarimeter coordinate frame). For a detailed description of the polarimeters architecture we refer to Newburgh (2010) and Bischoff (2010); we report a simple mathematical characterization for each polarimeter component (following a matrix formalism) which is useful to understand the simulation pipeline description that follows. Here we describe the case of an ideal polarimeter, the possible different non-idealities which may impact the final output are described in section (4.4).

Polarizer: the linearly polarized radiation captured by the feed horn enters the polarizer which combines the two components (E_x, E_y) into an output proportional to left and right circularly polarized signal. The matrix describing the polarizer functioning

---

[3]The elevation is defined as the angle between the direction of pointing of the telescope and the celestial equator
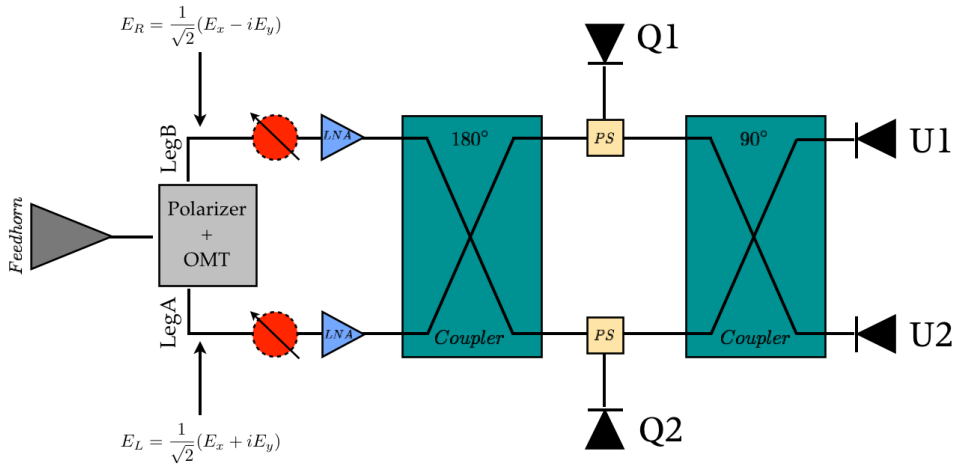
Figure 4.9: Sketch of the radiometric chain which composed the STRIP detectors. The different components are briefly described in the text.

can be written as:

$$S^{PL} = \begin{pmatrix} 1 & i \\ 1 & -i \end{pmatrix} \tag{4.1}$$

OMT: the two circularly polarized components from the polarizer are split by the OMT, according to the following operator:

$$S^{OMT} = \frac{1}{\sqrt{2}} \begin{pmatrix} 1 & 0 \\ 0 & 1 \end{pmatrix}. \tag{4.2}$$

Therefore, in the two polarimeter legs the signal proportional to the left and right circular polarization propagates respectively, as marked in figure (4.9).

Phase Switches: on both legs of the polarimeter a phase switch is present which adds a phase to the propagating signal (red symbols on figure 4.9). The added phase, in the ideal case, switches between 0 and π at a fixed frequency which is different for the two legs. The matrix describing the effect of these components can be written as:

$$S^{PhSw} = \begin{pmatrix} e^{i\varphi_A} & 0 \\ 0 & e^{i\varphi_B} \end{pmatrix} \quad \text{with } \{\varphi_A, \varphi_B\} = 0, \pi. \tag{4.3}$$

Amplifiers: on each leg of the polarimeter the signal is amplified in three different stages. Two Low-Noise Amplifiers (LNA) are located before the phase switch and a third one after it. We include these three amplification stages in one single operator (shown in light blue on figure 4.9):

$$S^{Amp} = \begin{pmatrix} g_A & 0 \\ 0 & g_B \end{pmatrix} \tag{4.4}$$

180° Coupler: this coupler mixes the signal propagating in two legs according to the following operator:

$$S^{180°} = \frac{1}{\sqrt{2}} \begin{pmatrix} 1 & 1 \\ 1 & -1 \end{pmatrix} \tag{4.5}$$

Power Splitters: the signals propagating after the $180°$ coupler are split by the power splitters. Half of the power arrives to the first pairs of diodes (Q1 and Q2 in figure 4.9), while the second half propagates in the final stages of the radiometric chain. The power splitter effect can be simply described by:

$$S^{PowSp} = \frac{1}{\sqrt{2}} \begin{pmatrix} 1 & 0 \\ 0 & 1 \end{pmatrix} \tag{4.6}$$

90° Coupler: the second coupler mixes again the signals propagating in the two legs in order to have signals proportional to the Stokes U parameter of the observed radiation in the second pairs of diodes (U1 and U2 in figure 4.9). The operator describing this component can be written as:

$$S^{90°} = \frac{1}{\sqrt{2}} \begin{pmatrix} i & 1 \\ 1 & i \end{pmatrix} \tag{4.7}$$

We can write the final signals detected by the diodes as:

$$\begin{pmatrix} Q1 \\ Q2 \end{pmatrix} = \begin{pmatrix} E_{Q1} \\ E_{Q2} \end{pmatrix}^2 = \left[S^{PowSp} S^{180°} S^{Amp} S^{PhSw} S^{OMT} S^{Pol} \begin{pmatrix} E_x \\ E_y \end{pmatrix} \right]^2, \tag{4.8}$$

$$\begin{pmatrix} U1 \\ U2 \end{pmatrix} = \begin{pmatrix} E_{U1} \\ E_{U2} \end{pmatrix}^2 = \left[S^{90°} S^{PowSp} S^{180°} S^{Amp} S^{PhSw} S^{OMT} S^{Pol} \begin{pmatrix} E_x \\ E_y \end{pmatrix} \right]^2. \tag{4.9}$$

By including the previously defined operators and by taking into account the definition of Stokes (I, Q, U, V) parameters in terms of E_x and E_y[4] the final output signals can be written as:

$$\begin{pmatrix} Q1 \\ Q2 \end{pmatrix} = \frac{1}{8} \begin{pmatrix} g_A^2 \frac{\mathbf{I+V}}{2} + g_B^2 \frac{\mathbf{I-V}}{2} \pm g_A g_B \mathbf{Q} \\ g_A^2 \frac{\mathbf{I+V}}{2} + g_B^2 \frac{\mathbf{I-V}}{2} \mp g_A g_B \mathbf{Q} \end{pmatrix}, \tag{4.10}$$

$$\begin{pmatrix} U1 \\ U2 \end{pmatrix} = \frac{1}{8} \begin{pmatrix} g_A^2 \frac{\mathbf{I+V}}{2} + g_B^2 \frac{\mathbf{I-V}}{2} \mp g_A g_B \mathbf{U} \\ g_A^2 \frac{\mathbf{I+V}}{2} + g_B^2 \frac{\mathbf{I-V}}{2} \pm g_A g_B \mathbf{U} \end{pmatrix} \tag{4.11}$$

where we have considered a simplified case: the phase switch on legA of the polarimeter has fixed phase $\varphi_A = 0$, while the one on legB is switching with $\varphi_B = 0, \pi$; the $\pm$ which appears in front of terms $\propto g_A g_B$ originated from this phase switch action.

From relations (4.10) and (4.11) it is evident that, in case of linearly polarized radiation ($V = 0$), adding together the phase switch stages gives a detected signal proportional to the total intensity I of the incoming radiation, while by differentiating them the output signal is proportional to the Stokes Q and U parameters.

---

[4] $I = |E_x|^2 + |E_y|^2, Q = |E_x|^2 - |E_y|^2, U = 2\Re(E_x^* E_y)$

The effect of the second phase switch is to flip again the sign of the terms proportional to Q and U detected by each diode. The final polarized signal is thus obtained by computing a so called double demodulation:

$$Q1_{DD} = (Q1^{\varphi_A=0,\varphi_B=0} - Q1^{\varphi_A=0,\varphi_B=\pi}) - (Q1^{\varphi_A=\pi,\varphi_B=0} - Q1^{\varphi_A=\pi,\varphi_B=\pi})$$
$$= \frac{1}{2}g_A g_B \mathbf{Q} \tag{4.12}$$

and similarly for all the other diodes.

In the case of the STRIP polarimeter the phase switch in legB is working at the high frequency of 4 kHz, while the one in legA at the lower frequency of 50 Hz. The fast demodulation at 4 kHz is necessary to strongly reduce the presence of the $1/f$ noise in the final detected polarized signal, which is introduced by the LNA and that otherwise would strongly impact the final detection. The second demodulation is instead used to remove a possible leakage from Stokes I to Stokes Q/U as will be better explained in section (4.4).

Relations (4.10) and (4.11) do not take into account the presence of noise in the final detected signal. We can include it by considering:

$$Q1^{\varphi_A=0,\varphi_B=0} = \frac{1}{16}\left[G_A\left(1 + \Delta G_A^{oof} + \Delta G_A^{wn}\right)(\mathbf{I} + T_A)\right] +$$
$$\frac{1}{16}\left[G_B\left(1 + \Delta G_B^{oof} + \Delta G_B^{wn}\right)(\mathbf{I} + T_B)\right] + \tag{4.13}$$
$$\frac{1}{8}\sqrt{G_A\left(1 + \Delta G_A^{oof} + \Delta G_A^{wn}\right)}\sqrt{G_B\left(1 + \Delta G_B^{oof} + \Delta G_B^{wn}\right)}\mathbf{Q}$$

and similarly for the other phase switch stages and the output of the other diodes. In equation (4.13) we have that $G_{A/B} = g_{A/B}^2$, $\Delta G_{A/B}^{oof}$ and $\Delta G_{A/B}^{wn}$ represent the noise introduced by the amplifiers in the two legs of the polarimeter, which includes a $1/f$ (oof) and a white noise (wn) component and $T_{A/B}$ are the amplifier noise temperatures in the two legs of the module. We have considered the case with $V = 0$, meaning linearly polarized observed radiation.

Equation (4.13) and the similar ones for the other diodes represent the starting point of our simulation of the polarimeters architecture. They give the final output of the detectors as a function of the Stokes $I/Q/U$ parameters of the sky as observed by STRIP telescope and antennas. The values of the Stokes parameters in each point of the observed sky, taking into account the LSPE scanning strategy and the convolution with the beam, can be obtained from the first part of our simulation pipeline, i.e. the Level-S modules described in the previous section. The $I/Q/U$ TOD files produced by the Level-S modules are then the input of the second part of the pipeline, named as *STRIP_polarimeter* in figure (4.7). This module is coded using the python programming language and in the simplest case, which do not include the presence of systematic effects, directly combines the Level-S output TOD as in equation (4.13), adding to them realistic realizations of the noise and implementing the different phase switch stages to get the final polarimeter outputs as in equation (4.12).

The white noise RMS of the amplifier gain variations, $\sigma(\Delta G_{A/B}^{wn})$, can be obtained by considering the case of an ideal and perfectly balanced polarimeter ($G_A = G_B \equiv G$, $\sigma(\Delta G_A^{wn}) = \sigma(\Delta G_B^{wn}) \equiv \sigma(\Delta G^{wn})$, $T_A = T_B \equiv T_{sys}$) with uncorrelated noise between

the two legs and the different phase switch stages, and by imposing that the final sensitivity on Stokes Q and U parameters for the sampling time interval in the final TOD files is the one expected from a radiometer with the architecture of figure (4.9):

$$\Delta(Q/U)^{wn} = \frac{1}{\sqrt{2}} \frac{T_{sky} + T_{sys}}{\sqrt{\beta\tau}} \tag{4.14}$$

where T_{sky} is the brightness temperature of the observed radiation, β is the frequency bandwidth of the detector and τ is the integration time, which is the inverse of the final sampling frequency.

To perform a realistic simulation of the polarimeter architecture, we needed to implement the phase switches functioning with their actual switching frequency of 4 kHz (legB) and 50 Hz (legA). Consequently, the inputs of the *STRIP_polarimeter* module, for each of the 49 detector of the STRIP instrument, are:

- TOD files of the Stokes $I/Q/U$ parameters at a sampling frequency of 8 kHz produced by the Level-S modules;

- time stream realizations of the noise at a sampling frequency of 8 kHz with RMS calculated as described previously and which can eventually include also a $1/f$ component with knee frequency f_k[5];

- values of the amplifier gains $G_{A/B}$ and noise temperatures $T_{A/B}$.

The outputs are the time streams of the detection of each diode after the double demodulation. These TOD files thus include signals proportional to Stokes Q/U parameters of the simulated incoming radiation (for diodes Q1/Q2 and U1/U2 respectively) at the final sampling frequency of 50 Hz.

In principle, for each diode, we could also produce TOD files proportional to the total intensity I of the simulated observed sky, by adding together the phase switch stages. Nevertheless these detections are strongly contaminated by the presence of the $1/f$ noise component which would dominate over the sky signal (see next section). For this reason in our pipeline we consider only the double demodulated signals.

The two pairs of TOD files proportional to Q and U obtained for each detector are projected on maps considering the time stream of the detector pointings at the same 50 Hz sampling frequency (computed with the *multimod_lspe* module). At the end of the simulation process we have 49 pairs of Q/U maps, obtained from diodes Q1/U1 and Q2/U2 of each polarimeter. All the 49 maps from diodes-1 can be added together, and so also the ones from diodes-2, obtaining two simulated polarization maps of the sky as observed by the entire STRIP instrument. These two maps have independent noise and are thus useful, for example, to computed EE and BB cross-spectra. Obviously we can also add together these two maps to obtain the final simulated observation of the sky with the full sensitivity.

Processing the TOD files at the sampling frequency of 8 kHz for all the 49 STRIP detectors is computational expensive. For this reason we do not simulate the total LSPE mission duration of 15 days but we take into account the fact that, considering the nominal scanning strategy of the experiment, the full coverage of the observed portion of

---

[5]In our definition the $1/f$ noise has frequency spectrum: $S(f) \propto 1/f^\alpha$ and the knee frequency (f_k) represents the frequency at which the $1/f$ noise and the white noise contribution are equal.

the sky ($f_{sky} \simeq 0.3$) is accomplished in 22.5 hours. Consequently, we consider this time interval in our simulations and reduce the RMS of the amplifier noise accordingly (i.e. $\tilde{\sigma}(\Delta G^{wn}) = \sigma(\Delta G^{wn})/\sqrt{16}$, since the sky scanning is repeated in exactly the same way 16 times in the total 15 days of the balloon flight).

4.3 End-to-end simulation in the ideal case

We run a first set of end-to-end simulations considering the case of ideal polarimeters described previously. The simulated map we used as our input sky is the one shown in figure (4.2, left panel). This map has been computed using the PSM package and includes polarized foreground emission at 43 GHz, in particular thermal dust radiation and synchrotron, and a representation of the CMB sky obtained considering the Planck best-fit set of cosmological parameters (Planck Collaboration XIII 2015) and primordial tensor modes with tensor-to-scalar ratio $r = 0.1$.

The end-to-end simulation includes all the module blocks shown in figure (4.7) and provides, as final output, the polarized map and power spectra as observed by STRIP. In this first case we implemented the simulation for an ideal experiment, without including any possible systematic effects and considering perfectly balanced polarimeters.

Even though, as previously mentioned, the output TOD files of the *STRIP_polarimeter* module are obtained by considering the double demodulation of the phase switch stages, in one single case we run the simulation computing also the sum of the different stages getting therefore output proportional to the total intensity I of the simulated incoming radiation. We run this test in order to asses the level of suppression of the $1/f$ noise contribution in the differenced output compared to the summed one. We therefore included the $1/f$ noise component in our simulations, as in equation (4.13), with a knee frequency of 100 Hz. The frequency spectra of the resulting TOD (computed with a Fast

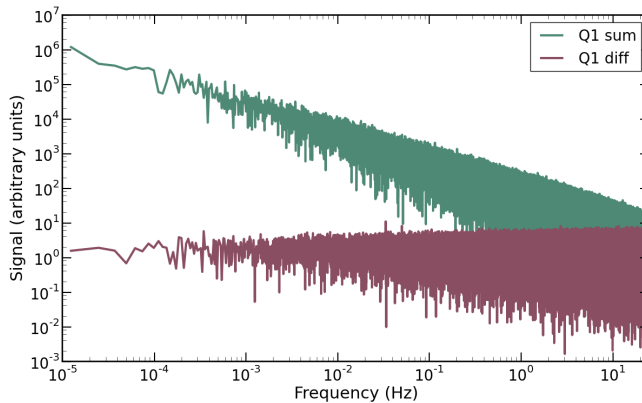**Figure 4.10:** Frequency spectra of the output TOD files of the simulations for one single diode of on polarimeter, in order to assess the scientific performance of the instrument. The green spectrum is obtained by summing the different phase switch stages, while the purple one by differencing them. We see that the fast demodulation efficiently suppressed the $1/f$ noise component in the differenced output.

Fourier Transform algorithm) are shown in figure (4.10), for one single diode (Q1) of one polarimeter; results for the other diodes are similar. We clearly see that, in the case of double demodulated output (purple spectrum), the $1/f$ noise in efficiently suppressed and its frequency spectrum is compatible with white noise. Nevertheless, we recall that our simulations are computed on time stream with a total length of 22.5 hours, and therefore any long time variation with time constant longer than this time interval is not visible. On the contrary, the output TOD proportional to the total intensity (green spectrum) is highly contaminated by the $1/f$ noise which prevents to gather information about sky emission using this signal.
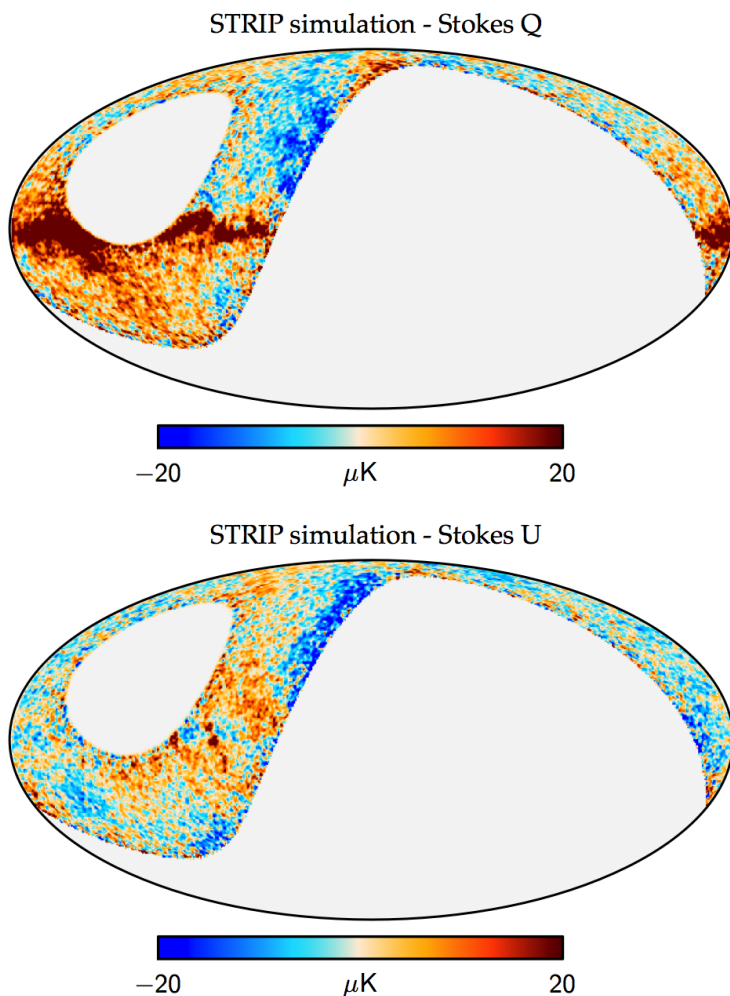

Figure 4.11: Output Stokes Q and U map from the end-to-end simulation in Galactic coordinates. These maps are computed as the weighted average of the 49 polarization maps obtained from each of the STRIP detector and are smoothed to $2°$ angular resolution to highlight the polarized Galactic signal.

To complete the end-to-end simulation we simulated the observation of the sky by all the 49 STRIP detectors. Figure (4.11) shows the Q and U maps computed by averaging together the polarization maps obtained for each detector (using as weight the inverse of the RMS per pixel). These maps are smoothed to $2°$ angular resolution to highlight the Galactic signal. The mean RMS of the noise on Q and U final maps at $Nside = 256$, at the nominal angular resolution of $1.5°$ and considering $T_{sys} = 20\,\mathrm{K}$ for all the polarimeters, is of $\sim 23\,\mu\mathrm{K}$.

From the maps, E and B-modes angular power spectra can be recovered. To obtain the spectra and correct for the incomplete sky coverage of the LSPE observations we used the *CrossSpect* algorithm described in section (3.3.1). To avoid the noise bias on the recovered power spectra we computed the cross-correlation of the two different Q/U maps obtained by combining the output of diodes Q1/U1 of all the detectors with the one obtained from diodes Q2/U2. These two polarization maps in our simulations have uncorrelated noise.
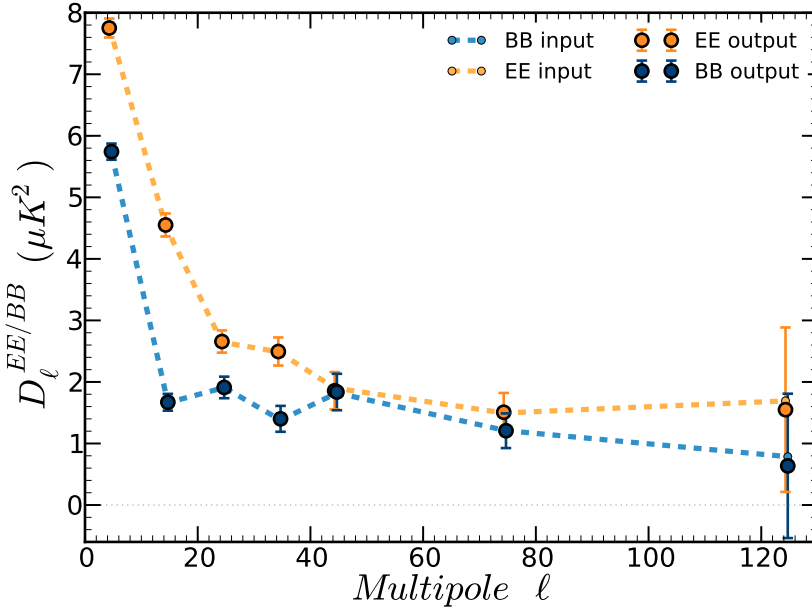
Figure 4.12: EE and BB power spectra obtained from end-to-end simulation of the STRIP instrument. Dashed lines represent the spectra of the input simulated sky, whose signal is dominated by synchrotron radiation. Orange and blue points represent the reconstructed power spectra from the simulation.

Figure (4.12) shows the resulting EE and BB power spectra. The signal at 43 GHz is dominated by the Galactic synchrotron emission and the STRIP measurements allow to reconstruct the spectrum of this signal up to $\ell \sim 80$. Error bars in figure (4.12) are obtained from the standard deviation of the spectra of one hundred simulations with independent realization of noise. These spectra are computed considering a multipole binning with $\Delta\ell = 10$ for $\ell < 50$ while for the last two bandpowers the binning covers a broader multiple range with $\Delta\ell = 50$ to optimize the sensitivity.

4.4 Simulating non-idealities in the polarimeters

Once we have simulated the performance of the STRIP instrument in the ideal case, we also included in the simulation pipeline the presence of different possible non-idealities in the experiment. As we have briefly seen in section (2.2), several systematic effects can contaminate polarization CMB measurements. In our analysis we principally focused on the non-idealities which can be present in the various components of the polarimeters, understating their impact on the final Q/U maps and polarization power spectra.

4.4.1 Modification of the analytical formalism

We included the possible systematic effects in the matrices describing the functioning of each component of the radiometric chain (see section 4.2.2). Using the Wolfram Mathematica computational software, which allows to perform symbolic calculations, we implemented the analytics equations of the polarimeter architecture obtaining the final outcomes of each diode. These equations are then finally included in our simulation pipeline. Here, for each considered non-ideality, we report the modified matrix describing the effect and the final output of the four polarimeter diodes after computing the double demodulation of the phase switch stages:

Polarizer: the matrix describing the polarizer functioning in the ideal case is reported in relation (4.1). In a more realistic analysis, we can consider the presence of cross-polarization η in the output signals ($\eta = 0$, in the ideal case) and writing the matrix which describes the polarizer as:

$$S_{Xpol}^{PL} = \begin{pmatrix} (1+\eta) & i*(1-\eta) \\ (1+\eta) & -i*(1-\eta) \end{pmatrix},$$ (4.15)

in this condition the output of the diodes can be written as:

$$\begin{pmatrix} Q1/Q2 \\ U1/U2 \end{pmatrix}_{asym}^{PL} = \frac{1}{4} \begin{pmatrix} \pm 2g_A g_B \left((1+\eta^2)\mathbf{Q} + 2\eta\mathbf{I}\right) \\ \pm 2g_A g_B (1-\eta^2)\mathbf{U} \end{pmatrix}$$ (4.16)

where the $\pm$ sign refers to the output of diodes-1 and 2 respectively (this convention is adopted also in the following relations). The presence of cross-polarization leads to a $I \rightarrow Q$ leakage in the detected signal.

OMT: the ideal functioning of the OMT is described by the matrix reported in (4.2). An imbalance in the OMT transmission ($m_1 = m_2 = 1$, in ideal case) or the presence of cross-polarization ($\varepsilon = 0$, in ideal case) leads to the following matrices:

$$S_{asym}^{OMT} = \begin{pmatrix} m_1 & 0 \\ 0 & m_2 \end{pmatrix}, \quad S_{Xpol}^{OMT} = \begin{pmatrix} 1 & \varepsilon \\ \varepsilon & 1 \end{pmatrix}$$ (4.17)

leading to final outputs in the form:

$$\begin{pmatrix} Q1/Q2 \\ U1/U2 \end{pmatrix}_{asym}^{OMT} = \frac{1}{4} \begin{pmatrix} \pm 2g_A g_B m_1 m_2 \mathbf{Q} \\ \pm 2g_A g_B m_1 m_2 \mathbf{U} \end{pmatrix}$$ (4.18)

$$\begin{pmatrix} Q1/Q2 \\ U1/U2 \end{pmatrix}^{OMT}_{Xpol} = \frac{1}{4} \begin{pmatrix} \pm 2g_A g_B \left((1+\varepsilon^2)\mathbf{Q} + 2\varepsilon \mathbf{I} \right) \\ \pm 2g_A g_B (1-\varepsilon^2)\mathbf{U} \end{pmatrix}. \tag{4.19}$$

The only effect is caused by the cross-polarization which generates a $I \rightarrow Q$ leakage proportional to ε in the Q1/Q2 output signals.

Phase Switches: we have seen that on both legs of the polarimeter a phase switch is present with phases φ_A and φ_B both switching between 0 and π at a giving frequency in the ideal case (see relation 4.3). The non-idealities in these components can consist in having phases not exactly equal to 0 or π or an imbalance in the signal transmission in the two switching stages ($s_{1/2} = s_{3/4} = 1$, in the ideal case):

$$S^{PhSw}_{asym} = \begin{pmatrix} s_{1/2} e^{i\varphi_A} & 0 \\ 0 & s_{3/4} e^{i\varphi_B} \end{pmatrix}, \quad \text{with } \{\varphi_A, \varphi_B\} = 0, \pi \tag{4.20}$$

$$S^{PhSw}_{ph} = \begin{pmatrix} e^{i\varphi_{A_{1/2}}} & 0 \\ 0 & e^{i\varphi_{B_{3/4}}} \end{pmatrix}, \quad \text{with } \begin{matrix} \varphi_{A_1} = \alpha_1, \varphi_{A_1} = \pi + \alpha_2 \\ \varphi_{B_3} = \alpha_3, \varphi_{B_4} = \pi + \alpha_4 \end{matrix} \tag{4.21}$$

where subscripts $1/2$ refers to first and second stage of phase switch on legA and subscripts $3/4$ to first and second stage of phase switch on legB. The outputs result in[6]:

$$\begin{pmatrix} Q1/Q2 \\ U1/U2 \end{pmatrix}^{PhSw}_{asym} = \frac{1}{8} \begin{pmatrix} \pm g_A g_B (s_1 + s_2)(s_3 + s_4)\mathbf{Q} \\ \pm g_A g_B (s_1 + s_2)(s_3 + s_4)\mathbf{U} \end{pmatrix} \tag{4.21}$$

$$\begin{pmatrix} Q1/Q2 \\ U1/U2 \end{pmatrix}^{PhSw}_{ph} = \frac{1}{2} \begin{pmatrix} \pm g_A g_B (X\mathbf{Q} - Y\mathbf{U}) \\ \pm g_A g_B (X\mathbf{U} + Y\mathbf{Q}) \end{pmatrix}. \tag{4.22}$$

The generic phase in the phase switch stages leads to leakage between Q and U signal, while the imbalance only leads to a multiplication factor in the outputs. Actually this result in case of imbalance is a direct consequence of the presence of the second phase switch in the polarimeter architecture: it can be easily shown that without the double demodulation the imbalance would cause an $I \rightarrow Q/U$ leakage, which could have a strong impact on the final measurement, the second slow phase switching is included to prevent this effect.

Amplifiers: we can consider the case in which the amplifiers add a generic phase to the amplified signal:

$$S^{Amp}_{ph} = \begin{pmatrix} g_A e^{i\varphi_{gA}} & 0 \\ 0 & g_B e^{i\varphi_{gB}} \end{pmatrix} \tag{4.23}$$

leading to the following outputs:

$$\begin{pmatrix} Q1/Q2 \\ U1/U2 \end{pmatrix}^{Amp}_{ph} = \frac{1}{2} \begin{pmatrix} \pm g_A g_B \left(\cos(\Delta\varphi_g)\mathbf{Q} + \sin(\Delta\varphi_g)\mathbf{U} \right) \\ \pm g_A g_B \left(\cos(\Delta\varphi_g)\mathbf{U} - \sin(\Delta\varphi_g)\mathbf{Q} \right) \end{pmatrix}, \tag{4.24}$$

---

[6]$X = \cos\left(\frac{\alpha_1 - \alpha_2}{2}\right) \cos\left(\frac{\alpha_3 - \alpha_4}{2}\right) \cos\left[\frac{1}{2}(\alpha_1 + \alpha_2 - \alpha_3 - \alpha_4)\right]$

$Y = \cos\left(\frac{\alpha_1 - \alpha_2}{2}\right) \cos\left(\frac{\alpha_3 - \alpha_4}{2}\right) \sin\left[\frac{1}{2}(\alpha_1 + \alpha_2 - \alpha_3 - \alpha_4)\right]$

where $\Delta\varphi_g = (\varphi_{gA} - \varphi_{gB})$, causing therefore a leakage between Q and U.

180° and 90° Couplers: the couplers in a non ideal polarimeter can have amplitude mismatches and phase errors. We can write the generic matrix describing the functioning of the couplers in the following way:

$$S^{Cpl} = \frac{1}{\sqrt{2}} \begin{pmatrix} c_1 e^{i(\pi - \varphi_c)} & c_2 \\ c_3 & c_4 e^{i\varphi_c} \end{pmatrix} \tag{4.25}$$

where, in the ideal case, the coefficients c are all equal to 1, $\varphi_c = \pi$ for the 180° coupler and $\varphi_c = \pi/2$ for the 90°. The final diode outputs can be written as:

$$\begin{pmatrix} Q1/Q2 \\ U1/U2 \end{pmatrix}^{180°}_{asym} = \frac{1}{4} \begin{pmatrix} \pm 2g_A g_B c_{1/3} c_{2/4} \mathbf{Q} \\ g_A g_B \left((c_1 c_2 - c_3 c_4)\mathbf{Q} \pm (c_1 c_4 + c_2 c_3)\mathbf{U} \right) \end{pmatrix} \tag{4.26}$$

$$\begin{pmatrix} Q1/Q2 \\ U1/U2 \end{pmatrix}^{180°}_{ph} = \frac{1}{2} \begin{pmatrix} \pm g_A g_B \left(\cos(\varphi_c)\mathbf{Q} + \sin(\varphi_c)\mathbf{U} \right) \\ \pm g_A g_B \cos(\varphi_c) \left(\cos(\varphi_c)\mathbf{U} - \sin(\varphi_c)\mathbf{Q} \right) \end{pmatrix} \tag{4.27}$$

$$\begin{pmatrix} Q1/Q2 \\ U1/U2 \end{pmatrix}^{90°}_{asym} = \frac{1}{4} \begin{pmatrix} \pm 2g_A g_B \mathbf{Q} \\ g_A g_B \left((c^2_{1/3} - c^2_{2/4})\mathbf{Q} \pm 2c_{1/3} c_{2/4} \mathbf{U} \right) \end{pmatrix} \tag{4.28}$$

$$\begin{pmatrix} Q1/Q2 \\ U1/U2 \end{pmatrix}^{90°}_{asym} = \frac{1}{2} \begin{pmatrix} \pm g_A g_B \mathbf{Q} \\ \pm g_A g_B \sin(\varphi_c)\mathbf{U} \end{pmatrix} \tag{4.29}$$

where in relations (4.26) and (4.28) subscripts $1/2$ refer to the output of the diodes-1, while subscripts $3/4$ refer to the diodes-2.

4.4.2 Impact on scientific results

We can divide the effects seen in the previous section into four different categories, depending on their impact on the final detected signal:

- non-idealities that generate $I \to Q$ leakage: polarizer and OMT cross-polarization;

- non-idealities that generate both $Q \to U$ and $U \to Q$ leakages: generic phases in the phase switches, amplifiers and 180° coupler;

- non-idealities that impact only on the U diodes causing $Q \to U$ leakage: asymmetries in the 180° and 90° couplers signal transmission;

- non-idealities that only account for multiplication factors in the final outputs.

Before run complete end-to-end simulations of the STRIP instrument including the described non-idealities, we can make a first estimate of their impact on the final measurements of the sky radiation by computing E and B-modes power spectra of the systematic effects themselves. Results are shown in figure (4.13); in each case the power spectrum of the systematic effect is calculated by computing the difference between a map (including foregrounds and CMB) of the LSPE observed region in the ideal case
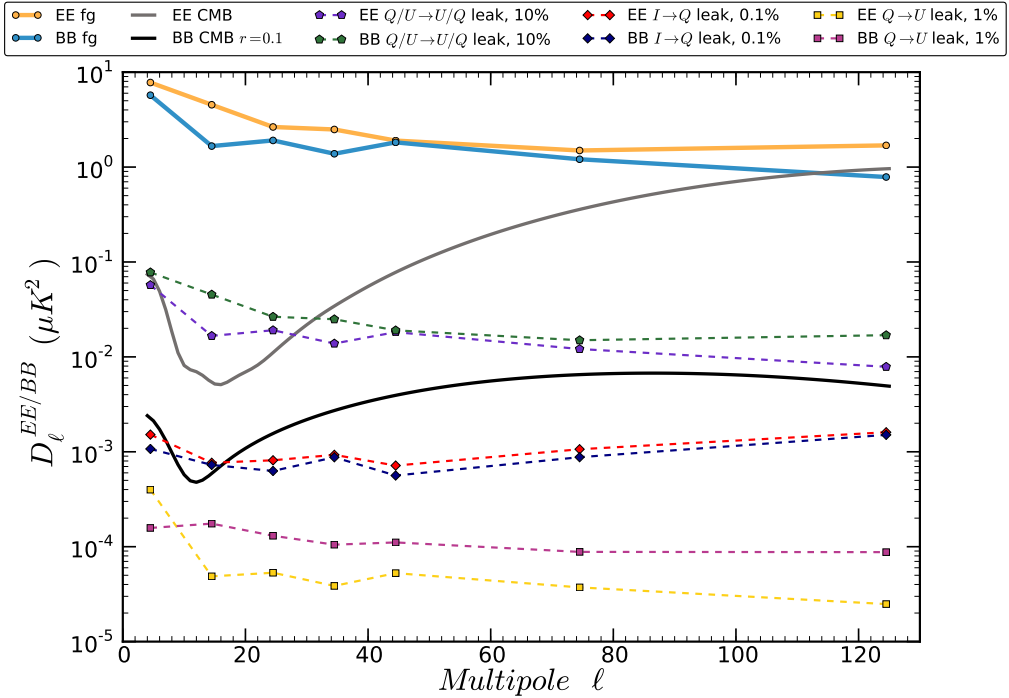
Figure 4.13: EE and BB angular power spectra of the possible systematic effects that may be caused by non-idealities in the polarimeter components (colored dashed lines) compared with the spectra of foreground emission at 43 GHz (blue and orange solid lines) and CMB radiation (black and grey solid lines).

and a map of the same region with the presence of the considered kind of leakage at the reported percentage level.

An $I \rightarrow Q$ leakage at the level of 0.1% (meaning that the 0.1% of the I power leaks into the detected Q signal) corresponds to a cross-polarization in the OMT or in the polarizer of the order of $-30\,\mathrm{dB}$. This level of cross-polarization is higher than what expected for the components assembled in the STRIP radiometric chains, which should have cross-polarization $< -40\,\mathrm{dB}$ (Virone et al. 2005). Nevertheless, even in the considered pessimistic case, we see from figure (4.13) that both the EE and BB spectra for this effect (blue and red dashed lines on the plot) lie well below the spectra of the foregrounds emission and are comparable with the level of CMB B-modes power spectrum (with $r = 0.1$) for low multiples with $\ell \lesssim 20$.

The 1% considered level of $Q \rightarrow U$ leakage is also a conservative estimate , since the level of signal transmission asymmetries in the couplers is expected to be very small. Nevertheless we see that even in the considered case the effect on the recovered power spectra is negligible (pink and yellow dashed lines).

Among the polarimeter non-idealities that can cause a $Q/U \rightarrow U/Q$ leakage the one that may have the largest impact is the error on the phase in the phase switches which is described by the matrix reported in (4.24). Indeed, the error on the phase angle can be of the order of few degrees (see for example Varis et al. 2009) leading to a leakage of

few percent. In figure (4.13) we report a $Q/U \to U/Q$ leakage of 10% and notice that in this case, even though the effect is negligible with respect to the spectra of the Galactic emission, this is not the case for the CMB. We have that the power spectra of the effect (green and purple dashed lines) are at the level of the CMB E-modes for multiples with $\ell \lesssim 40$.

It is important to remark though, that the $Q/U \to U/Q$ leakage effect caused by the polarimeter non-idealities is equivalent to a rotation in the polarization angle of the detector and therefore can be compensated by performing a calibration of this angle. This calibration can be made on Earth, using specific calibrators, and in-flight by observing specific sources such as the Crab Nebula or the Moon. For the STRIP detectors we expect to recover the polarization angle with an accuracy at the order of $1°$.
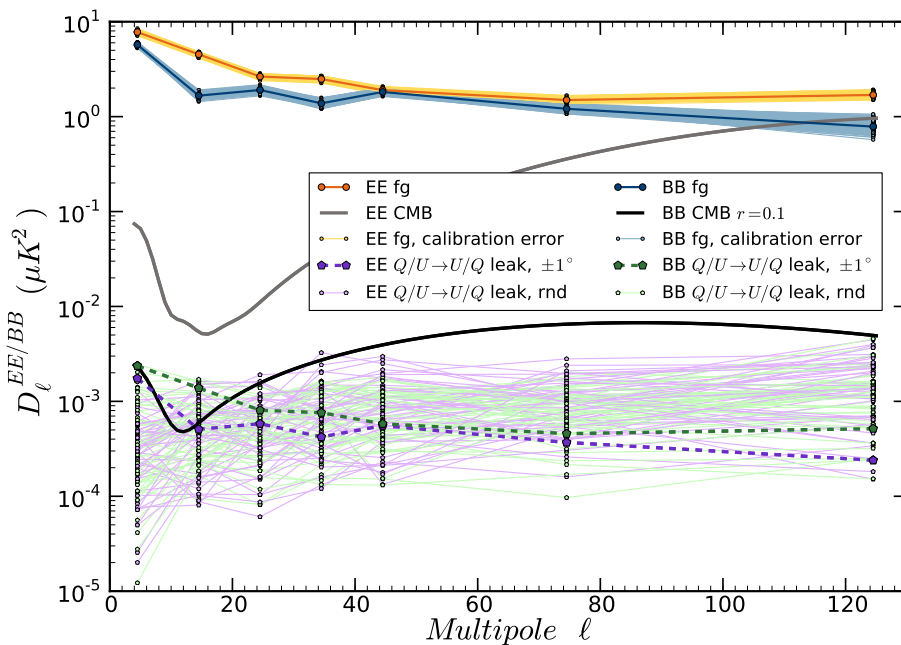

Figure 4.14: Power spectra to evaluate the impact of polarization angle error and responsivity calibration on STRIP measurements. Purple and green lines are the results of the one hundred simulation on the polarization angle errors, while yellow and blue thin lines are the spectra resulting from simulations on the responsitivy calibration errors (see text for details about these simulations). Solid thick lines are the power spectra of Galactic foreground and CMB radiations.

To evaluate the impact of polarization angle accuracy on the final sky measurements of the STRIP instrument we performed end-to-end simulations. In these simulations we considered the full STRIP focal plane and, for each of the 49 detectors, we included a polarization angle error randomly chosen between $\pm 1°$, in order to maximize the effect given the accuracy we expect to achieve with calibration. In this way we take into account how the effect sums up between the several detectors and also consider the sky
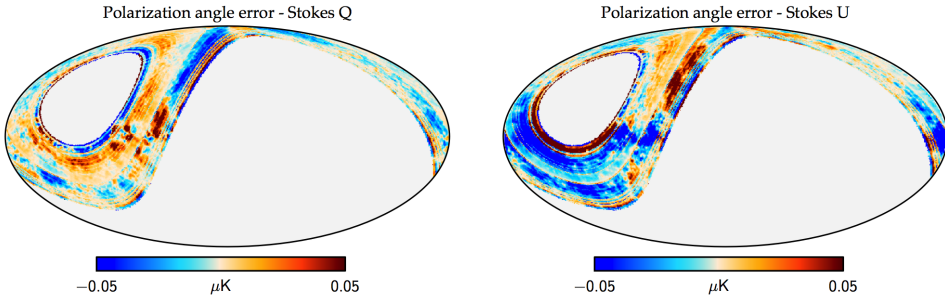
Figure 4.15: Effect of polarization angle error on Stokes Q and U maps. These maps are computed from a single simulation as described in the text and are the difference between maps generated considering the angle error and the maps in the ideal case.

scanning strategy. We realized one hundred simulations randomly changing the polarization angle error of the detectors and, for each simulation, we recovered the final Q/U maps and computed the difference with the Q/U sky map obtained in the ideal case (i.e with no error on the polarization angle)[7]. We then plotted the obtained one hundred EE and BB power spectra of these difference maps, shown as thin solid purple and green lines respectively on figure (4.14). Power spectra of the described simulations are compared with the ones obtained from the case where all detectors have the same polarization angle error equal to $1°$ (or $-1°$) shown with green and purple thick dashed lines on figure (4.15). We see that the sum of different errors for the various detectors and the combination with the sky scanning strategy reflect in having an average smaller impact at low multipoles and a higher one at the larger angular scales. From these simulations we can conclude that the impact of having an error on the polarization angle of $\sim 1°$ is negligible if compared with the Galactic signal, while for CMB radiation it can reach the level of the B-modes power spectrum with $r = 0.1$. Figure (4.15) shows the Q and U difference maps for one single simulation where we can see the effect of the sky scanning strategy causing the stripes pattern on the maps.

We have previously described how non-idealities in the polarimeter components can, in several cases, cause an attenuation of the detected signals which therefore reflects on the calibration of the responsivity of the detectors. As for the polarization angle, also the responsivity calibration of the STRIP detectors will be carried out before the balloon launch and during the flight. The in-flight calibration will be realized principally by observing the Crab Nebula polarized emission. From preliminary studies simulating the in-flight calibration strategy, we expect to achieve an accuracy at the order of 10% for the STRIP detectors (Montresor 2013). We therefore ran some simulations to asses the impact of this uncertainty on the final measurements, allowing for a calibration error for each STRIP detector chosen randomly between $\pm 10\%$. From the final Q/U map obtained summing the 49 maps of the detectors we computed the angular power spectra.

---

[7]Note that in this case the simulations are computed without considering the presence of noise in the detectors in order to evaluate directly the impact of the error on the polarization angle.

We ran one hundred simulations with the described procedure, changing randomly the calibration error of the detectors. The one hundred outcoming spectra are shown in figure (4.14), resulting in the yellow and blue shaded areas around the Galactic foreground spectra. As for the polarization angle errors, combining the uncertainties on the responsivity for the different STRIP detectors and considering the sky scanning strategy imply a lower impact at low multiples with respect to the higher ℓ. The maximum deviation from the ideal foreground spectra in the first considered multiple bin ($\ell \simeq 4$) in our simulations is of $\sim 9\%$, while in the last bin at $\ell \simeq 120$ can reach $\sim 30\%$.

4.5   Concluding remarks

In this chapter we described the simulation pipeline developed for the low frequency instrument onboard the LSPE experiment.

The STRIP instrument, by performing observations at the frequency of 43 GHz, will mainly measure the synchrotron polarized radiation on a large fraction of the sky. These observations will be important to remove the synchrotron contribution from the CMB measurements performed, at higher frequencies, by the SWIPE instrument also onboard the LSPE experiment.

Thanks to the end-to-end simulations we were able to asses the expected scientific performance of the STRIP instrument, reconstructing the polarization sky maps and power spectra as observed by the detector array. Considering the simplest case of an ideal instrument, our simulations showed that STRIP will be able to recover the E and B-modes power spectra of the synchrotron radiation up to multiple $\ell \simeq 80$.

We also added in our pipeline several non-idealities in the polarimeter behavior, computing first analytical calculation to understand their propagation through the polarimeter architecture up to the final signal detection and then, including them in the simulation process to derive their impact on the observed maps and power spectra.

All the effects we took into account result in having a negligible impact on the measurement of the synchrotron radiation at 43 GHz, showing therefore that the STRIP polarimeter architecture is capable of minimizing the systematic effects.

The accuracy in the detectors resposivity calibration will be a crucial aspect for the STRIP instrument. We have seen that an accuracy at the level of 10% on the calibration (achievable with in-flight observations of the Crab Nebula) would reflect in uncertainties of about $\sim 30\%$ on the power spectra for the smaller angular scales. A calibration campaign before the balloon flight will therefore be essential to better characterize the detectors.

In our analysis, several systematic effects have not been taken yet into account. In particular, we are currently working to include in our simulations those effects associated with the optical beam proprieties. Measurements carried out in anechoic chamber already provided us the characterization of the optical beam patterns of all the STRIP antennas. Starting from them and using a dedicated simulation software, we can compute the angular response of the instrument full optical system. Adding a module to the pipeline, which simulates the observation of the sky considering the actual angular response, will be important to understand the impact of beam asymmetries and sidelobes pickup on the final results.

Another important aspect to assess the expected scientific performance of the entire

LSPE experiment is the simulation of the astrophysical component separation, considering the four observation frequencies of the two instruments. Since the angular resolution of the instruments will be very similar in all the frequency bands, both a parametric or minimum variance methods in the pixel domain (see section 2.1.4) will be ideal approaches to perform the separation and isolate the CMB signal. Moreover we could also propagate the considered STRIP systematic effects through the component separation and estimate their impact on the final CMB maps and power spectra.

Conclusions

In this thesis we dealt with the two main challenges for present and future CMB polarization experiments: the characterization of foreground emissions and the control of instrumental systematic effects. We focused on two specific and explicatory experimental cases to study these topics. In particular, for what concerns the foreground emission we analyzed the Planck thermal dust observations in the BICEP2 field. On the other hand, we carried out the analysis of instrumental systematic effects relevant for polarization observations in the context of simulations for the LSPE experiment.

Our study of the foreground emission in the BICEP2 field, triggered by the BICEP2 measurement of an excess in the B-modes power spectrum compatible with the signal expected from primordial gravitational waves (BICEP2 collaboration I 2014), represents a specific aspect of a more general analysis on the polarized thermal dust proprieties carried out by the Planck collaboration (Planck Collaboration Int. XXX 2014).

In particular, the high frequency Planck observations allowed the study of the Galactic thermal dust polarized emission at intermediate and high Galactic latitudes. Thanks to the analysis of data on large regions of the sky (with sky fractions ranging from 30% to 80%) we recovered some general properties of the dust angular power spectra, in particular:

- the angular power spectra C_ℓ^{EE} and C_ℓ^{BB} at 353 GHz are well fit by power laws in ℓ with exponents consistent with $\alpha_{EE,BB} = -2.42 \pm 0.02$.

- The thermal dust frequency dependence in polarization is accurately described by the modified blackbody dust emission law derived from total intensity data with $\beta_d = 1.59$ and $T_d = 19.6\,\mathrm{K}$.

We found that these general proprieties also hold in the BICEP2 field on which we focused our analysis, with the specific goal of understanding the level of contamination arising from Galactic foreground in the BICEP2 CMB measurements . Our analysis, carried out using mainly Planck data at 353 GHz, showed that the dust signal in the BICEP2 region is high enough to account for the excess observed by BICEP2 in the B-modes power spectrum at 150 GHz.

This result was also confirmed by the Planck and BICEP2 joint analysis, that showed a positive correlation between Planck 353 GHz and BICEP2 150 GHz data. This joint

analysis constrained the value of the tensor-to-scalar ratio, with $r < 0.12$ at 95% confidence level (BICEP2/Keck Array and Planck Collaborations 2015).

The results of the Planck and BICEP2 observations certainly represent an important step toward a future possible detection of CMB primordial B-modes. In particular, this analysis made clear that Galactic foreground emissions are expected to be dominant over the CMB B-modes signal all over the sky, even at the highest Galactic latitudes, and at all the frequencies relevant for cosmological studies. Planck multi-frequency observations allowed to obtain full sky maps of both polarized synchrotron and thermal dust emissions. Nevertheless, as pointed out also in this thesis, the sensitivity of the Planck observations in the lowest and highest frequency bands is not optimal, preventing to perform astrophysical component separation with the level of accuracy needed to eventually isolate a CMB B-modes signal with $r \lesssim 0.1$.

Currently, several new ground-based and balloon-borne experiments are being designed or built, with the goal of reaching high sensitivity, not only in the frequency channels optimized for CMB observations (i.e $\sim 100/150$ GHz), but also at higher frequencies where thermal dust emission is brighter.

The Polarbear experiment already observed the sky at 150 GHz on small angular scales, detecting the CMB B-modes lensing signal (Polarbear Collaboration 2014). In the next years, the successor experiments, Polarbear-2 and the Simon Array, will perform observations with a large array of bolometers working in three frequency bands centered at 95, 150 and 220 GHz[8].

The EBEX (*E and B Experiment*) balloon-borne experiment observed the sky in three frequency bands at 150, 250, and 410 GHz during an eleven day flight in 2012, with data analysis still ongoing (MacDermid et al. 2014). A proposal for EBEX10k, the successor of EBEX, has been recently submitted to NASA. In the proposed configuration, EBEX10k is equipped with more than eleven thousands of polarization sensitive bolometers working in four frequency bands: 150, 220, 280 and 350 GHz. The highest frequency bands, in particular, will be crucial to characterize the thermal dust emission with high sensitivity having a noise level per pixel at 350 GHz six times lower than Planck. With this high sensitivity EBEX10K will reconstruct the power spectrum of galactic dust with 36 times higher signal-to-noise ratio compared to Planck. Using component separation it will have the capability to extract the CMB B-modes at signal levels as low as $r < 0.009$ (2σ)[9].

Another experiment, under development, with a multi-frequency coverage allowing for component separation is the *Q and U Bolometric Interferometer for Cosmology* (QUBIC, QUBIC Collaboration 2011). QUBIC is today the only instrument based on bolometric interferometry, a novel technique that brings together the high sensitivity of bolometric detectors with the systematics effects advantages of interferometry. In its final configuration QUBIC will have three frequency channels at 97, 150, 220 GHz.

The LSPE balloon-borne experiment, will perform a long duration flight (~ 15 days) around the North Pole in December 2016, observing the sky in four frequency bands, with high and low frequency channels that will monitor the foreground emissions. The observations will cover a large portion of the sky of about 30% focusing therefore on measurements of CMB and foreground polarization on the very large angular scales.

---

[8] http://bolo.berkeley.edu/polarbear/

[9] Private communication with Prof. Shaul Hanany (University of Minnesota), P.I. of EBEX and EBEX10k.

All these new generation of CMB experiments, reaching high sensitivity, will need to have a high control of systematic effects. This problem represents the second topic of this thesis and, in particular, we analyzed this issue by considering the case of the LSPE experiment. We developed a simulation pipeline for the STRIP instrument, which, with a single frequency bands centered at 43 GHz, will mainly observe the polarized synchrotron radiation on large angular scales.

The developed pipeline allowed us to simulate both the sky scanning strategy of the instrument, allowing the optimization of the focal plane configuration, and the polarimeter architecture, which is based on radiometric technology. We computed end-to-end simulations of the STRIP sky observations, recovering maps and power spectra as observed by the instrument. In our simulations we also included some possible systematic effects arising from non-idealities in the polarimeters and we derived their impact on the observed maps and power spectra. Our simulations allowed us to understand that the STRIP polarimeters architecture is efficient in minimizing the systematic effects, which, in the considered cases, have a negligible impact on the final sky observations.

As pointed out, our simulations do not include yet the effects concerning the optical beams. A preliminary work in this context is ongoing and a module which simulates sky observation with realistic beams, including effects arising from beam asymmetries and sidelobes pickup, is currently under implementation and will be added to the pipeline.

Finnaly, we are currently working on astrophysical component separation simulations for the LSPE experiment, using a pixel based parametric fitting technique. This simulations will allow to better understand the expected scientific performance of the two LSPE instruments in detecting the CMB B-modes signal at the very large angular scales, by considering the observations in all the four frequency bands.

The Planck space mission

Since, in this thesis, we make intensive use of the Planck data, we report here e brief overview about the space mission characteristics and the onboard instrumentation. For a detailed description we refer to general Planck papers, for example Planck Collaboration (2005) and Planck Collaboration I (2011).

Planck was launched from Kourou, French Guiana, on 14 May 2009 on an Ariane 5 rocket and was injected into a 6-month Lissajous orbit around second Lagrangian point (L_2) of the Sun-Earth system. Science observations began on 12 August 2009 and completely ended on 23 October 2013.

The main objective of Planck, defined in 1995 during the first design phase, was to measure the CMB temperature anisotropies, with an accuracy set by fundamental astrophysical limits, thereby extracting essentially all the cosmological information embedded in the temperature fluctuation. Planck was also designed to measure to high accuracy the CMB polarization anisotropies. In particular, the analysis of the Planck polarization data is still on going and the first scientific results and products have been released in early 2015.

Planck scientific payload is composed by an array of 74 detectors sensitive to frequencies between 25 and 1000 GHz, with angular resolution between 33 and 5 arcmin. The detectors of the *Low Frequency Instrument* (LFI) are pseudo-correlation radiometers, covering bands centered at 30, 44, and 70 GHz (all three channels are sensitive to polarization). The detectors of the *High Frequency Instrument* (HFI) are bolometers, covering bands centered at 100, 143, 217, 353, 545, and 857 GHz (sensitive to polarization up to 353 GHz).

The wide frequency coverage, as described in chapter (2), is essential to separate the CMB signal from the Galactic foreground emission. Planck observations, indeed, not only allowed to obtain full sky maps of the CMB temperature and polarization with unprecedented sensitivity and angular resolution, but, measurements in the lowest and highest frequency bands, also produced the most precise full sky maps of the foreground emissions available today. These recovered maps, especially the polarization ones, are of fundamental importance for other current and future experiments.

During the entire mission, Planck spinned at angular velocity of 1 rpm around the symmetry axis of the spacecraft, scanning the sky in great circles. The spin axis remained fixed for between 39 and 65 spins, depending on which part of the orbit the satellite was located. Therefore, each instrument observed precisely the same sky between 39 and 65 times. The set of observations made during a period of fixed spin axis pointing is often

referred to as a "ring". This redundancy plays a key role in the analysis of the data, since, as already mentioned in the previous chapters, gives set of independent maps, useful to compute null tests to check for systematics or to calculate cross spectra without the noise bias. As the Earth and Planck orbited around Sun, the great observed circles, rotated around the ecliptic poles. Figure (A.1) shows the resulting coverage of the sky, red regions have been observed for longer integration time.
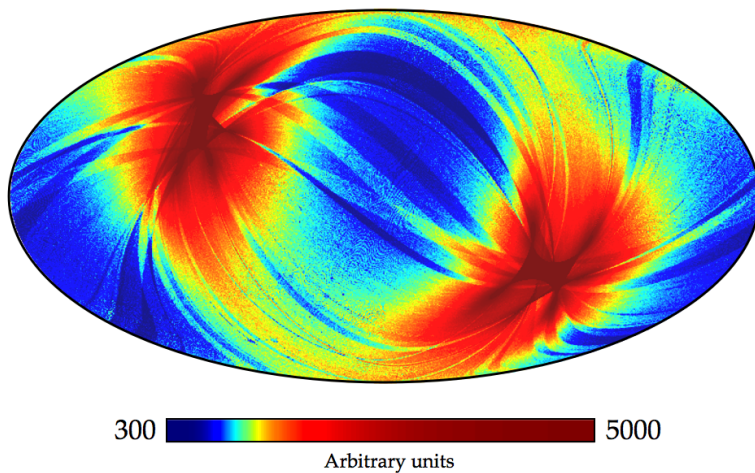

Figure A.1: Sky coverage map (in Galactic coordinate system) obtained from the Planck 100 GHz observations. The Planck scanning strategy is such that ecliptical poles are observed for longer integration time and thus the overall sensitivy is higher in these regions.

A.1   The Low Frequency Instrument

The LFI instrument (Bersanelli et al. 2010; Mennella et al. 2011) is composed by an array of 22 differential receivers based on cryogenic HEMT amplifiers. Radiation from the sky, collected by the Planck telescope, is observed through 11 corrugated feed horns, each coupled with a double-radiometer system. Each feed horn is connected to an OMT which separates the received signal into the two orthogonal polarizations. Two parallel and independent radiometers are connected to the output ports of the OMT, thus preserving the polarization information. These two radiometers are often called "main" and "side" OMT arms. The sky signal, in each arm, is separately amplified and differenced against the signal coming from a cold load at a nominal temperature of 4 K. There is a separate 4-K load for each arm of each radiometric chain.

By summing and differencing the calibrated outputs of these two arms, this configuration allows the recovery of the total intensity I and one component of the (Q_H, U_H) vector of the Stokes parameters of the incoming radiation, in the horn coordinate frame.

All LFI feed horns (with the only exception of a single spare feed horn at 44 GHz) are arranged in pairs which follow the same scan path, and whose polarization angles differ by approximately $45°$. Thus the second horn measures the Stokes parameter U_H, which

therefore, together with the values of Q_H measured by the first horn, allows to recover the linear polarization status of the observed radiation (for a complete description of the LFI polarization capability we refer to Leahy et al. 2010).

Table (A.1) summarizes the principal specifications of the recovered full mission maps in the three LFI frequency channels.

Parameter	30 GHz	44 GHz	70 GHz
Central Frequency [GHz]	28.4	44.1	70.4
Beam FWHM [arcmin]	33.16	28.09	13.08
White noise on map I [μK]	3.32	3.80	3.33
White noise on map Q/U [μK]	4.68	5.62	4.71

Table A.1: Principal LFI full mission maps characteristics. The level of white noise in in thermodynamic temperature and is scaled to $1°$ assuming that the noise is white.

A.2 The High Frequency Instrument

The HFI instrument (Lamarre et al. 2010; Planck HFI Core Team 2011) is composed by an array of 52 bolometers (32 of them sensitive to polarization), coupled with corrugated feed horns and located in the focal plane of the Planck telescope. The bolometers are sensitive to radiation in six frequency channels with central frequency form 100 to 857 GHz.

In a very schematized description, bolometers consist of (i) an absorber that transforms the incoming radiation into heat; (ii) a thermometer that is thermally linked to the absorber and measures the temperature changes; and (iii) a weak thermal link to a thermal sink, to which the bolometer is attached.

The HFI architecture is based on independent optical chains collecting the light from the telescope and feeding it to bolometers or bolometer pairs. Each of the total of 36 optical chains is composed by back- to-back horns, which provide initial geometrical and spectral selection of the radiation, and a first set of filters that blocks the highest

Parameter	100 GHz	143 GHz	217 GHz	353 GHz
Central Frequency [GHz]	100	143	217	353
Beam FWHM [arcmin]	9.68	7.30	5.02	4.94
White noise on map I [μK]	1.29	0.55	0.78	2.56
White noise on map Q/U [μK]	1.96	1.17	1.75	7.31

Table A.2: Principal HFI full mission maps characteristics, for the four frequency channels sensitive to polarization. The level of white noise in in thermodynamic temperature and is scaled to $1°$ assuming that the noise is white.

frequency. After that another detector horn is present, coupled with the bolometer(s), cooled down at a temperature of $0.1\,\mathrm{K}$.

Sixteen out of the 36 chains feed pairs of polarization-sensitive bolometers. For these bolometers the absorber are rectangular metallic grid which absorb only one state of polarization (see Holmes et al. 2008 for a detailed description of the HFI bolometers). In each pair two bolometers with absorber grids perpendicular to each other are located, allowing to reconstruct the full polarization status of the incoming radiation and recover the Q/U Stokes parameters.

Table (A.1) summarizes the principal specifications of the recovered full mission maps in the four HFI frequency channels which are sensitive to polarization.

Bibliography

Albrecht, A. & Steinhardt, P. J. 1982, Physical Review Letters, 48, 1220

Alpher, R. A., Bethe, H., & Gamow, G. 1948, Physical Review, 73, 803

Barkats, D., Aikin, R., Bischoff, C., et al. 2014, *Astrophys. J.*, 783, 67

Baumann, D. 2009, arXiv:0907.5424

Baumann, D., Jackson, M. G., Adshead, P., et al. 2009, in American Institute of Physics Conference Series, Vol. 1141, 10–120

Bennett, C. L., Larson, D., Weiland, J. L., et al. 2013, *Astrophys. J. Suppl.*, 208, 20

Bersanelli, M., Mandolesi, N., Butler, R. C., et al. 2010, *Astron. Astrophys.*, 520, A4

BICEP2 and Keck Array collaboration V. 2015, *Astrophys. J.*, submitted, arXiv: 1502.00643

BICEP2 collaboration I. 2014, *Physical Review Lett.*, 112, 241101

BICEP2 collaboration II. 2014, *Astrophys. J.*, 792, 62

BICEP2/Keck Array and Planck Collaborations. 2015, *Physical Review Lett.*, 114, 101301

Bischoff, C. A. 2010, PhD thesis, The University of Chicago

Brown, M. L., Ade, P., Bock, J., et al. 2009, *Astrophys. J.*, 705, 978

Bunn, E. F., Zaldarriaga, M., Tegmark, M., & de Oliveira-Costa, A. 2003, *Phys. Rev. D*, 67, 023501

Carretti, E., Cortiglioni, S., Sbarra, C., & Tascone, R. 2004, *Astron. Astrophys.*, 420, 437

Chiang, H. C., Ade, P. A. R., Barkats, D., et al. 2010, *Astrophys. J.*, 711, 1123

Crill, B. P., Ade, P. A. R., Battistelli, E. S., et al. 2008, in Society of Photo-Optical Instrumentation Engineers (SPIE) Conference Series, Vol. 7010, 2

Del Torto, F., Bersanelli, M., Cavaliere, F., et al. 2011, *Journal of Instrumentation*, 6, 6009

Delabrouille, J., Betoule, M., Melin, J.-B., et al. 2013, *Astron. Astrophys.*, 553, A96

Dicke, R. H., Peebles, P. J. E., Roll, P. G., & Wilkinson, D. T. 1965, *Astrophys. J.*, 142, 414

Dodelson, S. 2003, Modern Cosmology, Academic Press (Academic Press)

Dragone, C. 1978, *AT&T Technical Journal*, 57, 2663

Eriksen, H. K., Dickinson, C., Lawrence, C. R., et al. 2006, *Astrophys. J.*, 641, 665

Fixsen, D. J. 2009, *Astrophys. J.*, 707, 916

Fixsen, D. J., Cheng, E. S., Cottingham, D. A., et al. 1994, *Astrophys. J.*, 420, 445

Fuskeland, U., Wehus, I. K., Eriksen, H. K., & Næss, S. K. 2014, *Astrophys. J.*, 790, 104

Gold, B., Odegard, N., Weiland, J. L., et al. 2011, *Astrophys. J. Suppl.*, 192, 15

Górski, K. M., Hivon, E., Banday, A. J., et al. 2005, *Astrophys. J.*, 622, 759

Grain, J., Tristram, M., & Stompor, R. 2009, *Phys. Rev. D*, 79, 123515

Guth, A. H. & Tye, S.-H. H. 1980, Physical Review Letters, 44, 963

Hanson, D., Hoover, S., Crites, A., et al. 2013, *Physical Review Lett.*, 111, 141301

Hinshaw, G., Nolta, M. R., Bennett, C. L., et al. 2007, *Astrophys. J. Suppl.*, 170, 288

Hivon, E., Górski, K. M., Netterfield, C. B., et al. 2002, *Astrophys. J.*, 567, 2

Holmes, W. A., Bock, J. J., Crill, B. P., et al. 2008, *Appl. Opt.*, 47, 5996

Hu, W. & White, M. 1997, *New Astron.*, 2, 323

Hubble, E. 1929, Proceedings of the National Academy of Science, 15, 168

Kogut, A., Dunkley, J., Bennett, C. L., et al. 2007, *Astrophys. J.*, 665, 355

Kovac, J. M., Leitch, E. M., Pryke, C., et al. 2002, *Nature*, 420, 772

Lamarre, J.-M., Puget, J.-L., Ade, P. A. R., et al. 2010, *Astron. Astrophys.*, 520, A9

Lazarian, A. & Finkbeiner, D. 2003, *New Astron. Rev.*, 47, 1107

Leahy, J. P., Bersanelli, M., D'Arcangelo, O., et al. 2010, *Astron. Astrophys.*, 520, A8

Linde, A. D. 1982, Physics Letters B, 108, 389

LSPE Collaboration. 2012, in Society of Photo-Optical Instrumentation Engineers (SPIE) Conference Series, Vol. 8446, 7

LSPE-STRIP Collaboration. 2012, in Society of Photo-Optical Instrumentation Engineers (SPIE) Conference Series, Vol. 8446, 7

LSPE-SWIPE Collaboration. 2012, in Society of Photo-Optical Instrumentation Engineers (SPIE) Conference Series, Vol. 8452, 3

MacDermid, K., Aboobaker, A. M., Ade, P., et al. 2014, in Society of Photo-Optical Instrumentation Engineers (SPIE) Conference Series, Vol. 9153, 11

Maffei, B., Gleeson, E., Murphy, J. A., & Pisano, G. 2004, in Society of Photo-Optical Instrumentation Engineers (SPIE) Conference Series, Vol. 5498, 812

Maino, D., Burigana, C., Maltoni, M., et al. 1999, *Astron. Astrophys. Supp. Ser.*, 140, 383

Mennella, A., Bersanelli, M., Butler, R. C., et al. 2011, *Astron. Astrophys.*, 536, A3

Montresor, G. 2013, Master's thesis, Universita' degli Studi di Milano

Netterfield, C. B., Ade, P. A. R., Bock, J. J., et al. 2002, *Astrophys. J.*, 571, 604

Newburgh, L. 2010, PhD thesis, Columbia University

Page, L., Hinshaw, G., Komatsu, E., et al. 2007, *Astrophys. J. Suppl.*, 170, 335

Penzias, A. A. & Wilson, R. W. 1965, *Astrophys. J.*, 142, 419

Perlmutter, S., Aldering, G., Goldhaber, G., et al. 1999, *Astrophys. J.*, 517, 565

Planck Collaboration. 2005, ESA publication ESA-SCI(2005)/01, arXiv:0604069

Planck Collaboration I. 2011, *Astron. Astrophys.*, 536, A1

Planck Collaboration I. 2014, *Astron. Astrophys.*, 571, A1

Planck Collaboration I. 2015, *Astron. Astrophys.*, submitted, arXiv:1502.01582

Planck Collaboration II. 2015, *Astron. Astrophys.*, submitted, arXiv:1502.01583

Planck Collaboration III. 2014, *Astron. Astrophys.*, 571, A3

Planck Collaboration III. 2015, in preparation

Planck Collaboration Int. XIX. 2015, *Astron. Astrophys.*, 576, A104

Planck Collaboration Int. XXII. 2015, *Astron. Astrophys.*, 576, A107

Planck Collaboration Int. XXX. 2014, *Astron. Astrophys.*, arXiv:1409.5738

Planck Collaboration IX. 2015, *Astron. Astrophys.*, submitted, arXiv:1502.05956

Planck Collaboration V. 2014, *Astron. Astrophys.*, 571, A5

Planck Collaboration VI. 2014, *Astron. Astrophys.*, 571, A6

Planck Collaboration VII. 2015, *Astron. Astrophys.*, submitted, arXiv:1502.01586

Planck Collaboration VIII. 2014, *Astron. Astrophys.*, 571, A8

Planck Collaboration X. 2015, *Astron. Astrophys.*, submitted, arXiv:1502.01588

Planck Collaboration XI. 2015, in preparation

Planck Collaboration XII. 2014, *Astron. Astrophys.*, 571, A12

Planck Collaboration XIII. 2015, *Astron. Astrophys.*, submitted, arXiv:1502.01589

Planck Collaboration XVI. 2014, *Astron. Astrophys.*, 571, A16

Planck HFI Core Team. 2011, *Astron. Astrophys.*, 536, A4

Polarbear Collaboration. 2014, *Astrophys. J.*, 794, 171

QUBIC Collaboration. 2011, *Astroparticle Physics*, 34, 705

QUIET Collaboration. 2011, *Astrophys. J.*, 741, 111

QUIET Collaboration. 2012, *Astrophys. J.*, 760, 145

Reinecke, M., Dolag, K., Hell, R., Bartelmann, M., & Enßlin, T. A. 2006, *Astron. Astrophys.*, 445, 373

Riess, A. G., Filippenko, A. V., Challis, P., et al. 1998, *Astron. J.*, 116, 1009

Rybicki, G. B. & Lightman, A. P. 1979, Radiative processes in astrophysics (New York, Wiley)

Seiffert, M., Mennella, A., Burigana, C., et al. 2002, *Astron. Astrophys.*, 391, 1185

Smoot, G. F., Bennett, C. L., Kogut, A., et al. 1992, *Astrophys. J. Lett.*, 396, L1

Stompor, R., Leach, S., Stivoli, F., & Baccigalupi, C. 2009, *Mon. Not. R. Astron. Soc.*, 392, 216

Varis, J., Hughes, N. J., Laaninen, M., et al. 2009, *Journal of Instrumentation*, 4, 2001

Virone, G., Tascone, R., Baralis, M., et al. 2005, IEEE Transactions on Microwave Theory Techniques, 53, 888

Wandelt, B. D. & Górski, K. M. 2001, *Phys. Rev. D*, 63, 123002

Zaldarriaga, M. & Seljak, U. 1997, *Phys. Rev. D*, 55, 1830